ON THE MECHANICS OF BIO-INSPIRED STRUCTURES FOR ENHANCED ENERGY DISSIPATION, FATIGUE RESILIENCE AND VIBRATIONAL CONTROL

by

Adwait Arun Trikanad

A Dissertation

Submitted to the Faculty of Purdue University

In Partial Fulfillment of the Requirements for the degree of

Doctor of Philosophy

Lyles School of Civil Engineering

West Lafayette, Indiana

December 2021

THE PURDUE UNIVERSITY GRADUATE SCHOOL
STATEMENT OF COMMITTEE APPROVAL

Dr. Pablo D Zavattieri, Chair
Lyles School of Civil Engineering

Dr. Mirian Velay-Lizancos
Lyle School of Civil Engineering

Dr. Ramses Martinez
School of Industrial Engineering

Dr. Eric Nauman
School of Mechanical Engineering

Approved by:
Dr. Dulcy Abraham

To my parents, Smitha and Arun Trikanad,
my sister, Shruti
and my fiancé, Priya
for their endless love and support.

ACKNOWLEDGMENTS

First and foremost, I would like to offer my sincere gratitude to my advisor and mentor, Dr Pablo Zavattieri, for his support, encouragement and motivation during my PhD. He has taught me to think critically, focus on the big picture and given me space to explore my own ideas while always offering sound advice and valuable guidance along the way. The completion of this thesis would not have been possible without your support and encouragement, and I am forever grateful.

I would like to acknowledge financial support from the National Science Foundation through the CAREER award CMMI 1254864, and the Air Force Office of Scientific Research Multi-University Research Initiative (AFOSR-FA9550-15-1-0009). A special thanks to my PhD committee members, Dr Mirian Velay-Lizancos, Dr Ramses Martinez and Dr Eric Nauman for their comments and advice along the way.

I wish to thank all my collaborators in the Hernandez research group at Cornell, the McKittrick research group at UCSD, the Kisailus research group at UC Irvine, and the Bernal research group at Purdue University for their input, data and discussions.

A great environment to work is paramount to be productive and successful at graduate school. A big thank you to all my colleagues at the Multi-Scale Mechanics of Materials by Design Lab over the years including David, Yunlan, Di, Hadi, Mehdi, Chan, Alvaro, Kris, Jack and Saket. To Yunlan, Kris and Jack, our numerous discussions about mechanics have been an invaluable learning experience for me. Thank you for checking in on me and offering advice whenever I needed it. A special thanks to David Restrepo for mentoring me during my early years, being patient and always offering sound advice.

I offer sincere gratitude to my friends who have become family over the last few years. Thank you to Ajey, Kartik, Diwakar and Ankit for always being there when I needed them, and for motivating me and keeping my spirits up during difficult times.

This thesis would not have been completed without the support of my family. Thank you to my sister, for always being there for me and for keeping my spirits high from another country. Thank you to my fiancé, Priya for her constant love and support and for always believing in me and for encouraging me to push my boundaries. Finally, my deepest gratitude to my parents for their emotional support, affection and enthusiasm throughout my PhD journey. No words can describe the sacrifices they have made over the years to allow me to pursue my professional goals.

TABLE OF CONTENTS

LIST OF FIGURES 8
ABSTRACT 12
1. INTRODUCTION 14
1.1 Natural Materials 14
1.2 Natural Materials for Durability and Fatigue life 16
1.3 Natural Materials that harness Mechanical Vibrations 16
1.4 Natural Materials exhibiting Impact Resistance 17
1.5 Motivation 18
1.6 Objectives 18
1.7 Outline 19
2. BONE INSPIRED MICROARCHITECTURES ACHIEVE ENHANCED FATIGUE LIFE.. 21
2.1 Introduction 21
2.2 Experimental Analysis of 3D printed mimics 22
2.3 Development of Computational Model 22
2.4 Extension to Microarchitectured materials 23
2.5 Results and Discussion 24
2.5.1 3D Printed Bone Mimics 24
2.5.2 Computational Verification of Damage Accumulation in Rod-like Trabeculae 25
2.5.3 Extension to Synthetic Lattice Structures 26
2.5.4 Inelastic Dissipation Energy 28
2.5.5 Statistical Analysis 29
2.6 Conclusions 31
3. MECHANICAL AND NEUROPHYSIOLOGICAL MECHANISMS IN MOSQUITO ANTENNAE PROMOTE THE DETECTION OF ACOUSTIC TARGETS AMIDST NOISE . 33
3.1 Introduction 33
3.2 Structural and Mechanical Characterization 34
3.3 Development of Computational Models 38
3.3.1 CAD Modeling 39

3.3.2 Boundary Conditions 39
3.3.3 Addition of hair and segments 40
3.3.4 Material Properties 41
3.4 Quantification of effect of individual structural features 42
3.5 Mechanical Vibration Response to Real World Stimuli 44
3.6 Electrophysiological transduction of flagellar vibration 47
3.7 Conclusions 51
4. MECHANICAL AND FUNCTIONAL EVALUATION OF WOODPECKER SKULL BONES 53
4.1 Introduction 53
4.2 Biological Observation 55
4.3 Development of Computational Model 56
4.3.1 CAD Model of 3D Composite Woodpecker Head 56
4.3.2 Design of Simplified CAD Geometries 58
4.3.3 Finite Element Modeling of 3D Composite CAD Model 59
4.3.4 Finite Element Modeling of Simplified Models 60
Frequency Modal Analysis 60
Ricker Pulse Analysis 61
4.4 Results and Discussion 63
4.4.1 Stress Wave Propagation in the 3D Composite Model 63
4.4.2 Frequency Modal Analysis of simplified model 64
4.4.3 Ricker Pulse Analysis of simplified model 65
4.4.4 Stress Wave Propagation in the simplified model 65
4.4.5 Effect of Frontal Overhang 66
4.4.6 Experimental Corroboration 69
4.5 Conclusions 69
5. MECHANICAL AND FUNCTIONAL EVALUATION OF THE STOMATOPOD TELSON: A BIOLOGICAL SHIELD 71
5.1 Introduction 71
5.2 Morphological Features 72
5.3 Development of Computational Models 73

5.3.1 3D Models 73
5.3.2 2D Plane Strain Models 74
5.4 Results and Discussion 75
5.4.1 Finite element Analysis on Effect of Ridge Geometry under quasi-static conditions 75
5.4.2 Analysis of telson geometries under impact conditions 79
Preliminary Simulations for effect of ridges in regions far from impact 80
Parametric Analysis for different loading directions 81
FE Analysis of effect of ridges at impact location 82
Analysis of Stress Wave Propagation during impact 83
Analysis of Simpler 2D Geometries for stress wave propagation 85
5.4.3 Effect of Ridged shells with viscoelastic cores 88
5.5 Conclusions 90
6. MECHANICS OF RIDGED SHELL METASTRUCTURES FOR TAILORABLE STIFFNESS AND ENERGY DISSIPATION 92
6.1 Introduction 92
6.2 Methods 94
6.2.1 Finite Element Modeling 94
6.2.2 Experimental 95
6.3 Results and Discussion 95
6.3.1 Response under pure bending 95
Opposite Sense Bending 95
Same Sense Bending 96
6.3.2 Dimensionless Analysis 97
Stiffness Response 99
Experimental Verification of Stiffness Response 102
Evaluation of Peak Moment and Energy Dissipation 102
6.4 Conclusions 104
7. SUMMARY AND CONCLUSIONS 106
REFERENCES 110
PUBLICATIONS 118

LIST OF FIGURES

Figure 2.1 : Microstructure of cancellous bone – a) Rod-like and plate-like struts, b) strut orientation relative to anatomical position. Work by A. Torres, Hernandez Group, Cornell University. Adapted from [42]..... 22

Figure 2.2 : a) 3D printed bone mimics, b) increases in fatigue life observed, with small changes in c) density and d) stiffness by increasing thickness of rod-like struts. Experiment performed by A. Torres, Hernandez Group, Cornell University. Adapted from [42]..... 25

Figure 2.3: Quantification of PEEQ reveals that plastic strain is concentrated and continues to increase only in transverse rods over 5 loading cycles. Y-axis values represent greyscale pixel values and are only representative of plastic strain. 26

Figure 2.4: a) Octet truss, b) Two bone-like unit cells designed that are combined into c) a 2x2x2 supercell. Stress triaxiality for d) cancellous bone, e) octet and f) bone-like architecture with red lines indicating values of +0.33 and -0.33. Inset: Respective FE meshes for each microarchitecture. g) Images of 3D printed samples for cancellous bone (top) and bone-like (bottom) architectures. Adapted from [44]..... 27

Figure 2.5: Transverse volume fraction influences fatigue life in repeating cellular solids. a) Bone-inspired microarchitecture and octet truss supercell cores. b) Fatigue life of lattice structures compared with and without thickened transverse struts. Also includes the effect of thickened oblique struts in the octet. Also shown are specific stiffness values. c) Fatigue life of these structures is related to inelastic dissipation energy per unit work. d) Inelastic dissipation energy and stress triaxiality are shown to stabilize within the first 25 cycles allowing us to draw useful conclusions without high computational expense. Symbols indicate bone (•), bone-like microstructure (▲) and octets (♦). Experimental data from A. Torres, Hernandez group, Cornell University. Adapted from [42]..... 29

Figure 2.6: Fatigue life for 3D printed specimens at different applied cyclic loads ($\sigma/E0$ in microstrains) is shown with lines indicating regression model fits. Statistical analysis by Hernandez group, Cornell University. Adapted from [42]..... 31

Figure 3.1: CT scan of the antenna of *Aedes aegypti* female mosquito highlighting individual structural and functional components of the antennal hearing system. 36

Figure 3.2: Sex and species-specific variation in response to pure tone sound for mosquito antennae. (A) Acoustic cues for two different species of mosquitos. (B) Scaled representations of antenna for males and females of each species. (C) Magnitude and phase of response to pure tone stimuli for vibrations measured at the tip (blue) and middle (violet) for each antenna via LDV. Experiment performed by H. Pantoja, Bernal Group, Purdue University. 38

Figure 3.3: CAD models were developed for male and female of both species of mosquitos studied. 39

Figure 3.4: Boundary conditions for the antennal models. 40

Figure 3.5: Quantification of variation in segment dimensions with segment number for one of the four antennae – the *A. aegypti* female. 41

Figure 3.6: Parametric analysis of effect of varying mechanical properties on vibrational response of the antenna. 400 Hz is the expected natural frequency for this model. Variations in elastic modulus of the cuticle show the largest difference in the overall vibrational response. 42

Figure 3.7: Effect of sensory hair and intersegmental variation on mechanical response of antennae to pure tones. (A) Three models for each antenna consisting of a base model with a rod of constant diameter (blue), a rod with varied diameters to mimic intersegmental variation (red) and a rod with segmental variation as well as sensory hairs (black). (B) Magnitude of velocity response to pure tone stimuli for all 3 variations for both sexes of both species extracted from the tip of the antenna. Dashed line indicates experimentally observed first natural frequency. (C) Phase response for all 3 variations for both sexes of both species extracted at the tip of the antenna. 44

Figure 3.8: Response of antennae to real world stimuli. (A) Wing beat tones for the *A. aegypti* male and female mosquitos. (B) Response of the antenna of the female *A. aegypti* to the tone of the male wing beat (blue) and to the tone of combined male and female wingbeats (red). (C) Response of the *A. aegypti* male antenna to the female wingbeats (green) and to the combined male and female wingbeats (blue). (D) Combined input tones for frog calls and *A. aegypti* female wing beats. (E) Combined input tones for frog calls and *U. lowii* female wingbeats. (F) Response of *A. aegypti* (blue) and *U. lowii* (red) female antenna models to input tones from (D) and (E) respectively. 46

Figure 3.9: Electrophysiological transduction model simulating the mechanisms at the JO. (A) Denotes the different sensory units in the JO, with descriptions of intra and extracellular recordings. Also depicts the non-linear transfer function between current and displacement. (B) Intra (yellow) and extracellular (blue) recordings comparing model with experimental data. Also depicts harmonic distortion in both intra and extracellular recordings. (C) Intermodulation distortion amplifies the difference between the input tones (f2-f1). (D) Comparison of electrical response and attenuation between target signal and intermodulation product for different linear and non-linear transduction functions. Model by H. Pantoja, Bernal Group, Purdue University. 49

Figure 4.1: A) Different skull bones of the woodpecker head. Adapted from *digimorph.org*. B) Different species of woodpecker showing different anatomical adaptations on the skull bone based on pecking habits. Analysis performed by JY Jung, McKittrick group, UCSD. Adapted from [62] 56

Figure 4.2: Reconstruction from μCT data to create CAD models. This example shows the reconstruction of the paraglossal bone, which is a constituent part of the hyoid bone in the woodpecker head. 57

Figure 4.3: Composite 3D model of the woodpecker head including all the constituent parts. ... 58

Figure 4.4: Three models of the skull bone for dynamic finite element analysis. (A) Model 1: Original reconstruction of the skull of the Golden Fronted Woodpecker. (B) Model 2: Model with small artificial overhang. (C) Model with large artificial overhang. The images on the right side are the view-cut sectional along the sagittal plane. 59

Figure 4.5: A) Two models of the skull bone with different frontal overhangs for dynamic finite element analyses. B) Node identification for regions of interest where 1: the caudal end of the upper beak bone, 2: on the parietal bone near the brain, 3: on the palatine bone and 4: on the jugal bone. Adapted from [62]..... 61

Figure 4.6: (A) Schematic illustration of the Ricker pulse input and the fixed end location considered for the ricker pulse analysis. (B) Time domain and (C) frequency domain characteristics of the ricker pulse.(D) Example of clear response using ricker pulse vs noisy data in a direct impact simulation..... 63

Figure 4.7: VonMises stress along different points along the composite woodpecker head model where 'a' is on the keratin sheath, 'b' is at the frontal overhang, 'c' is on the jugal bone, 'd' is on the skull bone and 'e' is on the hyoid bone. 64

Figure 4.8: Computational results of impact testing. A) Five natural frequencies of the woodpecker skull. B) A representative result of Ricker pulse analysis at nodes 1 and 2. C) Plots of von Mises stress at four nodes. D) Time-lapse of von Mises stress distribution on the skull bone models at impact speeds of 7 m/s. Parts C and D performed by A. Pissarenko, UCSD. Adapted from [62]66

Figure 4.9: : Effect of frontal overhang. Comparison of dominant frequencies at the four regions of interest (inset in first plot) between woodpecker models with and without overhang show no major differences while maintaining the same frequency isolation characteristics around the brain (node 2). 68

Figure 5.1: Telson overview and comparison of bulk morphologies, (A) Smashing type (*O. scyllarus)* mantis shrimp. (B) Hammer-like dactyl appendage of smasher stomatopod. (C) Spearing type (*L. maculata)* mantis shrimp. (D) Spear-like dactyl appendage of spearer stomatopod. (E) Telson of smasher stomatopod. (F) Polished transverse cross section of the smasher telson with plane of section denoted by dashed line in (E). (G) Telson of spearer stomatopod. (H) Polished transverse cross section of the spearer telson with plane of section denoted by dashed line in (G). Inset: Higher magnification optical micrograph of dorsal cuticle along center line. Micrography performed by N. Yaraghi, Kisailus group, UC Riverside. Adapted from [38]..... 73

Figure 5.2: Strain rate dependent and distinct regions of shear moduli for the viscoelastic material used in simulations under impact..... 75

Figure 5.3: FE simulations on the effect of carinae geometries on stiffness. (A) Representations of CAD models used in the FE simulations with nomenclature. (B) Mean stiffness for top loading up to 0.5 mm displacement (inset: boundary conditions). (C) Mean stiffness for lateral loading up to 0.5 mm displacement (inset: boundary conditions) (D) Percentage change in stiffness as compared to the SMSH model under top loading. Corresponding change in stiffness for spearer geometry obtained from experimental data under top loading has been highlighted. (E) Percentage change in stiffness as compared to the SMSH model under lateral loading. Adapted from [38]..... 78

Figure 5.4: Comparison of experiments of 3D printed telson structures with simulation data indicating percentage change in stiffness as compared to the original ridged geometry shows good qualitative agreement with some variation for initial stiffness under quasi-static loading conditions. Color of curves indicate similar geometries in experimental and simulation with lighter color variants indicating experiment. Left bar shows 3D printed specimens while bottom bar shows 3D FE models. Experimental data acquired from J. Rivera, Kisailus group, UC Irvine..... 79

Figure 5.5: (A) Construction of two variations of 2D plane strain models from cross-sections of the smashing type telson. (B) Boundary conditions and data extraction points 80

Figure 5.6: (A) Indicates accelerations and shear strain at the midpoint of the telson geometries for ridged (blue) and smooth (orange) models. (B) Indicates accelerations on the telson shell at a region far from impact with magnification of acceleration data inset. 81

Figure 5.7: Parametric analysis for different loading directions. (A) Indicates different loading conditions considered. A total of 20 simulations were conducted with 5 of them being shown above indicated by red lettering. (B)-(F) Shear strain on the left telson shell at different loading directions for ridged vs smooth telsons. 82

Figure 5.8: Deformation of telson side wall during impact at impact location for the ridged telson model (top) and smooth telson (bottom)..... 83

Figure 5.9: Differences in stress wave speed between ridged and smooth telsons. Grey indicates stress wave front. 85

Figure 5.10: Three designed geometries tested under impact with boundary conditions shown on the right. 86

Figure 5.11: Frequency modal analysis for smooth, ridged and sinusoidal geometries shows the presence of a new mode (mode 5) in sinusoidal and ridged geometries that is consistent with flattening of the ridges. 87

Figure 5.12: Principal stress magnitude and directions for ridged, smooth and sinusoidal models at three different time steps of the simulation..... 88

Figure 5.13: : Equivalent strain comparison between ridged and smooth box geometries. Inset: The box geometries with red circle indicating set of nodes from where data was extracted..... 89

Figure 5.14: Viscous dissipation energy for the ridged vs smooth cylinder models. 90

Figure 6.1: 3D ridged shell structure designed from telson side wall and extruded in the z-direction. Also shown are the different geometrical parameters that are used in this study..... 94

Figure 6.2: Moment vs Rotation plots in opposite sense and same sense bending for varying ridge radii from r = 0 to r = s. Inset in blue is a characteristic hysteresis loop for one of the ridged geometries 97

Figure 6.3: (A) Stiffness response for varying ridge size for same and opposite sense bending. (B) Schematic describing movement of material points for models with $\pi 3$ lower or higher than 0.275. (C) Principal stress directions for models at $\pi 3$ lower or higher than 0.275 where red indicates compressive stress and blue indicates tensile stress. 101

Figure 6.4: Experimental verification of stiffness response. (A) Load-displacement data from experiments converted into moment rotation data and shows good match with simulations. (B) Stiffness calculated from the experimental data shows expected trend..... 102

Figure 6.5: (A) Varying ridge size ($\pi 3$) vs normalized peak moment for same and opposite sense bending. (B) varying ridge size ($\pi 3$) vs normalized energy dissipation for same and opposite sense bending. Inset: Highlights normalized energy dissipation for reference geometries ($\pi 3 = 0$).. 104

ABSTRACT

Biological materials are built from a fairly small number of naturally occurring elements and compounds. To compensate for the lack of diversity in these building blocks, biological organisms, through millions of years of evolution and natural selection have evolved a wide range of innovative structures to achieve optimized performance in interacting with their natural environments. The focus of this work is on understanding the evolution strategies employed by natural organisms that encounter dynamic mechanical loads such as impact events, repeated cyclic loading events and structures that are tuned to harness mechanical vibrations. Insights gleaned from understanding the mechanisms involved can find potential applications towards lightweight structural materials and mechanical sensors.

We study cancellous bone, a naturally occurring lightweight micro-architected material and show that resistance to fatigue failure is sensitive to a microarchitectural trait that has negligible effects on stiffness and strength – the proportion of material oriented transverse to applied loads. Using models generated with additive manufacturing, we show that small increases in the thickness of the elements oriented transverse to the loading direction can increase fatigue life by 10 to 100 times. We show that the mechanism can be extended to synthetic microlattice structures, where fatigue life can be enhanced by 5 to 9 times with only negligible changes in stiffness and strength.

Another interesting field of study are natural structures tuned to harness mechanical vibrations. Mosquitos lack tympanic ears to detect sound. Instead, they rely on their plumose antennae, light-weighted sensory structures which detect sound induced air vibrations. Mosquitos use audition in different behavioral contexts. Here, we study the antenna of two species known to use hearing for different functions. Through the use of geometrically accurate computational models, we find that the mechanical design of the antenna is associated with the specific biological function of hearing in each species. Structurally, intersegmental variation and sensory hairs in the antenna are responsible for increased sensitivity and tuning of the mechanical response. Mechanical and neurophysiological mechanisms promote the detection of specific acoustic cues amidst the noise produced by their own wingbeats.

Finally, we focus our efforts on natural structures that encounter high-energy impact loading in their ambient environments. Woodpeckers are known to peck at trees every day through their 15-year lifespan while showing no evidence of brain damage. High fidelity finite element simulations in combination with an additive manufacturing experimental approach is utilized to unveil two main features in the woodpecker head that may contribute to the absence of brain damage; the bar structure of the jugal bone acting as a stress deflector and the high natural frequency in the skull bone acting as a frequency isolation tool.

Another natural organism that encounters high-energy impacts is the mantis shrimp. This aggressive marine crustacean utilizes a shield-like segment of its abdominal armor called the telson to defend itself from blows of conspecifics during ritualized fighting. We quantify the effect of ridges present on the dorsal surface of the telson. First, we show that ridges play a role in modulating stiffness of the mechanical system dependent on the point of application of the load. Second, under dynamic loading, ridges may act as wave traps retarding the propagating stress wave to prevent significant damage to the telson under impact. Finally, we extend the concept of the ridged geometry to bio-inspired curved shells, where we show an interplay between competing mechanisms that allows such structures to show the potential for large energy dissipation within controlled stiffness bounds.

1. INTRODUCTION

1.1 Natural Materials

Natural materials have undergone close to 4 billion years of evolution and natural selection to achieve optimized performance when responding and interacting with their complex environments. The functional diversity in these materials has allowed them to be a source of inspiration for solving challenges in various scientific fields and indeed, to tackle complex multidisciplinary problems that stretch across fields. Many biological materials have shown to possess mechanical properties that far surpass those that are achievable using similar synthetic materials[1], [2]. This is surprising, given that natural materials consist of relatively few constituent elements, which combine to create a set of polymers, minerals or a composites of polymers and ceramic particles that are considered quite weak[1], [3]–[6]. The limited strength is due to a combination of the ambient temperature, aqueous environment processing and the limited availability of elements. To compensate for the lack of diversity in their building blocks, natural organisms have evolved structures that incorporate unique and elegant architectures that provide remarkable mechanical properties such as stiffness, toughness and durability surpassing those of their components by orders of magnitude and yet remain lightweight. Wegst and Ashby[7] provide an apt example to illustrate the effect of structural variation in such materials. They compare skin, tendon and cartilage which all consist of the same constituent building blocks; collagen and elastin. What varies is the fractions and structure of each component resulting in distinctly different mechanical responses for each of these materials. Tendon and ligaments are both designed to transmit tensile forces, while skin is able to deform in all directions without requiring elongation of individual collagen fibers and cartilage is designed for sites where flexibility and shape recovery are of prime importance.

These combinations of structures and materials lead to unique and interesting properties that are not commonly seen in engineered materials. For example, most engineering materials display an inverse relation between stiffness and toughness. Materials such as ceramics, that show high stiffness and strength exhibit brittle behavior. However, for natural materials, the inverse relationship between these mechanical properties has not been observed. This builds a roadmap towards building high strength and stiffness materials without sacrificing toughness[7], [8]. The

key to these unique properties is hidden in the hierarchy of biological materials. In biological systems, the structure and material are intricately linked across length scales while for engineering materials, a distinction is drawn between mechanical engineers as structural engineers and materials engineers who for the most part, independently operate in their scientific disciplines. Hierarchy plays a large role in the mechanical response of biological materials. Several studies have demonstrated the ability of natural materials to combine high stiffness with high toughness allowing them to be extremely damage tolerant. Freshwater fish such as *Arapaimas gigas* have developed tough protective layers known as elasmoid scales to protect against piranhas[8], [9]. Bone and nacre have been extensively studied for their combined high stiffness and strength arising from distinct mechanical behavior at different length scales[10]–[13]. The dactyl club of the mantis shrimp has one of the most powerful strikes in the animal kingdom, and also contains a hierarchical structure consisting of a bouligand architecture that accounts for their exceptional damage tolerance[14].

Another defining characteristic of biological materials is their multifunctionality[1], [2]. For example, bones provide structural support as well as assist in blood cell formation. Insect antennae can detect chemical and thermal information from their environment and at the same time, can act as hearing organs for certain insects[15]. The characteristic multifunctionality must be taken into account when considering, evaluating and studying structure-function relationships in such biological organisms.

Many investigators have characterized the structures of these natural materials such as mollusk shells, bone, bird beaks, and fish scales[16]–[19] in an attempt to mimic the behavior. Yet, few have attempted to quantify the critical mechanical properties and parameters governing the mechanical performance which is integral to apply these bioinspired strategies to engineering materials and design. Arguably, success stories of bioinspired design consist of those that have focused on nature inspired structures such as Velcro, with its hook and loop architecture rather than materials. These strategies have found success by attempting to exploit one design feature of the natural structure rather than attempting to mimic the material in its entirety.

In this vast space of biological and bioinspired materials, there is a subset of those biological organisms that encounter dynamic mechanical loads such as cyclic loading, mechanical vibrations and high energy impact events during their lifetimes as part of their ambient environment. For such organisms, there is a large amount of information and insight that can be mined by observing their

structures under their natural boundary conditions and unveiling their structure-function relationships.

1.2 Natural Materials for Durability and Fatigue life

In the new and burgeoning field of microarchitected materials, natural materials also provide some valuable insights. Microarchitected materials can achieve high stiffness and specific strength (strength per unit mass) through the manipulation of the underlying geometry[20]–[22]. However, the designers of such microlattice structures do not generally consider resistance to fatigue life. Applying such structures to durable devices such as vehicles will require a larger consideration of fatigue life. Previous work investigation fatigue in architected materials has shown that porosity and unit cell type are significant indicators of fatigue life[23]. Ahmadi et al[24] also found that surface roughness during the manufacturing process was relevant to fatigue life. However, an understanding of life cycles of natural foams may further enhance the understanding of fatigue in architected materials. Bone is a biological material with high stiffness and strength relative to density. Whole bones consist of an outer shell made of dense tissue known as cortical bone that surround a foam-like tissue known as cancellous bone. Although the effect of microarchitecture on the mechanical performance of cancellous bone has been well studied[25], its effect on fatigue life has not been as well studied. Insights gleaned from the study of cancellous bone could be extremely beneficial in furthering the understanding of fatigue in microarchitected materials.

1.3 Natural Materials that harness Mechanical Vibrations

Another interesting mechanical interaction between biological structures and their natural environments can be seen in mosquito hearing organs. Insect hearing organs can be divided into two distinct classes; tympanal ears, which are sensitive to pressure waves in sound, and particle velocity receivers which are sensitive to oscillations of air particles in the sound field[26]. Particle velocity receivers are generally light structures such as antennae that are deflected by sound induced vibration of the air particles. Understanding and unravelling the inherent mechanical behavior can provide inspiration for innovative designs in microphone technology. Avitabile et al[27] provided an analytical framework for the description of antennal hearing system in mosquitos, but did not include a structural and morphological description of the antenna. Saltin et

al[28] provided mechanical stiffness correlations using confocal laser scanning microscopy while Su et al[29] reported a quantitative analysis of mechano-transducer function in several species of mosquitos. Yet, a detailed explanation unveiling the mechanisms that promote the detection of acoustic targets in mosquitos is still lacking.

1.4 Natural Materials exhibiting Impact Resistance

Woodpeckers peck at trees every day throughout their lifespan, and yet, amazingly, show no evidence of traumatic brain injury (TBI) or concussions in their brains[30]. During pecking, the woodpecker head reaches decelerations up to 1200 g, 7 m/s impact speeds and pecking rates around 20 Hz[30]–[32]. There is immense value, then, to determine the mechanical characteristics that the woodpecker has developed and employ them in the development of better shock absorption systems for the protection of the human head. Scientists have attempted to understand and identify key elements of the woodpecker's shock tolerance through a biomechanical approach and have provided some good insights such as the presence of a specialized hyoid apparatus[33], the inclusion of a spongy bone surrounding the brain[34], and an adaptive bill shape and relative movement between the skull and the upper jaw[35] that could account for some of the shock absorption characteristics. While these may be partial explanations of the mechanistic behavior, a full determination of the structure-function relationship is still lacking.

Stomatopods, colloquially referred to as mantis shrimp use a set of highly developed appendages known as dactyl clubs during hunting and fighting[14], [36], [37]. Along with this offensive weapon, stomatopods also possess a shield like terminal segment of abdominal armor called the telson which they use as a shield for personal protection during ritualized fighting with conspecifics. Telsons face impacts from the dactyl club reaching velocities of 23 m/s and peak forces up to 1500 N[38]–[41]. An investigation into the structural behavior of the telson may open more avenues for development of materials for impact resistance and damage mitigation. Taylor and Patek examined the mechanical impact properties of the telson through measurements of the coefficient of restitution which revealed an inelastic response of the telson structure, allowing it to effectively absorb and dissipate 69% of the impact energy[41]. Through micro-CT measurements, morphological features including ridge-like regions called carinae were identified within the telson structure which could provide the combination of stiffness and compliance necessary for energy

absorption. However, the mechanisms underlying the telson's resistance to impacts and the specific role of the carinae is yet to be uncovered.

1.5 Motivation

Biological organisms have optimized their structures over millions of years of evolution to withstand forces in their natural environments. Since natural materials consist of relatively few constituent building blocks, there is a need to adapt structures to withstand loads. Natural materials showcase unique, remarkable and non-intuitive mechanical properties simply through variations in their structure and architecture. Specifically, for the durability displayed by cancellous bone, the acoustic sensitivity exhibited by mosquito antennae, and the impact resistance displayed by the woodpecker and mantis shrimp, while previous work has built a base of knowledge for the mechanical behavior, studying, understanding and unveiling the mechanisms at play during dynamic mechanical events can inspire new and innovative solutions in our design of synthetic structures and materials.

The aim of this body of research then is to employ computational techniques and novel methodologies to analyze the structures present in these natural organisms that contribute to their dynamic mechanical response, identify their structure-function relationships to extract the key structural parameters, and to build mechanistic explanations for their deformation behavior for future use in applications towards lightweight structural materials and mechanical sensors.

1.6 Objectives

With the above goals in mind, this work has the following three objectives:

1. Use mechanics as a tool to understand structural adaptations of organisms that allow them to survive and thrive when subject to dynamic mechanical events in their natural environments.

    With this objective, computational techniques are utilized to run systematic sets of simulations to differentiate responses between the various structural adaptations in these organisms and quantify the differences.

2. Identify the governing structural parameters and mechanisms responsible for the mechanical behavior and build mechanistic explanations for the deformation behavior and structure – function relationships.

   This objective aims to identify those structural adaptations that may be key to the deformation behavior, understand the mechanisms involved, and expand the understanding into a mechanical framework.

3. Extrapolate the mechanisms to biomimetic and bioinspired structures for future applications in lightweight structural materials or mechanical sensors.

   This objective then aims to extend the mechanisms found in biological organisms that resist dynamic mechanical loads to biomimetic and bioinspired structures to take the first step towards incorporation into synthetic materials and structures for applications such as lightweight structural materials and mechanical or acoustic sensors.

1.7 Outline

This dissertation is divided into seven chapters. A quick road map is as follows:

- Chapter 2: This chapter investigates the ability of cancellous bone in withstanding multiple cycles of loading and identifies key structural parameters responsible for the behavior. This work was in collaboration with Hernandez Group from Cornell University.
- Chapter 3: This chapter concerns how mosquitos use their antennae for hearing and identifies mechanisms that allow mosquitos to capture acoustic cues despite the presence of noise. This work is in collaboration with Bernal group from Purdue University in the department of biology.
- Chapter 4: This chapter investigates the ability of the woodpecker to withstand repeated pecking with no brain damage and identifies structural variations that contribute to the shock absorption. This work is in collaboration with the Restrepo group from the University of Texas, San Antonio as well as McKittrick group from the University of California, San Diego
- Chapter 5: This chapter investigates the effect of ridges in the mantis shrimp telson that allows it to withstand high-energy impacts. This work is in collaboration with the Restrepo

group from the University of Texas, San Antonio as well as Kisailus group from the University of California, Irvine.

- Chapter 6: This chapter extends the concept of ridged geometries inspired from the mantis shrimp telson from chapter 5 to 3D curved shells and identifies competing mechanisms involved that allow such curved ridged shells to display large energy dissipation within controlled stiffness bounds.

2. BONE INSPIRED MICROARCHITECTURES ACHIEVE ENHANCED FATIGUE LIFE

Parts of chapter 2 are included in the publication – A.M Torres, A. A Trikanad, C. A. Aubin, F. M. Lambers, C. M. Rimnac, P. Zavattieri, C. J. Hernandez, "Bone inspired microarchitectures achieve enhanced fatigue life". Proceedings of the National Academy of Sciences, 116(49), 201905814, (2019) [42]

2.1 Introduction

Microarchitectured materials achieve excellent mechanical properties such as high stiffness and strength per unit mass through geometry rather than composition[21]. With recent developments in additive manufacturing and design software, there has been a rise in optimized architectures to meet stiffness, strength and energy absorption demands with low density microarchitectures[20]–[22]. However, resistance to fatigue failure is not often considered in the design of lattice microstructures. Microarchitectured materials can be susceptible to fatigue failure because their complex geometries can cause large stress concentrations promoting the initiation and propagation of damage[17]. Cancellous bone is a naturally occurring foam-like material which consists of a network of plate-like and rod-like trabeculae in different orientations (Figure 2.1). These trabeculae are preferentially aligned in the direction of stresses generated during habitual physical activity. Here we study the effect of microarchitecture on the fatigue properties of cancellous bone, in an effort to draw useful parallels to microarchitectured materials. To better understand the effects of microarchitecture on fatigue life, our collaborators performed fatigue damage processes in high porosity (>90%) cancellous bone[42]. Cyclic compressive loading was applied in the direction of habitual loading and microdamage was detected within the structure with contrast agents. It was observed that the amount of tissue damage was reduced in specimens having thicker horizontal rod-like struts. This finding was surprising since rod-like struts, on average, constitute only 20% of the solid volume of cancellous bone, with negligible effects on stiffness and strength in the longitudinal direction[43]. These findings suggest that in cancellous bone, transversely oriented struts act as sacrificial elements during cyclic loading by accumulating tissue damage and protecting the load-carrying longitudinally oriented plate-like trabeculae.

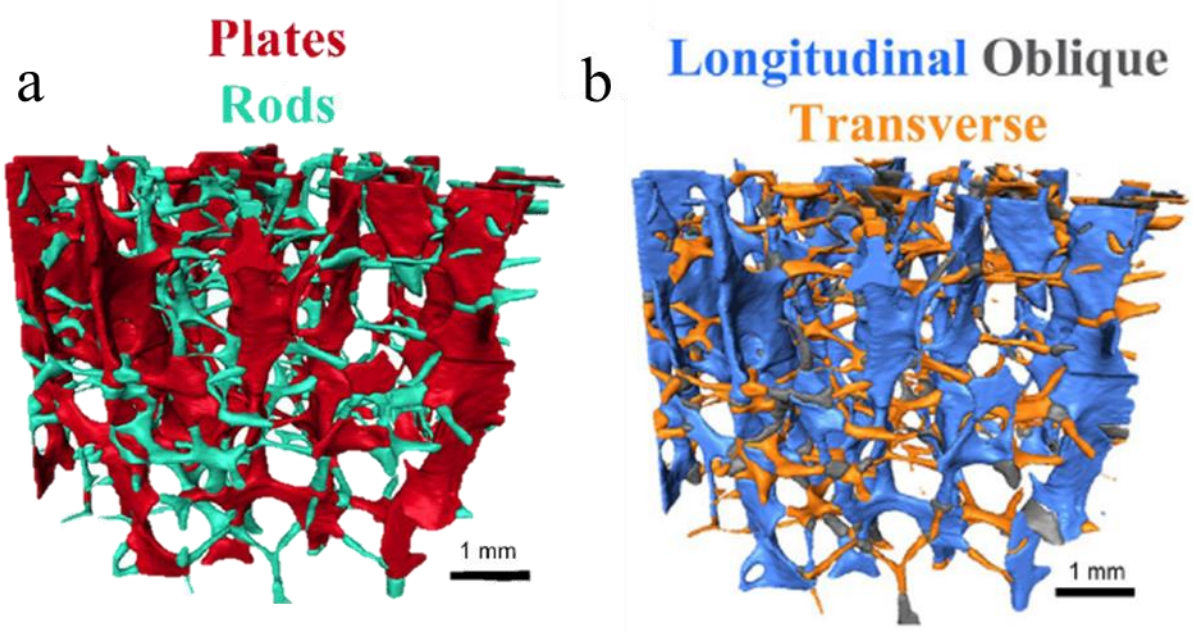

Figure 2.1 : Microstructure of cancellous bone – a) Rod-like and plate-like struts, b) strut orientation relative to anatomical position. Work by A. Torres, Hernandez Group, Cornell University. Adapted from [42]

2.2 Experimental Analysis of 3D printed mimics

Since bone also contains tissue heterogeneity which could contribute to damage accumulation[17], the microstructure of bone was mimicked and 3D printed using a high-resolution SLA printer. Our collaborating research group then performed similar fatigue testing. Fatigue loading was applied between 0 N and a compressive load corresponding to $\sigma = E_0 * 0.0035$ mm/mm, where σ is the stress and E_0 is the initial Young's modulus of the specimen. To test the observation that damage accumulation in the transversely oriented rods, some microstructures were modified by adding material to the surface of transverse rods. Because transverse rods constitute only a small portion of the total solid volume, and contribute very slightly to resisting loads, the addition of the material had a very small effect on the overall density and apparent stiffness of the microstructure.

2.3 Development of Computational Model

To assess the effect of damage accumulation in transverse rods, a computational model was designed. CAD models of bone microstructure were created through a conversion from imaging data using custom MATLAB scripts and reverse engineering software. From the CAD models,

finite element meshes were created consisting of about 1.5 million C3D8 brick elements. Cyclic compressive loading was applied consistent with the loading rate applied during experiments. The material was assumed to be elastic – perfectly plastic with a Young's modulus of 600 MPa and a yield stress of 26 MPa consistent with material properties of the 3D printing polymer. Classification of transverse, longitudinal and oblique rods and plates from the computational model was accomplished through the use of custom image processing MATLAB scripts that compared images of the bone microstructures to the computational models to determine elements corresponding to each of the structural members. Damage was quantified by measuring the accumulation of equivalent plastic strain (PEEQ) in each of the structural members as well as the inelastic dissipation energy for the complete model (ALLPD).

2.4 Extension to Microarchitectured materials

In an effort to characterize if this effect is generalizable to synthetic microlattice structures, bone like microarchitectures were derived from an octet truss - a well-known and well-studied lattice structure[22]. The length of the octet truss was elongated along the longitudinal axis by 40% so that struts were oriented 60 degrees from the transverse plane, thereby mimicking longitudinal elements seen in cancellous bone. To further match the architecture of cancellous bone, 6 plates were added per octet. The resulting supercell achieved porosity, transverse volume fraction, longitudinal volume fraction and plate volume fraction similar to cancellous bone specimens. Simple octet trusses were utilized as another component of the study. These three types of structures, namely, the bone microstructures, the bone-like architecture material and the octet trusses then represented a large design space of microlattice structures with distinctly different deformation behaviors. To characterize the primary deformation mechanism (bending dominated vs stretching dominated) within each lattice structure, stress triaxiality was determined at each point within every model. Stress triaxiality is defined as:

$$Triaxiality = -\frac{p}{q}$$

where p is the hydrostatic stress defined as positive when stress is compressive and q is the von Mises stress. By this definition, points under uniaxial tension would show a triaxiality of +0.33 and points under pure uniaxial compression would show a triaxiality of -0.33.

2.5 Results and Discussion

2.5.1 3D Printed Bone Mimics

Figure 2.2 describes the results of experimental analysis on the 3D printed bone mimics. Thickening of the transverse rod-like struts had only a small effect on the density (Figure 2.2C) and apparent stiffness (Figure 2.2D), but showed a disproportionately large increase in fatigue life, in some cases by two orders of magnitude (Figure 2.2B). Since previous finite element simulations have shown that transversely oriented rod-like trabeculae are primarily subjected to tensile stresses, these finding indicate that small increases in mass applied to these transversely oriented structural components of the microstructure can cause a reduction in tensile stresses, thereby leading to disproportionately large increases in fatigue life.

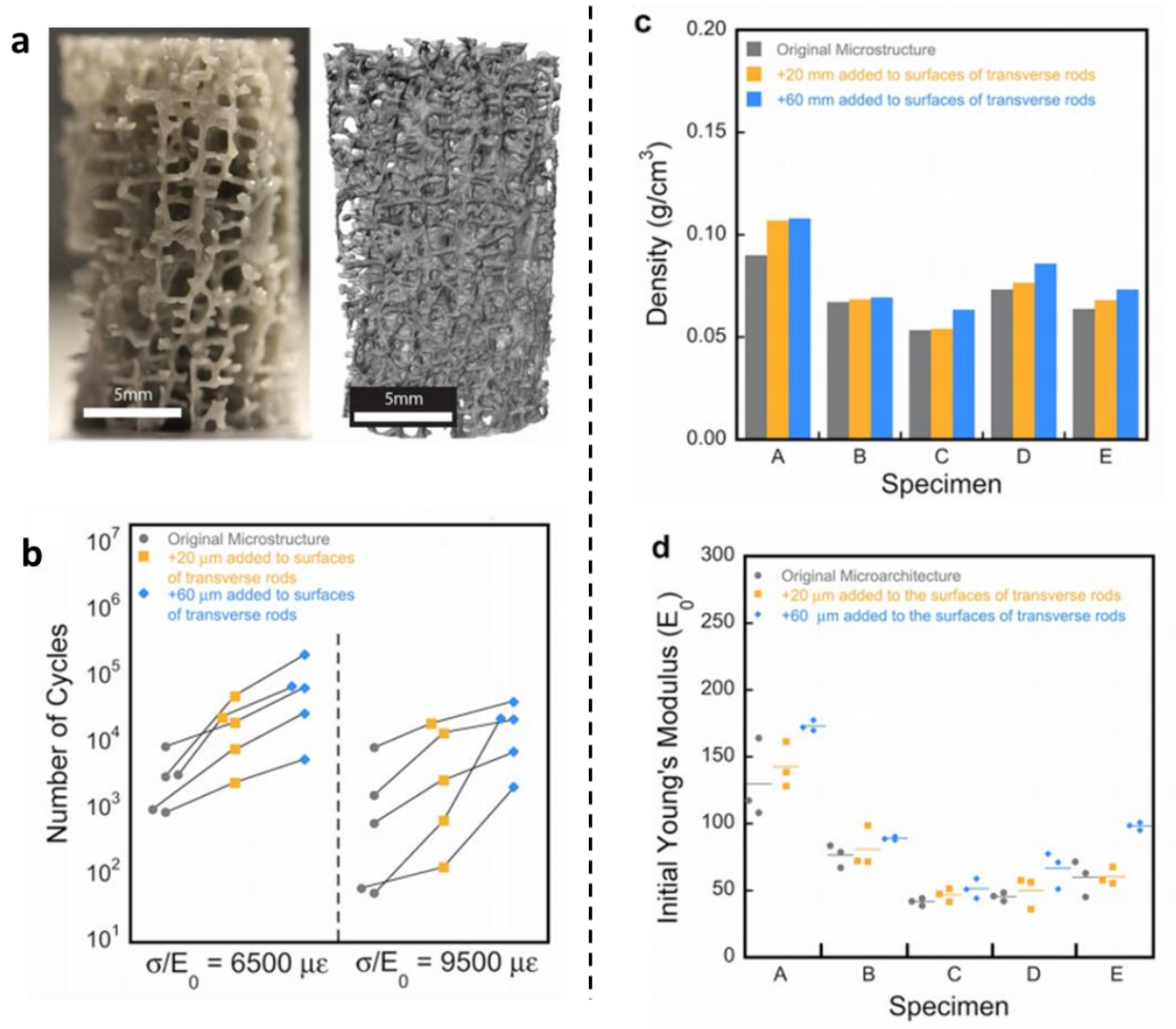

Figure 2.2 : a) 3D printed bone mimics, b) increases in fatigue life observed, with small changes in c) density and d) stiffness by increasing thickness of rod-like struts. Experiment performed by A. Torres, Hernandez Group, Cornell University. Adapted from [42]

2.5.2 Computational Verification of Damage Accumulation in Rod-like Trabeculae

To further validate the assertion that damage under cyclic loading was concentrated in rod-like trabeculae, finite element simulations of the bone architectures was performed with an elastic-perfectly plastic material matching the mechanical properties of the 3D printing polymer. While FE simulations did not account for damage, accumulation of damage was quantified by the presence of plastic strain. The equivalent plastic strain (PEEQ) is a scalar quantity used to represent a material's inelastic deformation. Quantification of the PEEQ revealed that plastic strains were

indeed dominated in transverse rod-like trabeculae while remaining constant in the other structural components (Figure 2.3).

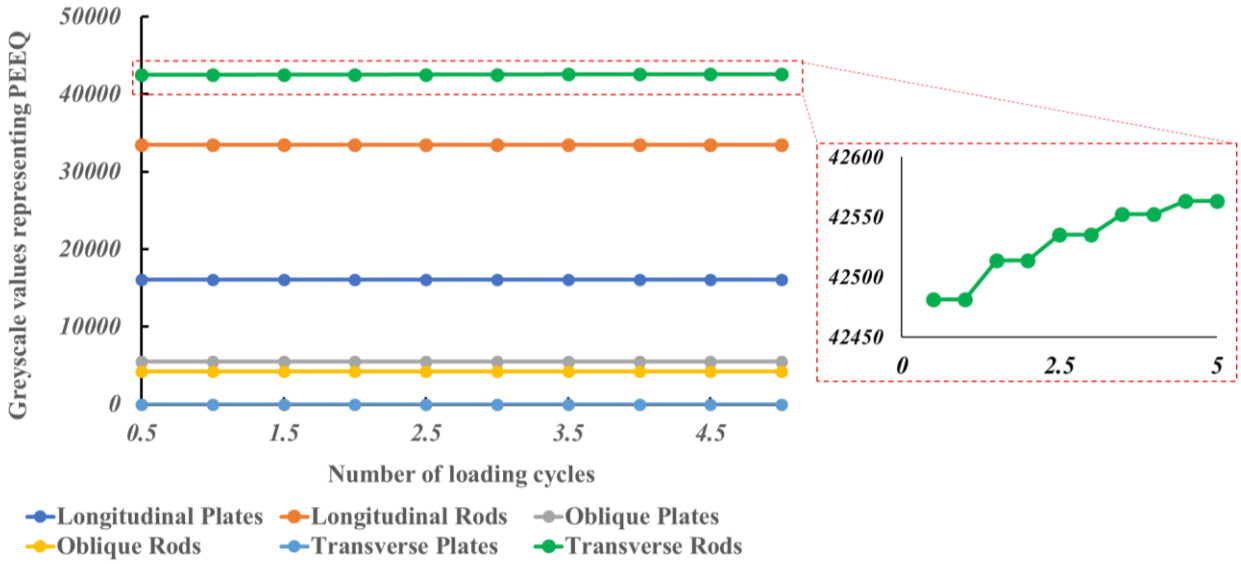

Figure 2.3: Quantification of PEEQ reveals that plastic strain is concentrated and continues to increase only in transverse rods over 5 loading cycles. Y-axis values represent greyscale pixel values and are only representative of plastic strain.

2.5.3 Extension to Synthetic Lattice Structures

To determine if these findings would extend to synthetic lattice microstructures and cellular foams with different deformation behaviors (bending dominated vs stretching dominated), we utilized models of an octet truss (Figure 2.4A), and a modified architecture of the octet truss designed to have plate-like and rod-like trabeculae similar to cancellous bone architectures (Figure 2.4B, 2.4C). Triaxiality results showed that the octet truss is stretching dominated, cancellous bone specimens are bending dominated, and the bone-like architectures show a combination of the two deformation behaviors. (Figure 2.4 D, E, F).

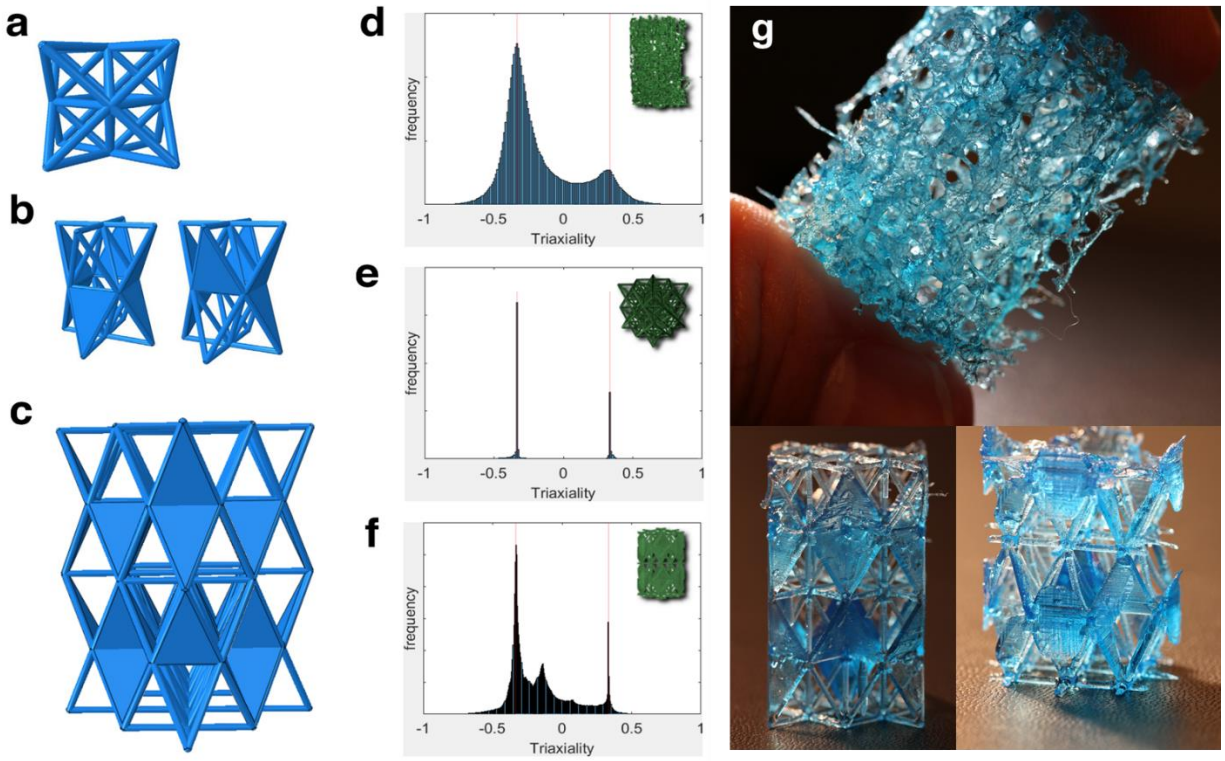

Figure 2.4: a) Octet truss, b) Two bone-like unit cells designed that are combined into c) a 2x2x2 supercell. Stress triaxiality for d) cancellous bone, e) octet and f) bone-like architecture with red lines indicating values of +0.33 and -0.33. Inset: Respective FE meshes for each microarchitecture. g) Images of 3D printed samples for cancellous bone (top) and bone-like (bottom) architectures. Adapted from [44]

In the bone-like architectures, increases in transverse rod thickness resulted in increased fatigue life by a factor of 8 (Figure 2.5B) with small changes in density (4%) and apparent stiffness (20%). In octet trusses, increase in transverse rod thickness resulted in increased fatigue life by a factor of 5 with small changes in density (10%) and apparent stiffness (14%). Interestingly, when the octet truss model containing thickened rods was rotated by 90 degrees so that thickened elements were vertically oriented and acting oblique to the applied loads, there was a decrease in fatigue life by a factor of 9 when compared to the model without thickened transverse rods (Figure 2.5B). This implies that the effect of transverse elements on fatigue life is related to the proportion of material oriented transverse to loading rather than thickness of transverse struts.

2.5.4 Inelastic Dissipation Energy

To characterize the influence of transversely oriented material on the fatigue damage accumulation, we performed finite element simulations of cyclic loading. Fatigue damage consists of a local irreversible energy-dissipating process resulting in increases in inelastic dissipation energy. Inelastic dissipation energy is defined as that portion of the internal strain energy which is dissipated by rate dependent and rate independent plastic deformation and is given by

$$E_p = \int_0^t \left(\int_V \sigma^c : \dot{\varepsilon}^{pl} dV \right) d\tau$$

where E_p is the inelastic dissipation energy, σ^c is the stress derived from the constitutive equation, and $\dot{\epsilon}^{pl}$ is the plastic strain rate. These properties being integrated in time and over the volume of the specimen. FE models of the first 25 loading cycles showed that fatigue life of octet and bone-like architectures is closely related to a dimensionless parameter; the ratio of inelastic dissipation energy to work done (calculated as the area enclosed by the load-displacement curve) as shown in figure 2.5C. Although these models were limited to the first few loading cycles, inelastic dissipation energy and stress triaxiality were shown to stabilize by this point (figure 2.5D).

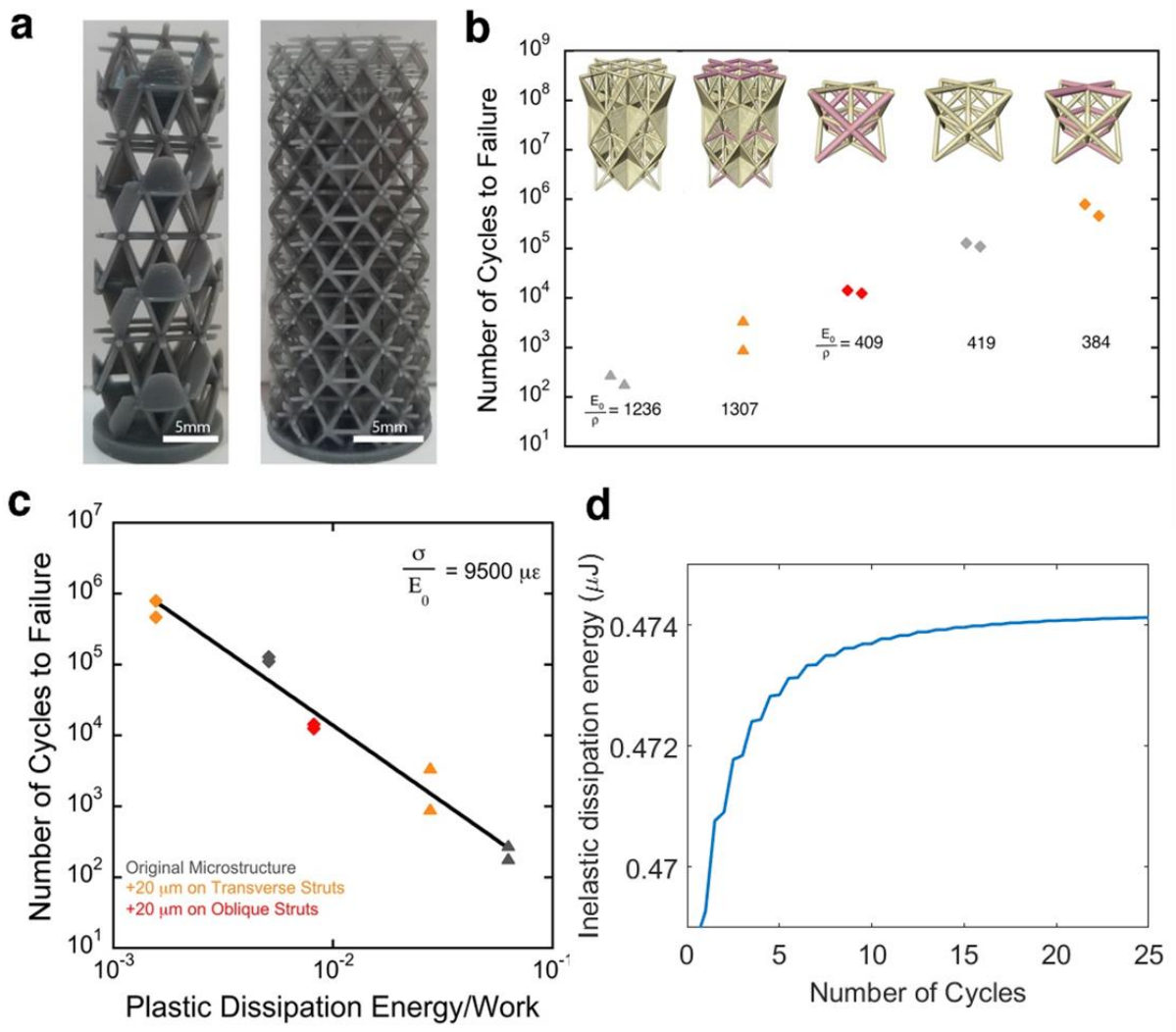

Figure 2.5: Transverse volume fraction influences fatigue life in repeating cellular solids. a) Bone-inspired microarchitecture and octet truss supercell cores. b) Fatigue life of lattice structures compared with and without thickened transverse struts. Also includes the effect of thickened oblique struts in the octet. Also shown are specific stiffness values. c) Fatigue life of these structures is related to inelastic dissipation energy per unit work. d) Inelastic dissipation energy and stress triaxiality are shown to stabilize within the first 25 cycles allowing us to draw useful conclusions without high computational expense. Symbols indicate bone (•), bone-like microstructure (▲) and octets (♦). Experimental data from A. Torres, Hernandez group, Cornell University. Adapted from [42]

2.5.5 Statistical Analysis

Our collaborating research used a Generalized Least squares model (GLM) to identify the empirical relationship between stress amplitude (denoted by σ/E_0), transverse volume fraction

(denoted by ψ) and number of cycles to failure (N_f) [42]. To account for differences in number of samples for each microstructure, microstructure was included as a random effect using REML. Previous work has empirically identified the fatigue life of foams via normalized stress vs life (S-N) relationships of the form[45]:

$$\frac{\sigma}{E_0} = AN_f^B$$

where σ is the maximum compressive stress, E_o the initial Youngs modulus, N_f is number of cycles to failure and A and B are empirical constants which differ among microstructures. Data from this work was used to develop an empirical model to characterize the same relationship and the regression models were able to identify a predictive equation only slightly differing from the equation above:

$$\frac{\sigma}{E_0}\frac{1}{\sqrt{\psi}} = AN_f^B$$

with $R^2 = 0.82$. Where A and B are empirical constants and ψ denotes the transverse volume fraction (Figure 2.6). There remains some unexplained variance likely due to differences in stress among bone, bone-like and octet trusses. Yet, this modification to the normalized S-N relationship provides a simple means of considering fatigue life during the design of microarchitectured materials.

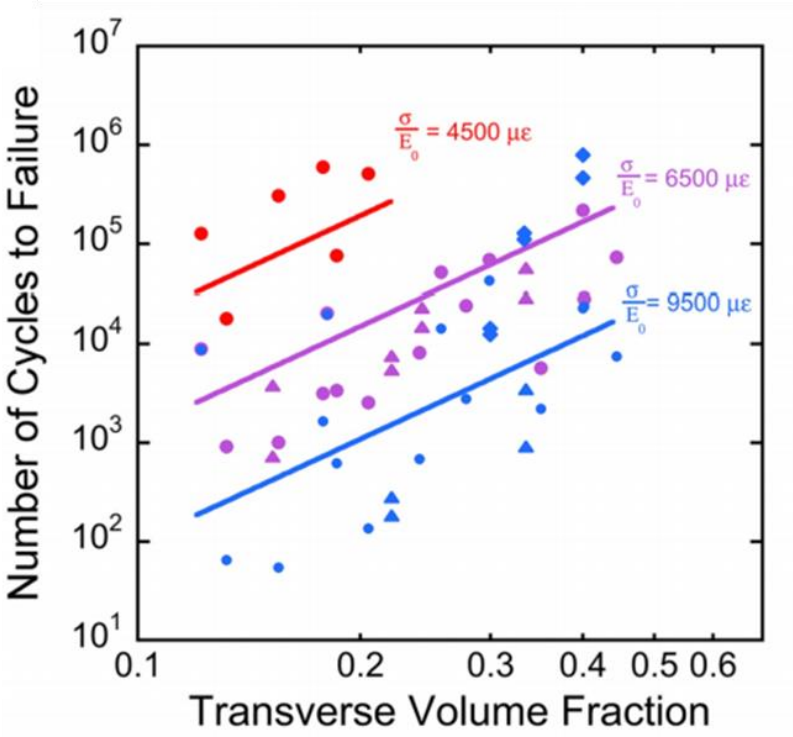

Figure 2.6: Fatigue life for 3D printed specimens at different applied cyclic loads (σ/E_0 in microstrains) is shown with lines indicating regression model fits. Statistical analysis by Hernandez group, Cornell University. Adapted from [42]

2.6 Conclusions

The findings reported in this study show that fatigue life in cancellous bone is sensitive to the transverse rod thickness, a structural component that has negligible effects on strength and stiffness. We extend the concept to synthetic microlattice structures where we show that the fatigue life of such cellular foams is heavily influenced by the proportion of material oriented transverse to the loading direction. We show that this effect is not limited to bending dominated structures, but is also effective for stretching dominated lattices. Further, we identify empirical modifications to traditional stress vs life (S-N) curves with the addition of $1/\sqrt{\psi}$ where ψ refers to the proportion of material oriented transverse to the loading direction. These findings then allow the designer to balance stiffness and strength needs in microarchitectured materials with durability and allow for the design of more efficient cellular foams and microlattice structures. In this chapter, we identified a key structural parameter in bone, the transverse rods that affect fatigue life, implemented a

mechanical framework to understand the response and we employed computational techniques to extend the behavior to engineering structures and synthetic lattices. While the focus of this chapter was on fatigue resilience, in the next chapter we investigate a more dynamic loading scenario, by exploring vibrational characteristics of mosquito antennae.

3. MECHANICAL AND NEUROPHYSIOLOGICAL MECHANISMS IN MOSQUITO ANTENNAE PROMOTE THE DETECTION OF ACOUSTIC TARGETS AMIDST NOISE

Parts of chapter 3 will be included in the publication – A. A. Trikanad, H. Pantoja, X. Bernal, P. Zavattieri, "Mechanical and neurophysiological mechanisms in mosquito antennae promote the detection of acoustic targets amidst noise", Status – In preparation.

3.1 Introduction

In the last chapter, we investigated fatigue resilience in cancellous bone. From a cyclic loading study, we now focus on a more dynamic loading context by investigating the acoustic organs in mosquitos to glean useful mechanical insights. The ability to detect sound has evolved independently, multiple times in animals over millennia to allow them to distinguish sources in many different directions and to effectively exploit biologically relevant acoustic sources[46]. Sound sensory organs vary widely between animals from the tympanic ears of vertebrates to the particle velocity detectors of insects. Elegant and efficient solutions have evolved to confront the challenge of hearing in insects to overcome physical constraints imposed by their small size which complicates acoustic detection due to the smaller surface area available to harness the propagating sound wave[47], [48]. Flying insects such as mosquitos also face an additional challenge posed by their beating wings which produce a tone. Consequently, mosquitos have to account for a noise source consisting of their own wingbeats at close proximity to their hearing organs. Despite these dual challenges, evolutionary adaptations have resulted in sensitive and specialized ears that allow then to accurately detect, localize and respond to conspecifics in demanding acoustic conditions such as a swarm of thousands of individuals[26].

Mosquitos use their antennae as acoustic receivers which, in contrast to tympanic ears, respond to velocity vectors in an impinging sound field rather than pressure variations[49]. In *Aedes aegypti*, males localize and follow females in swarms by listening to their wingbeats[26]. Females respond to the flight tones of males and couples engage in acoustic courtship behavior. In other mosquito species however, audition is critical in other ecological contexts. In *Uranotaenia lowii*, mating is not mediated by acoustic signals but females depend on audition to detect, localize and attack frogs by hearing their call and ultimately feeding on their blood[50]. The disparate auditory challenges associated with hearing frog calls for foraging and mates for reproduction are

expected to have resulted in different hearing organs that effectively respond to those stimuli. Understanding the ability of mosquitos to accurately detect these distinct acoustic cues despite their own noisy wingbeats could introduce new understanding into acoustic systems.

The mosquito antennal system consists of two functional components, the segmented flagellum (or antennal shaft) and the sensory organ located at the base of the antenna, called the Johnston's Organ (JO) (Figure 3.1) [49]. Acoustic stimuli are detected as flagellar sound-induced vibrations which travel down the flagellum to the base of the antenna entering the JO where they are transduced by mechanosensory cells to electrical signals to be parsed out at the brain. Antenna performance is thus governed by both biomechanical and neurophysiological mechanisms. Studies so far, however, have mainly focused on the neurophysiological component of mosquito audition[51]–[56] while less attention has been given to the biomechanical component[26], [28], [29]. Considering that the neural component is similar across species[29], biomechanics are expected to play a critical role in determining interspecific differences in sensitivity and tuning across mosquitos. Here, we study the structural and functional features of the mosquito antennal hearing system. Specifically, we characterize the morphological and mechanical features of the antenna of two species that detect acoustic cues in different behavioral contexts. We determine the effect of individual structural parameters that shape the vibrational response, and we evaluate how the mechanical design of the antenna modulates detection of acoustic cues associated with specific biological functions; hearing conspecifics and hearing frogs. Finally, we propose and validate a neurological model of mechano-electric transduction that occurs at the JO, and predict how the entire system can amplify target sounds despite the presence of their own noisy wingbeats.

3.2 Structural and Mechanical Characterization

The flagellum of the mosquito consists of segments of varying dimensions stacked one on top of the other. From each segment, long and thin sensory hairs (fibrillae) extend radially outward from the antenna. The sensory hairs along with the flagellum are deflected by an impinging sound field and the system behaves as a simple forced damped harmonic oscillator which is resonantly tuned to specific frequencies[26], [27]. While most research into mosquito auditory systems assumes that the antenna is a stiff rod whose primary purpose is to transmit vibrations to the JO, we contend that the structural variations as well as material properties in the antennae have a more significant effect on the vibrational response. Antennae of males and females of two species – *Aedes aegypti*

and *Uranotaenia lowii* - were examined under an X-ray microscope (Figure 3.1). *Aedes aegypti* males detect and orient towards a close moving target (female flight tones) during mating while females are able to detect approaching males. Male antennae are short (about 1300 μm) with an average diameter of about 20 μm, with a structure vaguely reminiscent of a Christmas tree. They are plumose (large number of sensory hair) with approximately 40 sensory hairs per segment with hair lengths ranging from 270 to 740 μm. *Aedes aegypti* females have longer antennae (about 2000 μm with an average diameter of about 23 μm. They are non-plumose antennae with about 6 hairs per segment ranging in length from 150 to 430 μm[57]. *Uranotaenia lowii* males are not known to use sound for any purpose, while females detect and orient towards a distant static target (frog calls) for blood meals. Males and females are structurally similar with both containing non-plumose antennae of comparable lengths (approximately 1414 μm for males and 1480 μm in females) with average diameters of 15 μm for both. They contain about 6 sensory hairs per segment with lengths ranging from 115 to 260 μm for males and 105 to 260 μm for females (Figure 3.2B). Our collaborating group then assessed the vibrational response for these antennae using Laser Doppler Vibrometry (LDV). Antennae were subjected to pure tone stimuli in a frequency range from 100 to 10000 Hz. Magnitude and phase of the particle velocity in the sound field as well as magnitude and phase of the velocity response of the antenna were measured at the free end of the antennae as well as along the midpoint. The magnitude and phase of vibration velocity of the antenna was normalized by the magnitude and phase observed for the particle velocity of the ambient air (Figure 3.2C).

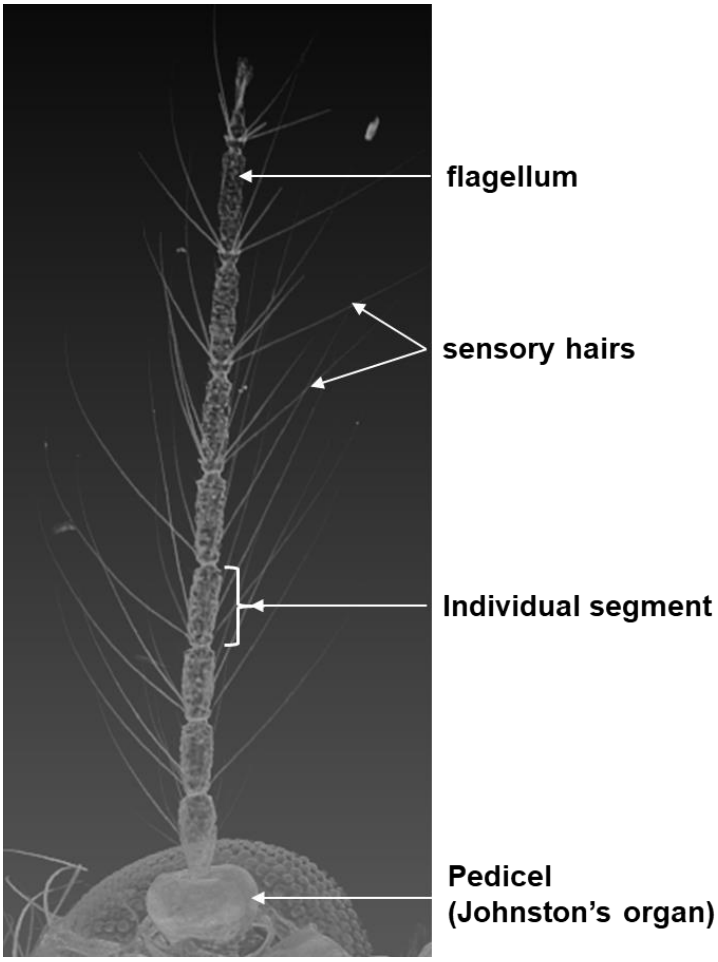

Figure 3.1: CT scan of the antenna of *Aedes aegypti* female mosquito highlighting individual structural and functional components of the antennal hearing system.

Response curves for the *Aedes aegypti* antennae were recreated from data procured from Gopfert et al[26]. They reported that the male *Aedes aegypti* antenna shows the highest sensitivity at 383 ± 28 Hz whereas the female antenna shows peak response at 229 ± 17 Hz. At these frequencies, amplitude peaks are observed to be greater than 1, indicating amplification of the signal. The phase response shows that antennal vibration leads the particle velocity at low frequencies by about 90 degrees, followed by a phase shift at the regions around the best response. The phase shift (of approximately 180 degrees) concurrent with the peak in the amplitude indicates the presence of the first resonance mode for each model. Further phase shifts at higher frequencies also indicate the presence of higher order resonance modes. At resonance, the *Aedes aegypti* male has a maximum antennal velocity (v_f/v_air) of 3.0±0.3 while the female shows a lower amplification of 2.1±0.3. The *Uranoteania lowii* mosquitos show similar structural features

between the two sexes, but this is not reflected in their vibrational response to pure tone stimuli. The male antenna shows best response at 518±16 Hz while the female antenna has a peak response at 305±25 Hz. The phase shift seen in the response indicates the presence of resonance concurrent with the amplitude peaks for the male and female antennae. The amplification of the signal (v_f/v_air) observed for the *Uranotaenia lowii* male at the best frequency is 1.275 while the female shows a larger amplification of 1.72.

Overall, a comparison of all the antennae shows that there are design variations present between species as well as between sexes with differences in the structure, antennal segments and sensory hairs which is reflected in the variations observed in their response to pure tone stimuli. Comparing between sexes, the plumose antenna of the *A. aegypti* male shows a higher amplification at resonance than the *A. aegypti* female. Interestingly, the *U. lowii* female antenna shows a higher amplification than the male, even though there is not much variation of the sensory hairs between the two antennae. Comparing between species, the *A. aegypti* male antenna presents the largest amplification across all antennae studied and the female *A. aegypti* antenna shows a higher amplification than the *U. lowii* female. These LDV experiments then provide a baseline to calibrate computational models that can provide deeper insight into the workings of the antennal system.

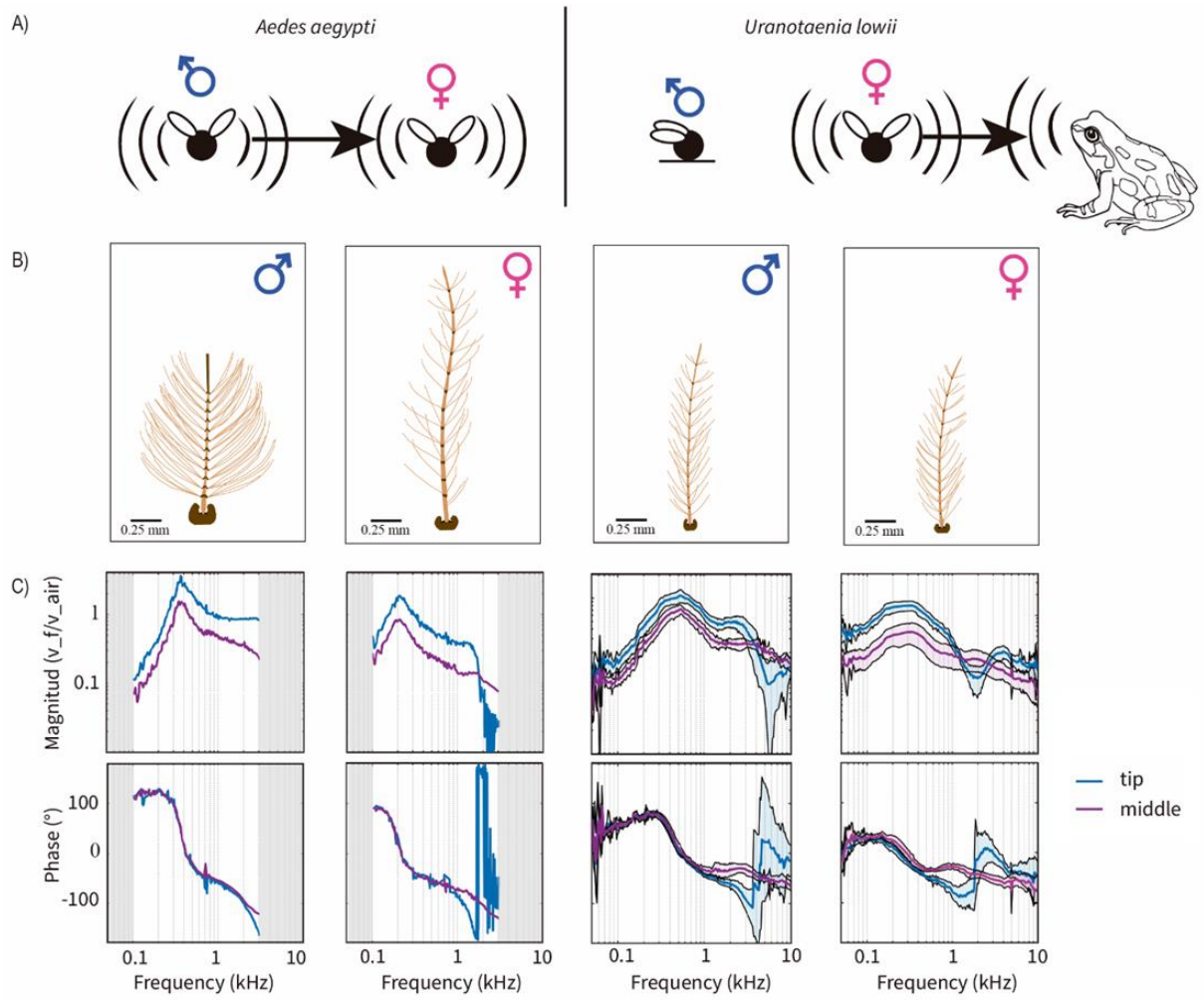

Figure 3.2: Sex and species-specific variation in response to pure tone sound for mosquito antennae. (A) Acoustic cues for two different species of mosquitos. (B) Scaled representations of antenna for males and females of each species. (C) Magnitude and phase of response to pure tone stimuli for vibrations measured at the tip (blue) and middle (violet) for each antenna via LDV. Experiment performed by H. Pantoja, Bernal Group, Purdue University.

3.3 Development of Computational Models

To evaluate the effect of the individual structural features on the vibrational response, finite element modeling (FEM) was performed for each antenna when subject to pure tone stimuli.

3.3.1 CAD Modeling

For each of the four mosquitos, dimensions of individual antennae including hair lengths and distributions, segment sizes and the JO were used to design geometrically accurate CAD models using the Abaqus CAE pre-processor (Figure 3.3). Three types of models were built for each antenna; models with a flagellum of uniform diameter (base model), models with flagellum including the intersegmental variation, and finally models with flagellum with segments and hair lengths and distributions. We hope to determine the effect of each structural parameter through a comparative analysis between these different models.

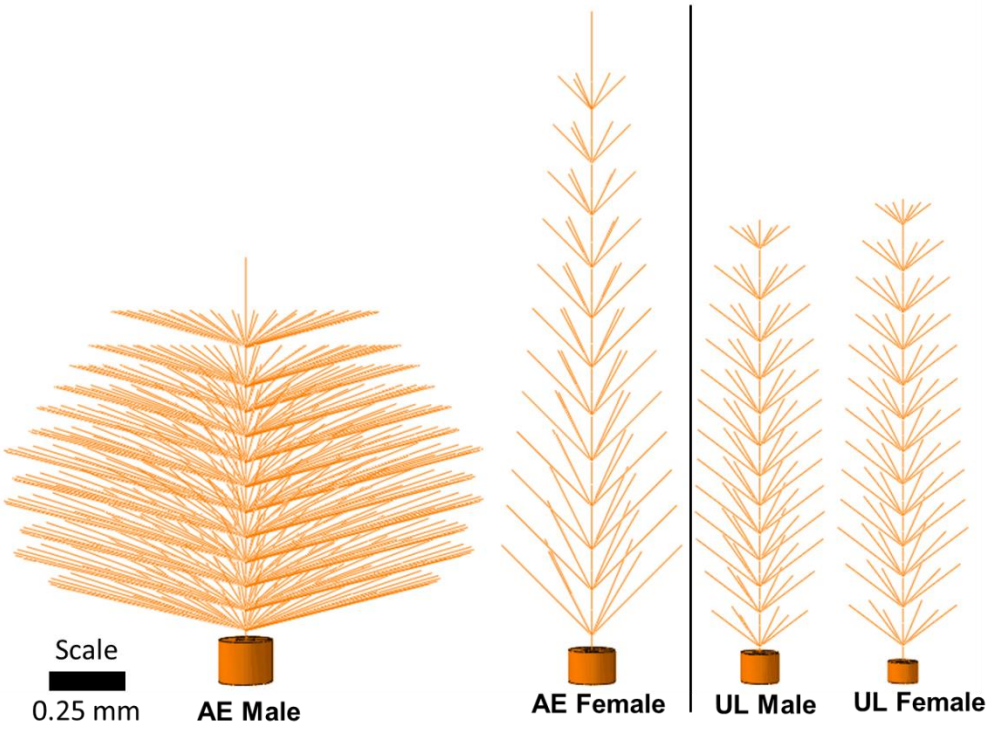

Figure 3.3: CAD models were developed for male and female of both species of mosquitos studied.

3.3.2 Boundary Conditions

First, a free vibration analysis was performed to determine the natural frequencies and associated mode shapes for each model. Then, forced vibration response was analyzed in the steady state to evaluate the response of each antenna when subject to harmonic inputs. Models were fixed at the bottom of the JO and pressure was applied directly to the antennal surface (Figure 3.4). Since the Reynold's number of the system is very small (<<1), the major driving forces are considered to be

friction and damping, which are represented in the model, but as acting directly on the surface of the antenna. This simple approximation allows us to avoid a computationally expensive fluid-structure interaction model since the focus of this work is on the effect of the individual structural parameters.

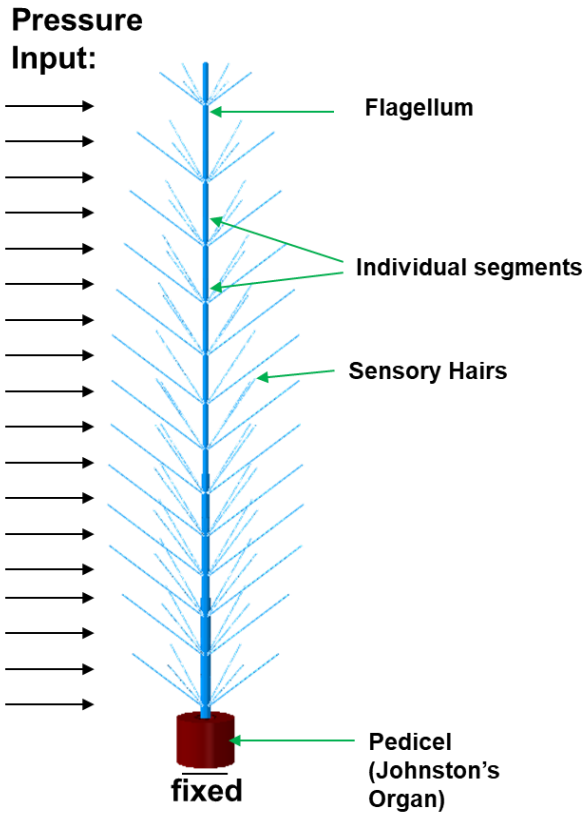

Figure 3.4: Boundary conditions for the antennal models.

3.3.3 Addition of hair and segments

The addition of the sensory hairs led to a significant increase in mass of the *A. aegypti* male antenna (48%) while the increased mass for the other antenna models was not as large (6%). The addition of segments converted a beam with a constant cross-section to one with a varying cross-section. The change in width per unit length was calculated as a function of segment number to show that the antennae have a tapering cross section due to a combination of decreased diameter of segment and increased length of segment with increasing segment numbers (Figure 3.5).

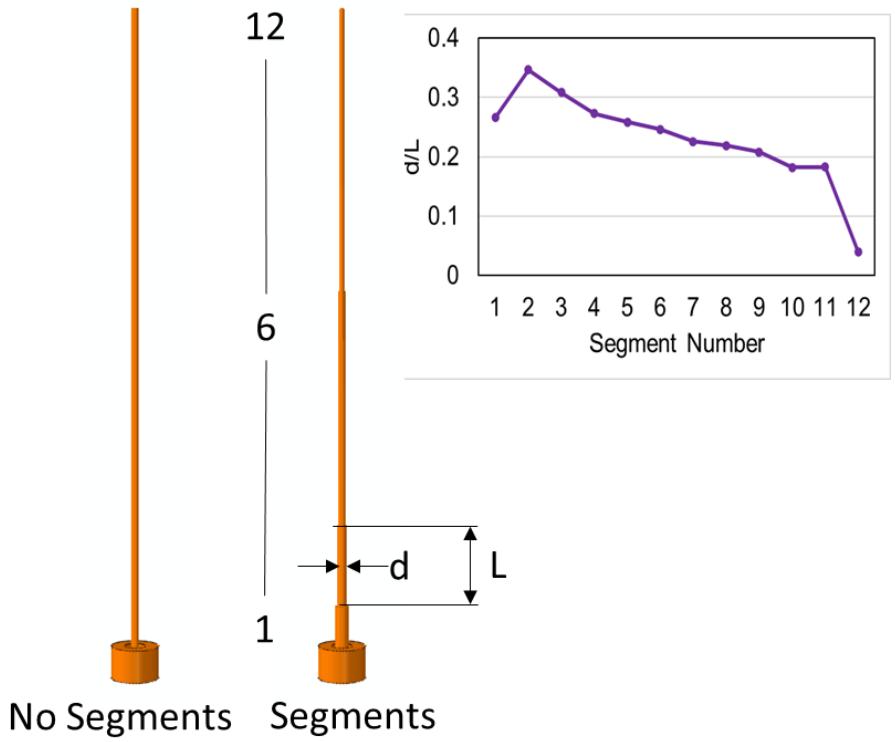

Figure 3.5: Quantification of variation in segment dimensions with segment number for one of the four antennae – the *A. aegypti* female.

3.3.4 Material Properties

To the best of our knowledge, there is no publication that has comprehensively characterized the mechanical properties for the different materials in the antennal system. Therefore, the following approach was adopted. The flagellum consists of an external shell of hard cuticle with an internal core of soft tissue. Material properties for the cuticle were obtained from previously published work[58]. Since the cuticle has been relatively well studied, material properties for the other components of the models including the soft tissue, the JO cuticle and tissue, and the sensory hairs were assigned using ratios of stiffness variation from the cuticle as observed by Saltin et al using confocal laser microscopy[28]. A parametric analysis for each of the materials was performed to evaluate the effect of material on vibrational response (Figure 3.6). It was found that any large changes in vibrational properties for the system was only significantly affected by the mechanical properties of the insect cuticle which has been characterized in literature[58]. Finally, a rule of mixture approach was used to derive a composite stiffness for the flagellum to ensure computational efficiency.

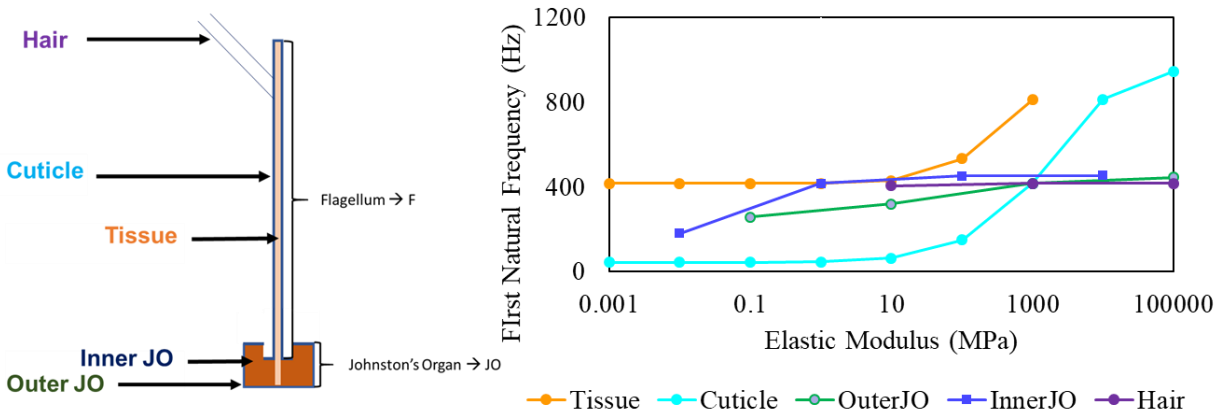

Figure 3.6: Parametric analysis of effect of varying mechanical properties on vibrational response of the antenna. 400 Hz is the expected natural frequency for this model. Variations in elastic modulus of the cuticle show the largest difference in the overall vibrational response.

3.4 Quantification of effect of individual structural features

Figure 3.7A shows all the models with the different variations that were tested. Free vibration analysis showed that the first mode of natural frequencies consisting of a rigid translation of the antenna with no inflection points showed an excellent match with the experimentally observed first resonance peaks. These models were then subjected to pure tone stimuli ranging from 100 to 3000 Hz. Velocities were extracted at points along the tip of the antennae to determine the effect of individual structural parameters on the steady state vibrational response (Figure 3.7B). All models showed an excellent fit with the experimental data with the first natural frequency modes matching those observed in the experiments (dashed line). In highlighting the effect of the structural parameters, most apparent, is the effect that the sensory hairs have on the sensitivity of these antennae. All models displayed a significant increase in sensitivity due to the presence of hair. The highly plumose male *A. aegypti* antenna, showed a remarkable 39.18 dB increased sensitivity as compared to the base model, with the female showing an 18.46 dB increased sensitivity. For the *U. lowii* antennae, the male showed a 20.89 dB increase in sensitivity with hair, while the female showed a 20.37 dB increased sensitivity when compared with the base model. Mechanically, the addition of sensory hairs causes an increase in mass and stiffness of the system, while at the same time, increasing the surface area available to capture the applied pressure. In general, an increase in mass for such a system is expected to drive down the vibration amplitude, and cause a negative shift in the tuning response resulting in a lowering of the resonant frequency.

In contrast, the increased stiffness as well as surface area can result in an increased sensitivity, with the increased stiffness also potentially increasing the resonant frequency. For the *A. aegypti* male model, we see an interplay between these competing mechanisms where the stiffness and surface area effects dominate the vibration amplitude response leading to a large increase in sensitivity while the tuning response seems dominated by the mass, resulting in a lower first natural frequency peak. The addition of hairs also results in a more familiar phase change for all models, with good agreement with those observed in the experiments (Figure 3.7C). The effect of the intersegmental variation was also quantified, with the addition of the segment geometry leading to a relatively smaller increase in sensitivity. While the vibrational response for the *A. aegypti* male seems dominated by the hairs, the effect of the segmental variation for the other three models on tuning is more significant, allowing for a shift in the natural frequency modes in the simulations that more closely align with those observed via experiments. Overall, these results indicate that the sensory hairs play a large role in increasing sensitivity of these antennae, while the intersegmental variation is integral in tuning the natural frequencies of these resonantly tuned antennal systems.

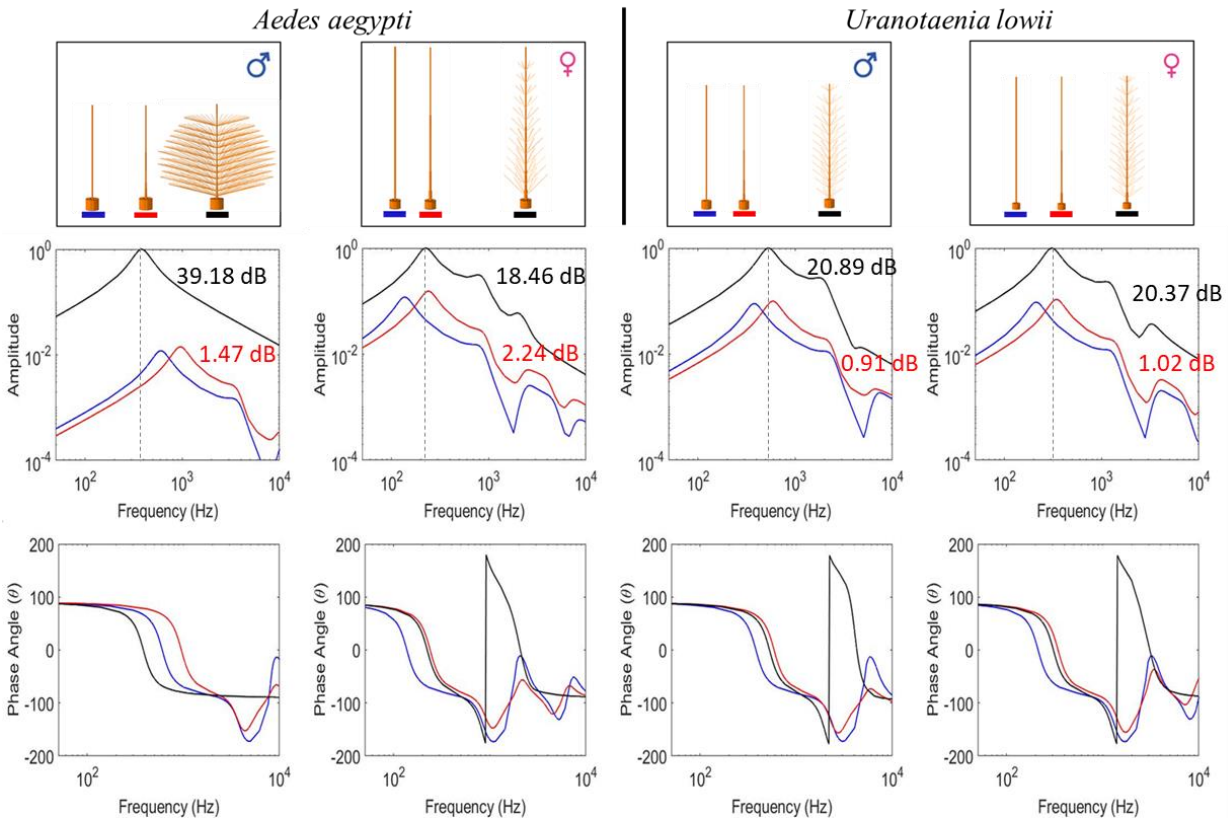

Figure 3.7: Effect of sensory hair and intersegmental variation on mechanical response of antennae to pure tones. (A) Three models for each antenna consisting of a base model with a rod of constant diameter (blue), a rod with varied diameters to mimic intersegmental variation (red) and a rod with segmental variation as well as sensory hairs (black). (B) Magnitude of velocity response to pure tone stimuli for all 3 variations for both sexes of both species extracted from the tip of the antenna. Dashed line indicates experimentally observed first natural frequency. (C) Phase response for all 3 variations for both sexes of both species extracted at the tip of the antenna.

3.5 Mechanical Vibration Response to Real World Stimuli

To ascertain the response of these hearing systems to real world stimuli, the antenna models were subject to specific inputs mimicking those they may observe in their natural environments. Since the *A. aegypti* mosquitos are known to follow conspecifics in a swarm by tracking wingbeats of the opposing sex, wing beats of the *A. aegypti* male and female mosquitos were recorded and provided as input to the models (Figure 3.8A). The *A. aegypti* antenna models were first subject to the wing beat tones of their opposing sex. Since the mosquitos also have their own wingbeats in close proximity which may act as a noise source, models were also subject to their own wingbeats in conjunction with the opposing wing beat signals. Velocities were extracted from the base of the

antenna, on the basal plate, to more accurately identify the information reaching the JO. Both models of the *A. aegypti* antennae showed an ability to highlight the opposing wingbeats with their highest amplitude peaks matching the wing beat frequency of the opposing sex. The *A. aegypti* male model accomplishes this due to the proximity of its first natural frequency mode to the wingbeat frequency of the female. For the female *A. aegypti* antenna, the models show that the antenna harnesses its second natural frequency mode, a mode associated with bending of the antennal flagellum to amplify the signal of the male wingbeats. Interestingly, when subject to the combination of their own wingbeats as well as the opposing wingbeats, the antenna in the *A. aegypti* female model was able to produce an amplification of the signal of the opposing wingbeat of about 43% (Figure 3.8B). In comparison, the *A. aegypti* male antenna was unable to show significant amplification of the signal when subject to a combination of its own wingbeats and those of the opposing sex (Figure 3.8C). These findings suggest that, while both sexes of the *A. aegypti* antennae are able to highlight the wingbeats of the opposing sex, the male antenna might already be well suited to amplify the signal of the wingbeats of the female due to the profusion of sensory hair, while the female antenna benefits from the "noise" produced from its own wingbeats to amplify the signal of the male wingbeats. Also noteworthy, is the proximity of the two peaks in the antennal responses when antennae are subject to wing tones of both sexes. These indicate the presence of a strong distortion product produced during the non-linear transduction process in the JO when the mechanical vibrations are converted to electrical signals. Previous studies indicate the ability of some mosquito species to harness the distortion products to amplify the target signal[52], [54], [59].

While the *A. aegypti* mosquitos are known to follow conspecifics in swarms, the females of the *U. lowii* mosquito species use audition for a different purpose; to localize frogs for blood meals by tracking their frog calls. To explore their ability to highlight frog calls, and compare and contrast against another species, the antennae of the *A. aegypti* female and the *U. lowii* female were subject to inputs gathered from the recording of male barking tree frogs (*Hyla gratiosa*) which are known to attract *U. lowii* females in their natural environment[50]. Inputs to each model also included their own wingbeats in conjunction with the frog calls to better mimic natural conditions (Figure 3.8D and Figure 3.8E). Velocities were extracted from the base of the antennae models, on the basal plate, to maintain accuracy with information that would reach the JO.

Comparatively, the *U. lowii* female model showed a higher sensitivity to the frog call frequencies than that observed by the *A. aegypti* female (Figure 3.8F). In addition, the *U. lowii* female antenna showed its highest sensitivity at the frog call frequency while in comparison, the *A. aegypti* female had its largest peak at the frequency of its own wingbeats. These indicate that the passive biomechanics of the *U. lowii* female antenna has been optimized to highlight the frog call signal even through the "noise" associated with its own wingbeats occurring in close proximity to its antenna.

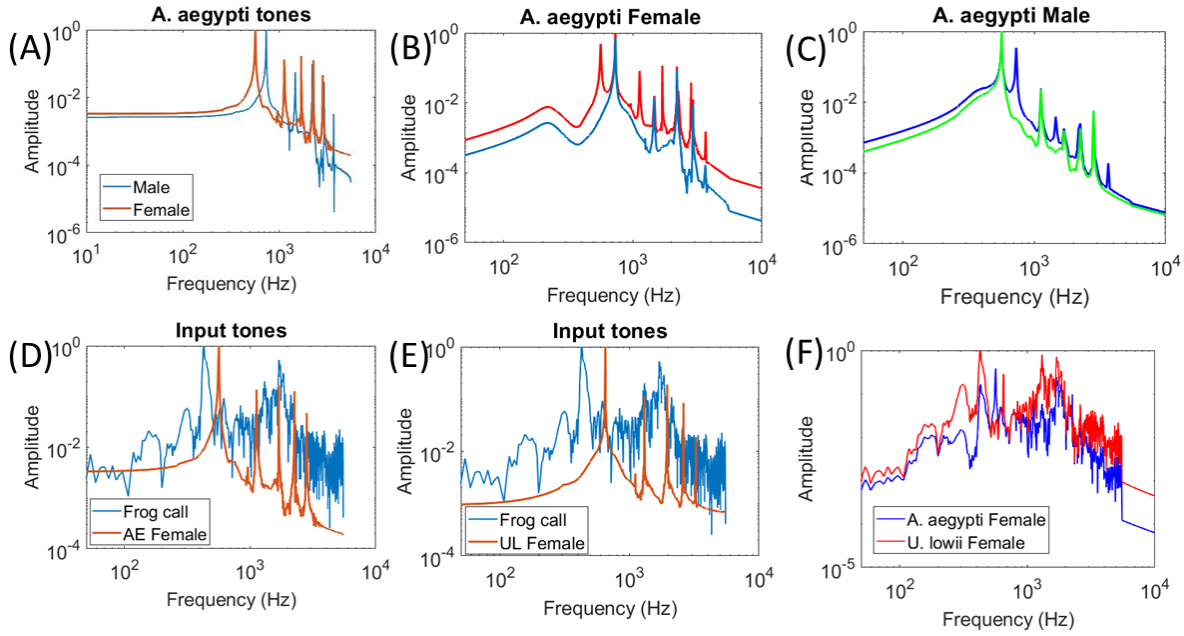

Figure 3.8: Response of antennae to real world stimuli. (A) Wing beat tones for the *A. aegypti* male and female mosquitos. (B) Response of the antenna of the female *A. aegypti* to the tone of the male wing beat (blue) and to the tone of combined male and female wingbeats (red). (C) Response of the *A. aegypti* male antenna to the female wingbeats (green) and to the combined male and female wingbeats (blue). (D) Combined input tones for frog calls and *A. aegypti* female wing beats. (E) Combined input tones for frog calls and *U. lowii* female wingbeats. (F) Response of *A. aegypti* (blue) and *U. lowii* (red) female antenna models to input tones from (D) and (E) respectively.

Overall, these results indicate the importance of the structural features and mechanisms in the antennal system to harness and amplify those specific acoustic targets associated with their biological function. While the antennal system is effective at harnessing the sound wave, the information is then transmitted via the basal plate at the base of the antenna to the JO which

performs the transduction of mechanical vibrations to electrical signals, and then through the antennal nerve to the brain where information is processed. The JO neural response has therefore been investigated in previous literature by inserting conductive electrodes in the antennal nerve, to record electrical activity being transmitted in response to sound. By performing electrophysiological recordings at the antennal nerve, it has been established that the JO works like a low-pass filter of frequencies below 1000 Hz and relies on a non-linear transduction process—non-linear relationship between flagellar displacement and electric current recorded at the antennal nerve. In addition, high precision experiments have revealed differences on the dominant frequency of intracellular and extracellular recordings. Such characteristics produce particular and trackable characteristics that our collaborators have used to develop and validate a model of transduction. Here, they employ simple electric circuits to qualitatively simulate the electric response of JO sensory units, and use neurophysiological recordings previously obtained by [52], [59], to validate our simulations.

3.6 Electrophysiological transduction of flagellar vibration

In the JO, aggregations of sensory units called scolopidia are responsible for transducing flagellar vibrations. These sensory units are formed by two or three cells working in anti-phase (Figure 3.9A). This model simulates each cell as an electrical circuit composed of a current source connected in parallel to a variable resistance and a capacitor. The resistance value is controlled by the displacement of the flagellar base plate, modeling the transduction occurring at the cell membrane with a non-linear transfer function between displacement and current (Figure 3.9A). In addition, low-pass filters simulate the limit rate at which membranes can transduce mechanical stimuli into electrical current. The response of a single circuit simulates intracellular recordings and the summation of electrical signals from two or more circuits working in anti-phase simulate extracellular recordings. The output of this model qualitatively matches the characteristics of electrophysiological signals obtained from intra and extra-cellular recordings (Figure 3.9B), using one or two-tone stimuli[59]. In response to one tone or an individual frequency, both the experimental data and the model output show that intra and extra-cellular responses exhibit harmonic distortion (Figure 3.9B), produced by the non-linear properties of transduction. The dominant frequency of the response, however, varies between intra and extra-cellular responses. While intracellular responses exhibit a dominant frequency equivalent to the stimulus frequency,

extracellular responses exhibit a dominant frequency that is double the frequency of the stimulus (Figure 3.9B). Frequency doubling in the model is produced by the antiphase response of individual circuits. In response to two-tone stimuli (f1 and f2, with f1<f2), nonlinear transduction produces extracellular responses that exhibit intermodulation distortion. In particular, intermodulation amplifies the frequency difference between the two-tone stimuli (f2 – f1) (Figure 3.9C).

By using this electrical model developed by our collaborators, we evaluated the sensory response of an interaction between two tones corresponding to the mosquito's own flight tone fundamental frequency and an acoustic target. To simulate how non-linear properties of transduction affect detection, we compared the electrical response obtained from our model, using a linear transduction function, $y(x) = x$, a higher order polynomial series ($y(x) = 1 + x + x^2 + x^3 + \cdots + x^{12}$) and an exponential function ($y(x) = e^x$) where the resistance value ($y(x)$) depends on the displacement (x) of the basal plate. By gradually reducing the amplitude of the acoustic target, we evaluated the level of attenuation in the response. Also, we determined the if the intermodulation produced at the sensory unit of the JO helps to amplify the target signal. Results were obtained in reference to the amplitude of the tone that simulates the mosquito's own flight tone. First, we found that non-linear transduction reduces attenuation (Figure 3.9D). While a higher-order polynomial series reduces attenuation by 4.64$\pm$0.64 dB, the exponential function was able to reduce attenuation by 0.63 $\pm$0.53 dB. Secondly, the electrical model shows that intermodulation can amplify the frequency difference between two tones (f2-f1) depending on the transfer function. While the higher order polynomial series generates an amplified intermodulation product, experimentally recorded in [54], the exponential function does not produce any amplification. The advantage of intermodulation is that, while amplified, low frequency products also carry information about the acoustic targets. When the target has similar amplitude to the mosquito flight tone, intermodulation distortion produces an amplification of 1.32 dB in reference to the mosquito's own flight tone (Figure 3.9D). Further, when the target amplitude is reduced, the intermodulation product is attenuated at a lower extent compared to the target with an attenuation of 11.67$\pm$9.74 dB for the intermodulation product versus an attenuation of 16.26$\pm$0.64 dB for the acoustic target. Together, these results support the hypothesis that non-linear transduction processes provide mosquitos with several advantages in terms of detection of acoustic targets.

Figure 3.9: Electrophysiological transduction model simulating the mechanisms at the JO. (A) Denotes the different sensory units in the JO, with descriptions of intra and extracellular recordings. Also depicts the non-linear transfer function between current and displacement. (B) Intra (yellow) and extracellular (blue) recordings comparing model with experimental data. Also depicts harmonic distortion in both intra and extracellular recordings. (C) Intermodulation distortion amplifies the difference between the input tones (f2-f1). (D) Comparison of electrical response and attenuation between target signal and intermodulation product for different linear and non-linear transduction functions. Model by H. Pantoja, Bernal Group, Purdue University.

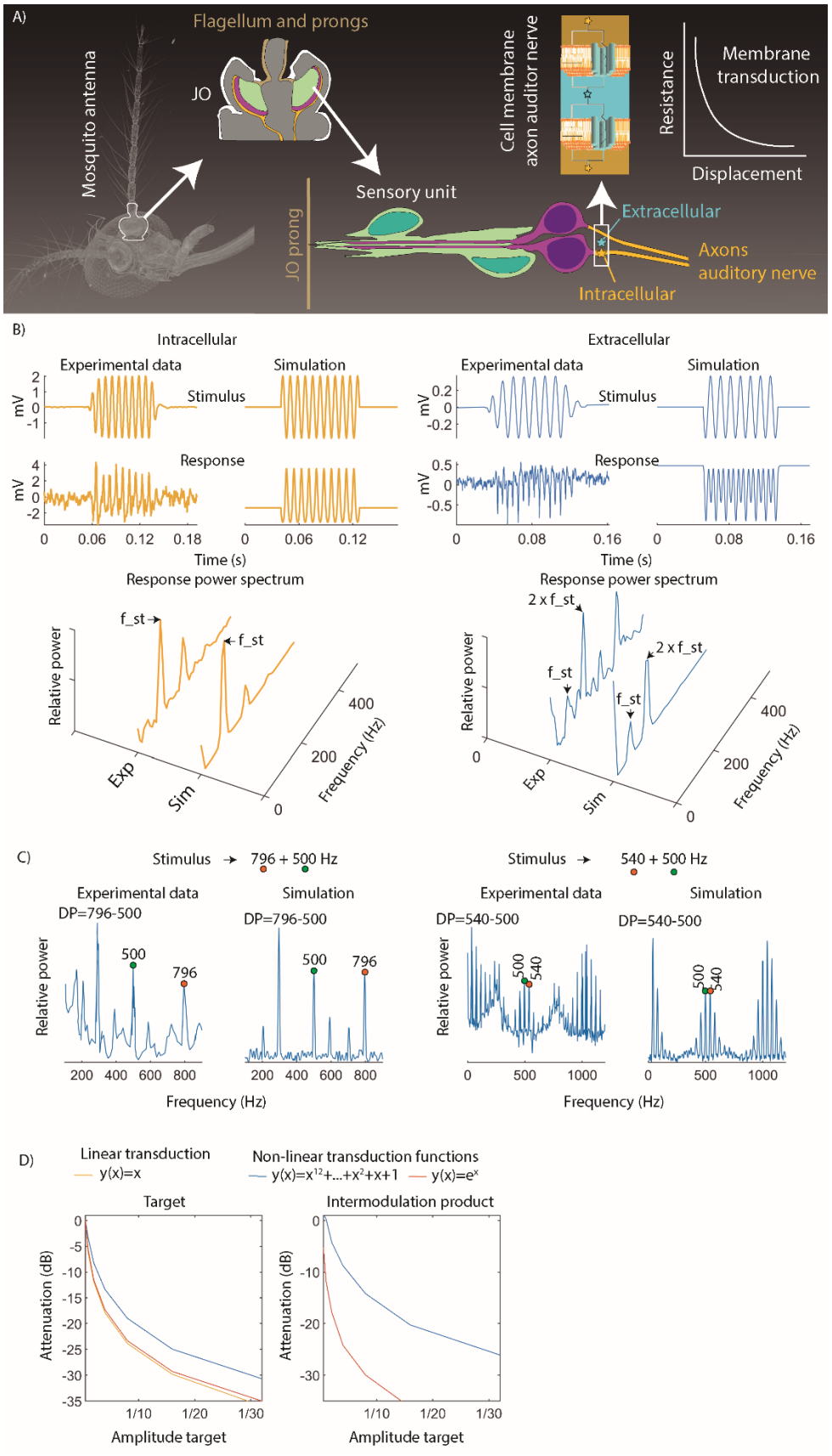
A)
Flagellum and prongs
JO
Mosquito antenna
Sensory unit
JO prong
Cell membrane
axon auditor nerve
Resistance
Membrane
transduction
Displacement
Extracellular
Axons
auditory nerve
Intracellular
B)
Intracellular
Experimental data
Simulation
Stimulus
Response
mV
Time (s)
Extracellular
Response power spectrum
Relative power
f_st
2 x f_st
Exp
Sim
Frequency (Hz)
C)
Stimulus → 796 + 500 Hz
Stimulus → 540 + 500 Hz
DP=796-500
DP=540-500
Frequency (Hz)
D)
Linear transduction
y(x)=x
Non-linear transduction functions
y(x)=x¹²+...+x²+x+1
y(x)=e^x
Target
Intermodulation product
Attenuation (dB)
Amplitude target
1/10
1/20
1/30

3.7 Conclusions

Our studies show that mosquito antennae are small, sensitive and specialized acoustic systems. Finite element modeling of the individual structural features highlights opposing mechanisms at play that allow sensory hairs to increase sensitivity of these systems and intersegmental variation to affect the tuning of the natural frequencies. FE modeling also showed that these antennal systems are able to amplify specific acoustic signals. In *A. aegypti*, male antennae show the highest response at the fundamental frequency of the female wingbeats and female antennae show the highest sensitivity at the fundamental frequency of male wingbeats. With the addition of their own wing tones as noise, these models were able to show an even larger amplification, indicating that these antennal systems can use the noise produced from their own wing beats to amplify the acoustic target signal. In response to frog calls, FE models showed that the *U. lowii* female mosquito is able to highlight the frog call frequency above the frequency of its own wingbeats, while in comparison, the *A. aegypti* female cannot highlight the frequency of the frog call, but instead, shows highest sensitivity at its own wingbeat frequency. When the acoustic target and the noise consisting of their own wingbeats are fed into these models, we see that the vibrational response shows two sensitivity peaks in close proximity. Our electrophysiological model shows that due to a non-linear transduction process between current and displacement of the basal plate, the proximity of the two peaks produces intermodulation distortion products. The mosquitos are able to harness the distortion products to amplify the signal at a lower, more accessible frequency. Also, the distortion product is attenuated at a lower extent compared to the acoustic target. Taken together, these results indicate that mosquitos in fact use noise or competing signals (their own wing beats) to both mechanically and electrophysiologically amplify and capture the target acoustic signal. While in general, noise is considered detrimental, these studies of mosquito audition point to non-intuitive and unexpected mechanisms in mosquitos which allow them to utilize noise to amplify signals. These mechanisms draw parallels with superheterodyne receivers[60], employed in virtually all modern day radios, which use distortion products of radio frequencies to pick up radio channels at specific frequencies. These results indicate a uniquely engaging method of acoustic communication with numerous potential applications in sensing technologies[61], with arrays of such antennal systems that can be integrated into wearable technology. Another potential application for these systems is in MEMS (Micro electrical mechanical system) microphones which have gained increasing popularity due to their small size,

high sensitivity and relatively low power consumption. They are integrated into hand-held devices, mobile phones, wearable electronics and Internet of Things (IoT) devices. Newer generations of hearing aids also feature MEMS microphones. While MEMS microphones are known for their high signal to noise (SNR) ratios, performance in noisy environments can still pose a challenge. Using the mechanisms unveiled in this study can provide insight and ideas to inspire a new generation of noise-resistant microphones.

This study primarily dealt with understanding mechanisms of mosquito antennae using steady state vibrational analysis. We evaluated structural adaptations in mosquito antennae including their sensory hairs and their intersegmental variation, and their effect on overall vibrational response. We defined mechanical and neurophysiological mechanisms present in these antennae that allow them use competing signals to amplify their acoustic targets. We also proposed their adaptation into different applications including mechanical sensors and noise resistant microphones. In the next chapter, we continue with the theme of mechanical vibrations by taking a look at vibrational characteristics in the woodpecker heads and their ability to prevent brain damage during pecking.

4. MECHANICAL AND FUNCTIONAL EVALUATION OF WOODPECKER SKULL BONES

Parts of chapter 4 are included in the publication – J. Y. Jung, A Pissarenko, A. A. Trikanad, D. Restrepo, F. Y. Su, A. Marquez, D. Gonzalez, S. E. Naleway, P. Zavattieri, J. McKittrick, "A Natural Stress Deflector on the Head? Mechanical and Functional Evaluation of the Woodpecker Skull Bones", Advanced Theory and Simulations, vol 2, no 4, p.1800152 (2019)[62]

4.1 Introduction

Concussion is a form of mild traumatic brain injury (mTBI) caused by external mechanical forces to the head. It occurs commonly in contact sports such as football or hockey or from direct trauma as a result of vehicular accidents[63]. Repeated concussions can lead to chronic traumatic encephalopathy, a progressive degenerative disorder resulting in symptoms of depression, memory loss, and suicidal behavior[64]. Woodpeckers, on the other hand, are known to peck at trees throughout their natural at pecking rates of 20-25 Hz while suffering no overt signs of brain damage[30]. May et al[65] originally recorded the drilling action of woodpeckers with a high speed camera and found that the head moves in a straight trajectory and reaches maximum speeds of 7 m/s with a deceleration of up to 1500 g within a 0.5 – 1 ms impacting duration. In terms of evolutionary design modifications, Burt and Bock[35] pointed out that some woodpeckers that hammer more frequently than others present an anatomical adaptation on their skull bone, called the frontal overhang. This was the first report of a structural specialization on the skull bone hypothesized to aid in impact mitigation. Gibson[66] described an allometry effect between woodpecker and human heads in terms of concussion limits and concluded that the scaling effect enables woodpeckers to avoid brain injury due to the smaller size, shorter duration of impact, and large contact area between the brain and skull bone but did not consider the interspecies variations in mass within woodpeckers in her study.

In terms of mechanical or biomechanical analysis of woodpecker pecking, there have been quite a few studies that focus on various aspects of the woodpecker mechanics. Yoon et al[34] focused on the spongy bone; a bone surrounding the brain as a shock absorbing mechanism and created a simplified mass-spring-damper model to represent the vibrational characteristics through impact. Using this simplified model, they were able to develop a bioinspired shock absorbing system to protect micromachined devices with very low failure rates of about 1% at 60,000g while

commercially available hard-resin methods displayed a failure rate closer to 26%. Another group of researchers, extracted a more accurate model from CT scans of a dead woodpecker and provided one of the earlier more detailed analyses of the woodpecker head. They assigned material properties to every part of the complete woodpecker head, including the brain and rain a finite element analysis against a simulated piece of wood[67]. They showed that the stress wave starts from the upper beak and then propagates into the lower beak and nostrils. They postulated that the hyoid bone absorbs most of the energy during impact and protects the brain in the skull. In a following paper that addresses three successive pecking events, through the use of numerical simulations, they claimed that 99.7% of the impact energy through pecking is converted into strain energy in the bulk of the body of the woodpecker and only 0.3% is converted into strain energy in the head which is then dissipated. They however do mention that they were unable to get a stable convergent resolution because of the large number of elements and significant differences between element sizes.

Another body of research focused on a biomechanical investigation of the woodpecker head[30]. They produced a FE model through micro-CT scans of a woodpecker head. Their investigation showed that the lower beak would be the first point of contact during impact. BY performing a parametric analysis for various lengths of the upper and lower beak, they were able to show that having an equal length for both beaks induced the highest strains on the woodpecker head. They postulate that there is a distinct advantage in having beaks of different lengths. They claim that the sophisticated shock absorption system of the woodpecker is a good cooperative phenomenon with not any single factor being able to achieve the function. Liu et al[32] studied the relationship between the woodpecker's head during impact and the hyoid bone. The hyoid bone is a bone that starts on the right nostril, moves through the top of the woodpecker skull, loops round the skull and goes into the mouth to become the tongue. They used micro-CT scanned images and employed the Material Point Method (MPM) to simulate the woodpecker's pecking process. The hyoid bone shows a variation of strength along its length. They performed analyses for woodpecker heads with and without hyoid bone, to assess the effect of the hyoid bone. Their results showed that the woodpecker head without the hyoid showed higher stresses as compared to the head with the hyoid. On models where they also add muscle, they show that the combination of muscle (modelled as simplified elastic material) and hyoid bone enhance rigidity of the

woodpecker head and thus suppress the deformation and oscillation of the endoskeleton after impact.

While there is a significant body of research on the workings of the woodpecker head under impact, there is still no clear quantification of the contribution of the separate constituent parts on impact mitigation and energy dissipation. Because of the complexity of the structures in the head, and the varying materials, compositions and interfaces, understanding the effects in a composite model can be difficult and computationally expensive. In this work, we first build a complete composite model of the woodpecker head for a more qualitative understanding of the mechanics during pecking, and then move to a simplified model with single material, structure and composition to evaluate the effect of the different skull bones. In the previous chapter, we primarily used steady state vibrational analysis to analyze mechanical response in mosquitos. In this chapter, we first investigate steady state response in woodpecker heads, and then investigate stress wave propagation during impact.

4.2 Biological Observation

A morphological comparative analysis between species of woodpeckers was performed by our collaborators. It shows that the frontal overhang, as observed by Bock[35] is an evolutionary adaptation among some species of woodpeckers that is directly correlated with their pecking habits. Figure 4.1A highlights the different parts of a woodpecker skull while figure 4.1B describes the biological observation of the frontal overhang being more prevalent in woodpeckers that are associated with pecking more often. This work then focuses on the mechanical and functional evaluation of the woodpecker skull bones with emphasis on the effect of the frontal overhang.

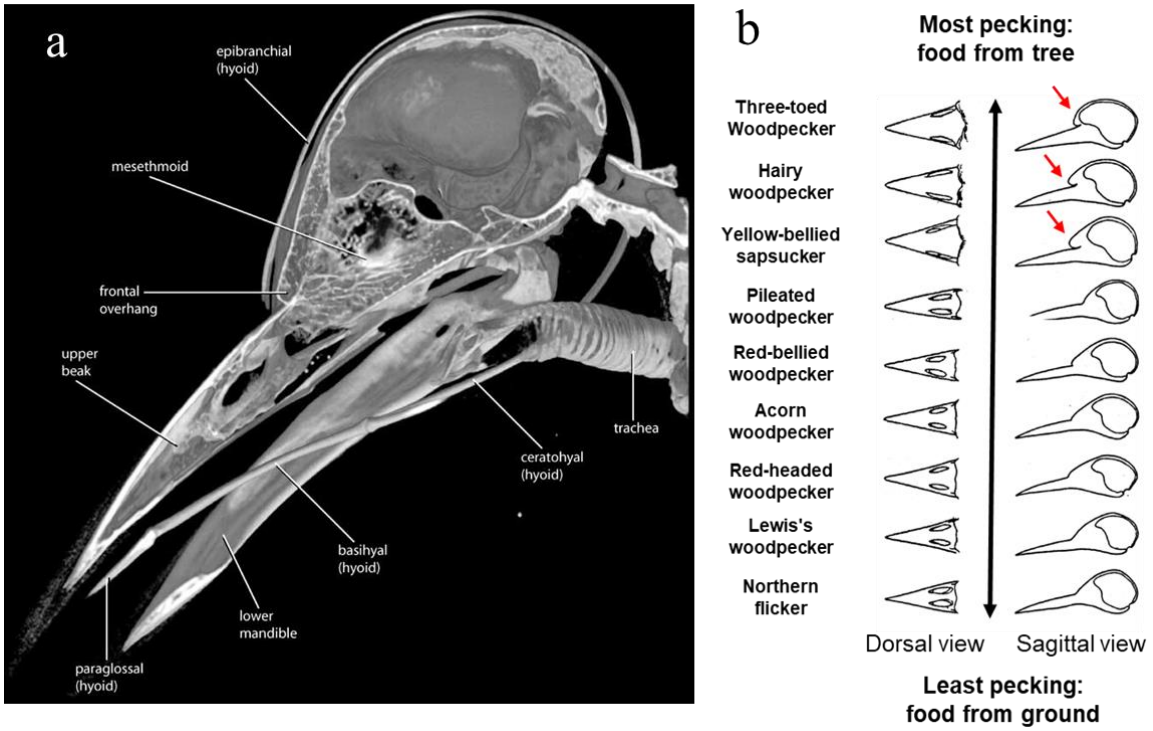

Figure 4.1: A) Different skull bones of the woodpecker head. Adapted from *digimorph.org*. B) Different species of woodpecker showing different anatomical adaptations on the skull bone based on pecking habits. Analysis performed by JY Jung, McKittrick group, UCSD. Adapted from [62]

4.3 Development of Computational Model

To quantify the effect of the skull bones and highlight comparisons between different parts, especially between the overhang and non-overhang species of woodpecker, a comprehensive 3D computational model was constructed with all the constituent parts to perform a general analysis of stress wave propagation and determine parameters that may be contributing to energy dissipation. Then, a simplified model of the woodpecker head was constructed. Two variations were considered from the original model, where frontal overhangs of smaller and larger size were added to quantify the effect of frontal overhang on impact mitigation.

4.3.1 CAD Model of 3D Composite Woodpecker Head

The woodpecker head is a complex structure with multiple constituent parts. 3D models of one species of woodpecker, the Golden Fronted Woodpecker (*Melanerpes aurifrons*) were generated

from micro-CT scans. Individual parts were generated from CT scans which then had to be converted to CAD models. Each part consisted of an initial 3D triangulated surface shell (.stl file) converted from CT scans using Amira. First, internal features were removed in Meshlab (an open source reverse engineering software), and holes that resulted from cleaning were filled to create a final clean surface. The surface was then imported into Geomagic (another reverse engineering software) where the files were converted to NURBS (non-uniform rational basis spline) surfaces which were then converted into 3D solid CAD models. Figure 4.2 represents the cleaning process for one of the parts.

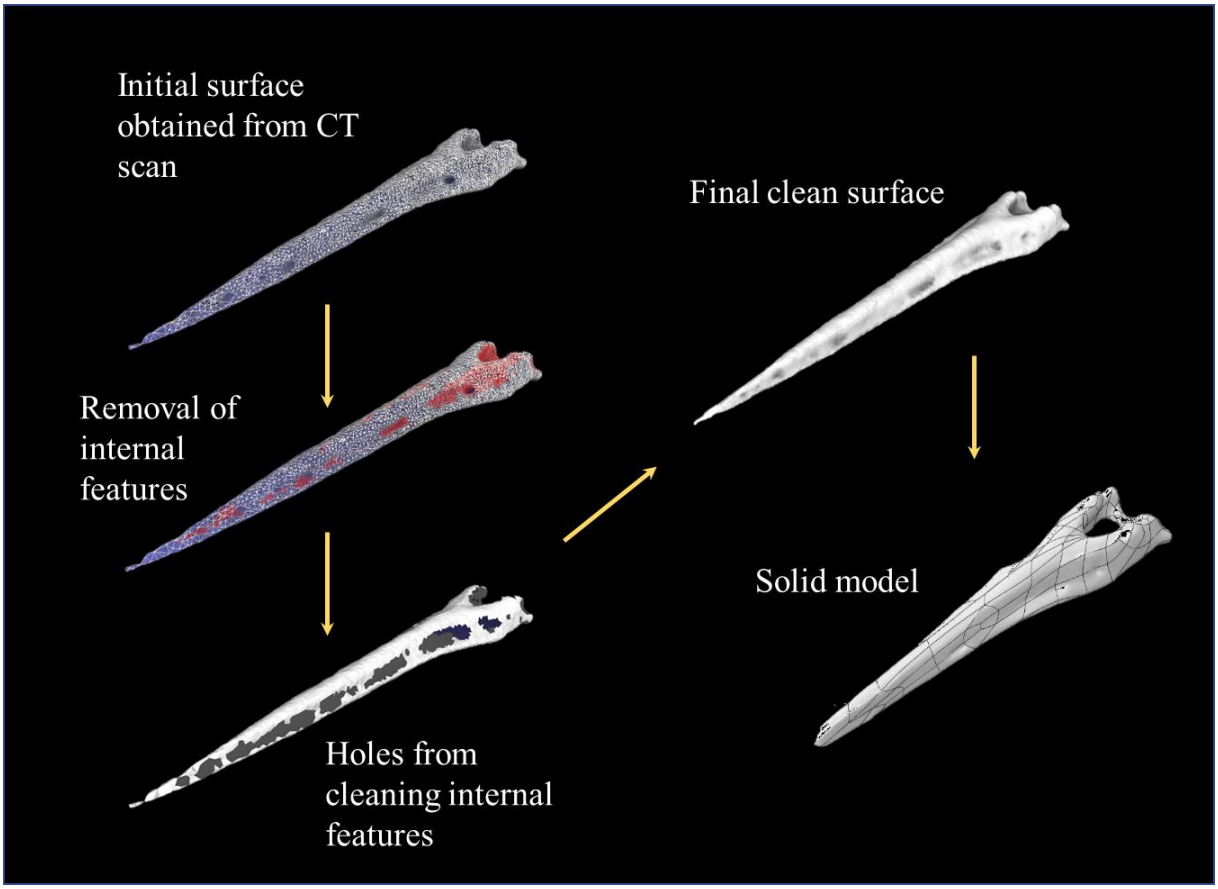

Figure 4.2: Reconstruction from μCT data to create CAD models. This example shows the reconstruction of the paraglossal bone, which is a constituent part of the hyoid bone in the woodpecker head.

The process was repeated for each of the bones in the woodpecker head, and then all the CAD parts were combined together into a single model in Abaqus. Figure 4.3 details the composite 3D model that was created after all the parts were assembled and connected.

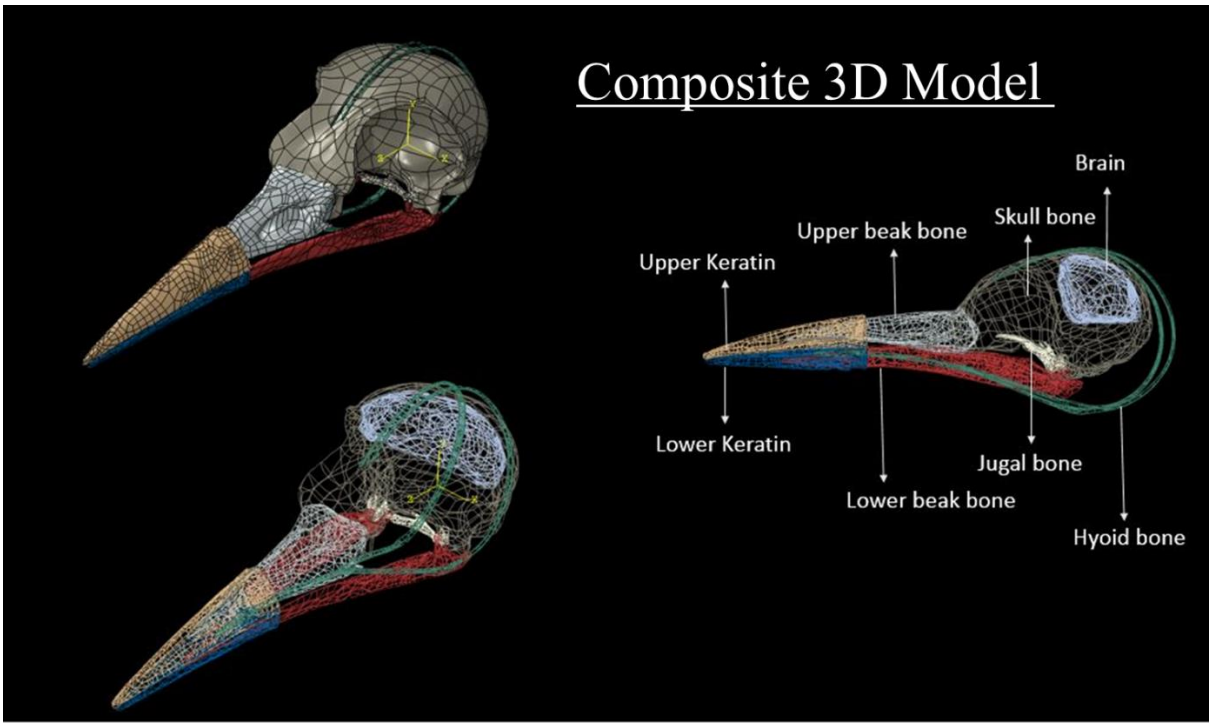

Figure 4.3: Composite 3D model of the woodpecker head including all the constituent parts.

4.3.2 Design of Simplified CAD Geometries

From the composite model, a simplified model was constructed that consisted of the skull bone, upper beak bone and jugal bone. From this model, two other models of the woodpecker skull with different overhang sizes were generated from the original scan. The artificial overhang models were built by adding material to the area that bridges the upper beak bone and the skull bone using sculpting tools in Geomagic with the original geometry of the Golden-fronted woodpecker as a reference. By using the same skull as a reference, we are able to rule out other parameters that might affect the dynamic behavior of the woodpecker under impact and focus only on the effect of the overhang during pecking. The three models are labelled model 1, model 2 and model 3 corresponding to the original skull, small overhang added, and large overhang added respectively. The models are shown in Figure 4.4.

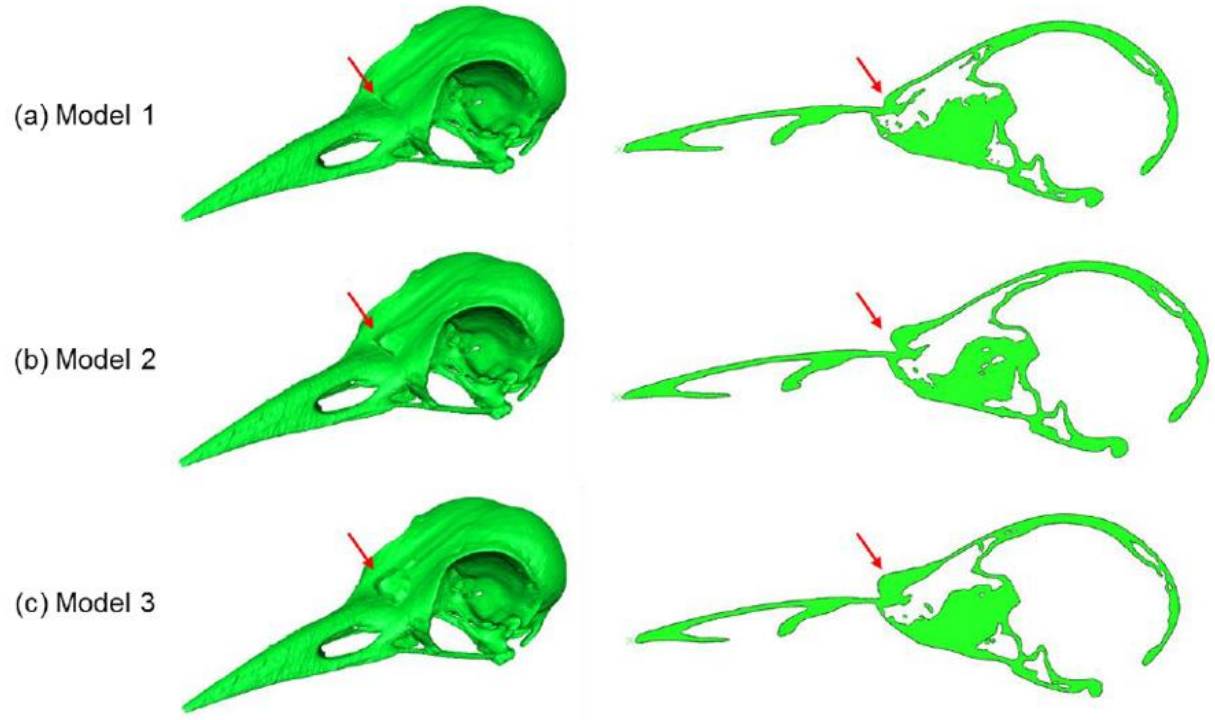

Figure 4.4: Three models of the skull bone for dynamic finite element analysis. (A) Model 1: Original reconstruction of the skull of the Golden Fronted Woodpecker. (B) Model 2: Model with small artificial overhang. (C) Model with large artificial overhang. The images on the right side are the view-cut sectional along the sagittal plane.

4.3.3 Finite Element Modeling of 3D Composite CAD Model

Individual parts of the woodpecker head were stitched together to create the composite 3D model in Abaqus. Material properties for the individual parts were derived from literature[32], [34], [68], [69]. Keratin was modeled with a density of 1320 kg/m^3 while the skull bone, beak bone and hyoid bone were assigned a density of 1456 kg/m^3. Elastic moduli assigned were 8.7 GPa for keratin, 11 GPa for the skull bone, 30.2 GPa for the beak bones, and 17 GPa for the hyoid bone. Poisson's ratios were 0.4 for keratin, and 0.3 for the skull bone, beak bones and the hyoid bone. The composite head model was meshed in Abaqus with a mesh consisting 1.5 million C3D4 linear tetrahedral elements. Impact simulations were conducted in Abaqus/Explicit against an analytical rigid plate to analyze the stress wave propagation in the composite model and determine important stress pathways to better understand the woodpecker head, and to inform the simplified 3D models.

4.3.4 Finite Element Modeling of Simplified Models

The simplified models of the woodpecker head consisting of the skull bone, upper beak bone and the jugal bone were meshed in Abaqus with approximately 650,000 C3D4 linear tetrahedral elements. The material for each of the models was considered to be linear elastic and isotropic with Young's modulus of 15 GPa, poisson's ratio of 0.33 and a density of 1456 kg/m^3. The material selection was taken through as a combination of materials for the skull bone and the upper beak bone referenced in the previous section. The addition of the artificial overhangs resulted in an increase of 62.65 mm^3 in the volume and of 0.092g of the mass in the case of Model 2, and of 65.29 mm^3 and 0.095g for volume and mass respectively in the case of Model 3. Previous research has shown that there is a negligible effect of the biological fluids and soft tissue in the pores of the bone on the modulus of the bone[69]. Consequently, in this study, we neglect the effects of tissue fluids. We considered two types of simulation methods to evaluate the effects of the frontal overhang during pecking.

Frequency Modal Analysis

We performed frequency modal analysis of the three models to evaluate the effects of the added mass and volume on the natural frequencies of the woodpecker's skull due to the frontal overhang. To this end, we fixed the models at the point where the skull meets the neck and calculated the first 5 modes of natural frequency for the three models. Figure 4.5A shows two of the three models used with different sizes of frontal overhang, and figure 4.5B shows four representative nodes that were identified as points of interest, where vibration data was extracted. Two of these nodes are along the dorsal line (nodes 1 and 2) and two of them along the ventral line (nodes 3 and 4). Modal analysis allows us to characterize the frequency response of the woodpecker head under free vibration.

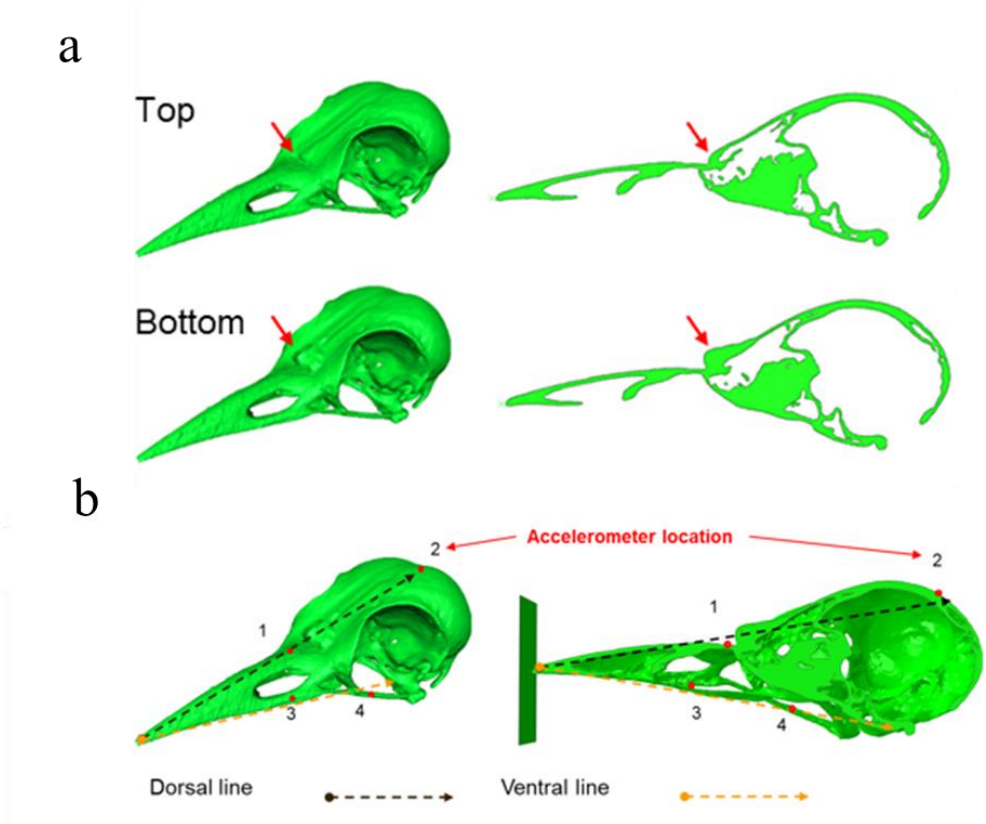

Figure 4.5: A) Two models of the skull bone with different frontal overhangs for dynamic finite element analyses. B) Node identification for regions of interest where 1: the caudal end of the upper beak bone, 2: on the parietal bone near the brain, 3: on the palatine bone and 4: on the jugal bone. Adapted from [62]

Ricker Pulse Analysis

Following the frequency modal analysis, time domain dynamic simulations using Abaqus/Explicit were performed to evaluate the effect of stress wave interaction and vibrational response of the three models during impact loading. The loading was applied to the tip of the beak as shown in figure 4.6A while keeping the same fixed end as in the modal analysis. A Ricker wavelet was used to represent the shape of the impact pulse. Ricker wavelets are widely used in the seismic and vibration fields because they can be uniquely specified with only a single parameter that corresponds to its peak frequency as seen on the wavelet's frequency spectrum (figure 4.6C)[70], [71]. In the time domain, the wavelet is represented by a central peak with two smaller side lobes

(figure 4.6B). The amplitude $A(t)$ of a Ricker wavelet with peak frequency f_M at time t is given by:

$$A(t) = (1 - 2\pi^2 f_M^2 t^2) e^{-\pi^2 f_M^2 t^2}$$

In the case of this study, the Ricker wavelet shape of the impact allowed us to obtain from the simulations a clean response with an expected bandwidth contrary to the case of a direct impact input at a given velocity (7 m/s) as shown in figure 4.6D. The amplitude of the Ricker pulse was scaled to 0.01 N for the models and centered on a peak frequency of 4970 Hz which is in the general region of the first mode of natural vibration for each model with the expectation that the vibrations in the model would be dominated by their first mode of natural frequency. Simulations were run for about 4000 μs and nodal accelerations were recorded at the points of interest previously specified in figure 4.5B. A fast Fourier transform (FFT) was used to convert the time domain acceleration information obtained at each point into the frequency domain. This allows us to discern the dominant frequencies present at those points and gives us an idea of the impact of frontal overhang in filtering these frequencies.

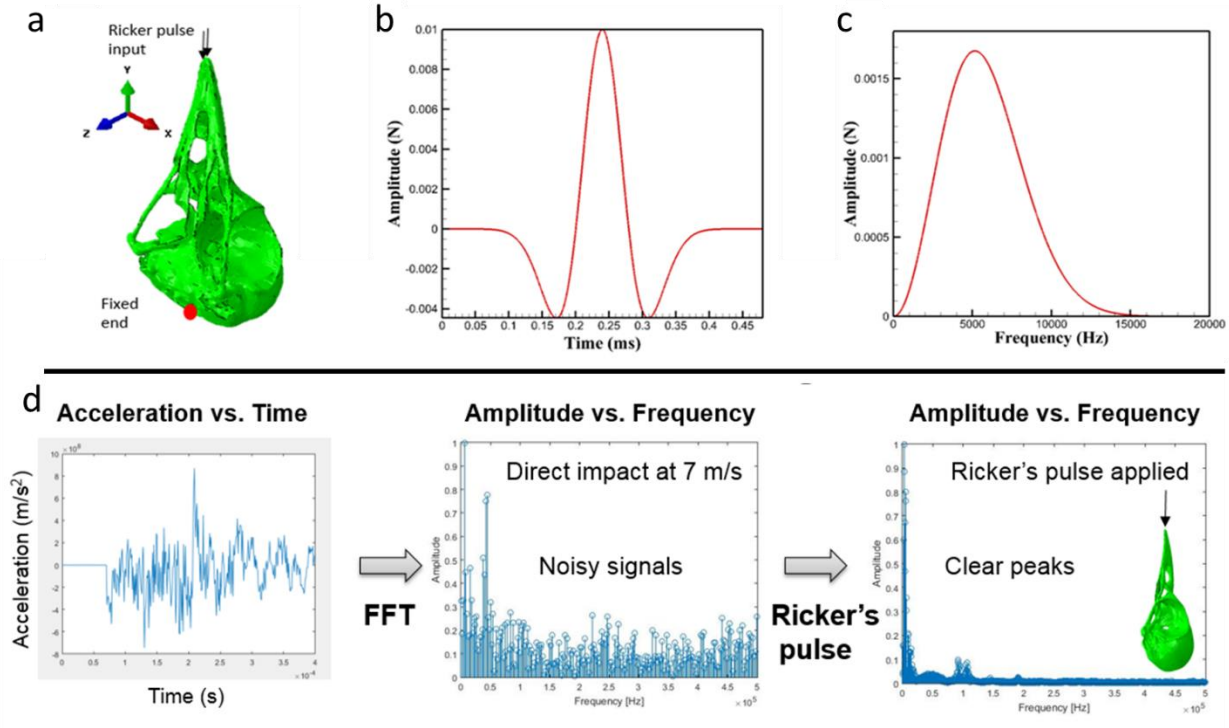

Figure 4.6: (A) Schematic illustration of the Ricker pulse input and the fixed end location considered for the ricker pulse analysis. (B) Time domain and (C) frequency domain characteristics of the ricker pulse.(D) Example of clear response using ricker pulse vs noisy data in a direct impact simulation.

4.4 Results and Discussion

4.4.1 Stress Wave Propagation in the 3D Composite Model

Dynamic impact simulations against an analytical rigid plate at 7 m/s impact velocity was performed with the 3D composite model including all the constituent parts to determine in a general sense, the stress pathway through the woodpecker head. VonMises stress was extracted at five points along the woodpecker head (Figure 4.7). Points of interest included the keratin sheath, the frontal overhang area, the jugal bone, the skull bone, and the hyoid bone represented as a, b, c, d and e respectively in figure 4.7. Stress wave propagation analysis showed that the stress was highest at the jugal bone (point c) indicating that perhaps the jugal bone is an important structural element in the stress pathway during impact. While at the same time, stresses on the back of the skull bone and the hyoid bone were very low indicating that perhaps the stress wave is redirected away from the brain during impact. While further analysis is necessary, this was done using the

simplified models of the woodpecker head. Due to the complexity of the structural elements, interfaces and contact conditions in the composite model, running simulations proved to be difficult and computationally expensive.

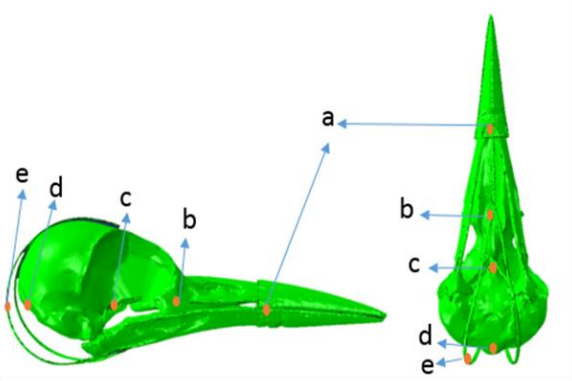

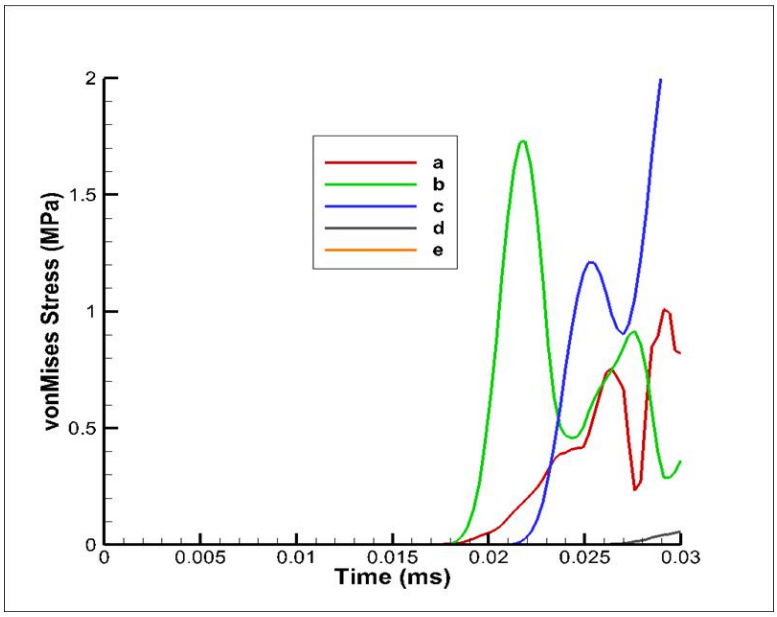

Figure 4.7: VonMises stress along different points along the composite woodpecker head model where ‘a’ is on the keratin sheath, ‘b’ is at the frontal overhang, ‘c’ is on the jugal bone, ‘d’ is on the skull bone and ‘e’ is on the hyoid bone.

4.4.2 Frequency Modal Analysis of simplified model

Previous work has shown that repeated low frequency impacts can result in head trauma for humans[72]. The authors reported that low frequency resonance between the brain and skull occurred in humans at ~20 Hz. Resonance can be dangerous because it amplifies the amplitude of movement in the brain and skull potentially causing brain damage. Therefore, it is advantageous

to have a frequency mismatch between brain and skull to prevent resonance during impact. Modal analysis of the woodpecker skull model described the first five modes of natural frequency. Modes 1 (4790 Hz), 2 (7026 Hz) and 3 (7458 Hz) corresponded to up and down bending motion of the skull bone in the three global axes. Modes 4 (8146 Hz) and 5 (10024 Hz) corresponded to twisted torsional motion between the palatine and jugal bones with relatively low movement of the skull (Figure 4.8A). To the best of our knowledge, there is no comprehensive material characterization of woodpecker brains in literature, therefore a direct comparison of the resonant frequencies of brain and skull are not possible. However, given that brain is a soft tissue with viscoelastic properties, resonant frequencies are expected to stay low (<4000 Hz) to avoid synchronized resonance with the skull bone.

4.4.3 Ricker Pulse Analysis of simplified model

Ricker pulse analysis allowed us to see the dominant frequencies at play during a dynamic event. Since the ricker wavelet has a characteristic frequency matching mode 1 (4970 Hz) of the model, one can expect that frequency to be dominant. FFT of acceleration data at the four points of interest showed that for points 1 (upper beak bone), 3 (palatine bone) and 4 (jugal bone) the dominant frequency matched that of the input frequency (4970 Hz). However, for node 2, situated near the brain, the dominant frequency was found to be around 7790 Hz which is a close match to mode 4 (8146 Hz) of natural vibration (Figure 4.8B). This is interesting because mode 4 is a mode associated with twisted torsional movement of the beak bones with relatively less movement of the skull bone and consequently, the skull-brain region experiences lower relative movement and therefore, potentially lower instances of damage. Using frequency mismatch is common practice in structural engineering, and the woodpecker is a good example of frequency control achieved only through modification of structural or geometric parameters.

4.4.4 Stress Wave Propagation in the simplified model

Further analysis of the stress pathway during impact was performed by collaborators[62] and is shown in figure 4.8C and figure 4.8D. Von Mises stress analysis showed that the stress wave-front after impact at the beak tip propagated through the ventral line of the head, primarily through the jugal bone to the neck and rest of the body. The stress level near the brain remained at a

significantly lower level than the rest of the skull bone. This shows good agreement with the stress wave pathways in the 3D composite model as well as with the results of the vibrational analysis indicating an isolation of the brain region from the path of the stress wave.

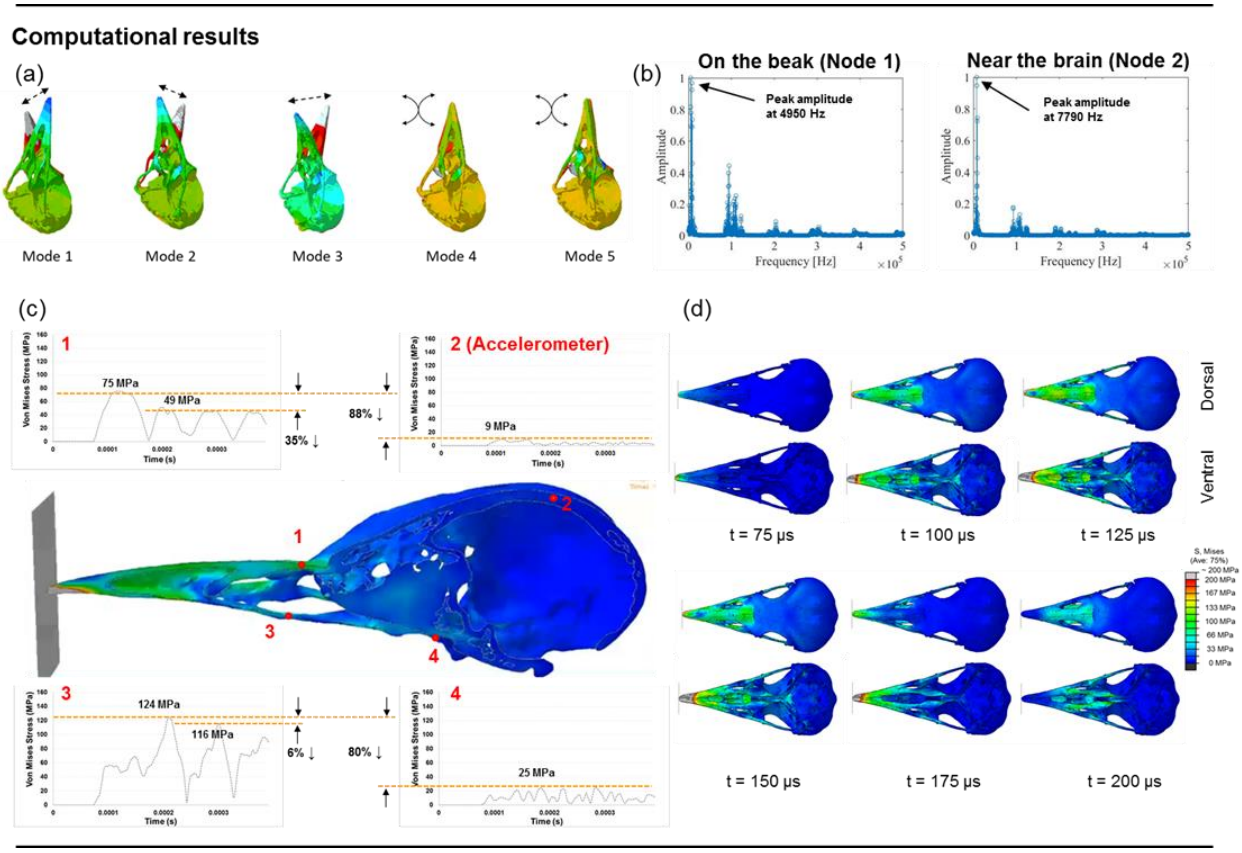

Figure 4.8: Computational results of impact testing. A) Five natural frequencies of the woodpecker skull. B) A representative result of Ricker pulse analysis at nodes 1 and 2. C) Plots of von Mises stress at four nodes. D) Time-lapse of von Mises stress distribution on the skull bone models at impact speeds of 7 m/s. Parts C and D performed by A. Pissarenko, UCSD. Adapted from [62]

4.4.5 Effect of Frontal Overhang

While biological observations seemed to indicate that the frontal overhang might play a role in frequency filtration or damage mitigation during impact, our simulations could not find a discernable effect of the frontal overhang in the modal or ricker pulse analysis. The first five natural frequency modes of the models with the frontal overhang were found to be very similar with variations within 15-20 Hz for all modes. This is likely due to the slight increased mass of

the system rather than a geometric property. Ricker pulse analysis comparing models with and without overhang showed small differences in dominant frequencies and all models showed the same trend of frequency isolation in regions around the brain (Figure 4.9).

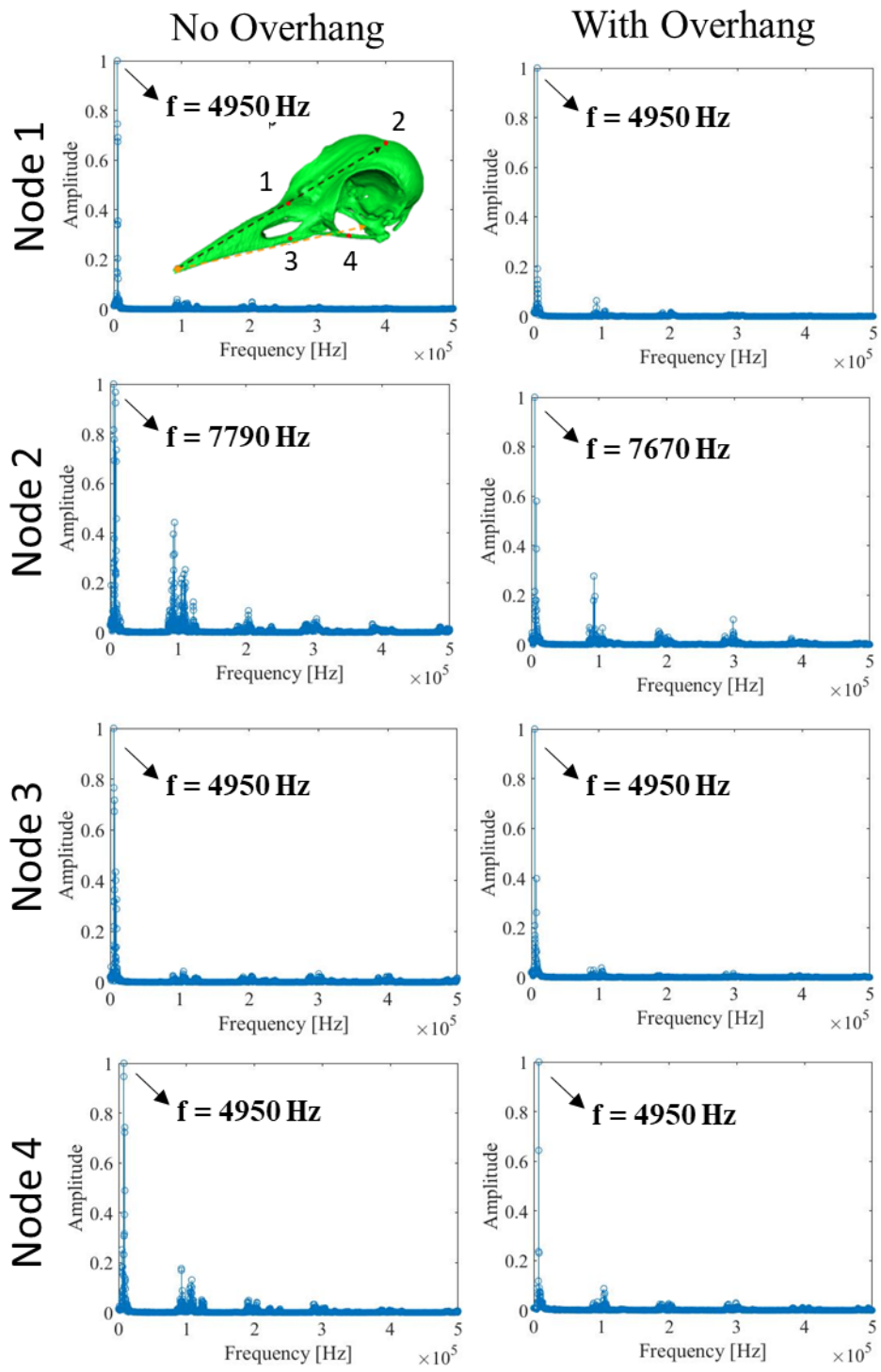

Figure 4.9: : Effect of frontal overhang. Comparison of dominant frequencies at the four regions of interest (inset in first plot) between woodpecker models with and without overhang show no major differences while maintaining the same frequency isolation characteristics around the brain (node 2).

4.4.6 Experimental Corroboration

Further experimental analysis was also performed by collaborators[62] with a drop tower impact testing setup using 3D printed skull models fitted with accelerometers. Vibrational data from the experimental setup showed a good match with computational results. Failure analysis of the 3D printed skull showed that significant damage at the beak tip and the jugal bones was observed during the dynamic test further supporting the hypothesis that the protection of the brain occurs by redirection of stress pathway through the jugal bone and a frequency mismatch between the brain and skull to avoid resonance. Further details on experimental work can be found in the referenced literature.

4.5 Conclusions

A combination of several structural features in the woodpecker head contribute to shock absorption and damage mitigation when they are pecking at trees. We developed a 3D composite model to assess stress wave propagation during impact. The model showed largest stresses at the jugal bone with stress around the brain and skull area remaining low. Further analysis with simplified models indicated that during impact, there is a redirection of the main stress pathway through the jugal bone and into the neck and body of the woodpecker. Natural frequency analysis hinted at large resonant frequencies in the skull bone which could help prevent resonance between the brain and the skull. Ricker pulse analysis showed frequency isolation of the skull bone and brain with the dominant frequency mode consisting of a torsional mode with relatively lower movement of the skull-brain area. Analysis of the frontal overhang was not able to discern any noticeable effect of this structural feature in energy dissipation or impact mitigation. Overall, these results indicate an ability of woodpeckers to use frequency mismatches and redirection of stress pathways using primarily structural features. Such design strategies can be applied towards protective head gear in contact sports.

In this chapter, we used novel methodologies including a ricker pulse analysis to identify structural adaptations in the head that allow the brain to be isolated from the stress wave during impact. We identified the effect of skull geometries in redirecting the stress wave away from the brain through the jugal bone and proposed applications towards protective head gear. The next chapter continues the theme of impact resistance, through the analysis of a different biological

structure that exhibits impact resistance and damage mitigation, the mantis shrimp where we use similar techniques, but with more focus on the transient analysis and the stress propagation.

5. MECHANICAL AND FUNCTIONAL EVALUATION OF THE STOMATOPOD TELSON: A BIOLOGICAL SHIELD

Parts of chapter 5 are included in the publication – N. A. Yaraghi, A. A. Trikanad, D. Restrepo, W. Huang, J. Rivera, S. Herrera, M. Zhernenkov, D. Y. Parkinson, R. L. Caldwell, P. D. Zavattieri, D. Kisailus, " The Stomatopod Telson: Convergent Evolution in the Development of a Biological Shield", Advanced Functional Materials, vol 1902238, p, 1902238, 2019 [38]

5.1 Introduction

In the previous chapter, we looked at woodpecker bones and their ability to protect against damage during pecking by redirecting the stress pathway. This chapter continues to investigate damage mitigation strategies in nature, by evaluating an organism that uses its skeleton in defensive situations. There are many natural organisms that depend on tough and stiff exoskeletons for protection against predators[6]. In organisms such as stomatopods (mantis shrimp), these structures also function as tools employed during ritualized fighting with conspecifics[41]. Mantis shrimp are well known for their powerful hunting strategies in which they employ a set of highly developed raptorial appendages known as dactyl clubs for hunting and attacking purposes[14]. Dactyl clubs are known to produce impacts with speeds of up to 23 m/s and forces up to 1500 N[73]. Two subgroups of mantis shrimp are the smashing and spearing varieties named for their attacking appendages. Smashing varieties of stomatopods use heavily mineralized club-like appendages (dactyl clubs) to deliver high energy impacts that smash shells of other crustaceans such as crabs. Conversely, spearers use thin dactyl structures with sharp spines to ambush, pierce and capture fish with soft bodies. Along with these attacking appendages, mantis shrimp have also developed a shield like terminal segment of their abdomen which they use as armor called the telson. The telson is commonly used for personal protection during ritualized fighting with conspecifics[39]. Smasher stomatopods perform an act known as coiling where they curl up their bodies and present the telson forward to absorb direct impacts from the dactyls of conspecifics during combat. Telsons can endure repeated high-energy impacts during ritualized fighting from the dactyl clubs without experiencing catastrophic failure. Previous observations made by Caldwell[74] suggest that the coiling behavior is limited to smashing type mantis shrimp. He also noted that the most burrow-limited species of smasher are not only the most aggressive, but also possess the most heavily armored telsons. Also, through micro-CT measurements, varying degrees

of mineralization and the presence of ridge-like geometries, called carinae, were identified in the smasher type telson which are hypothesized to impart a combination of stiffness and compliance in the structure necessary for energy dissipation[41]. During ritualized fighting, researchers observed via a statistical analysis that hits always occurred on the telson, and the winners of the bouts were the ones that displayed aggressive persistence or physiological endurance[39].

There have been relatively few biomechanical impact studies on the telson. Taylor and Patek compared multiple species of telson under impact by dropping steel balls on the telson and measuring the velocities pre and post impact[40], [41]. They found that co-efficient of restitution, a metric that determines elastic vs inelastic collisions, was on average 0.56 in the telson, indicating mostly inelastic behavior. On average, they calculated that 69% of the impact energy is dissipated. However, a more complete mechanistic description of the impact dynamics is still lacking. Moreover, the observation that more aggressive mantis shrimp have more well-developed ridges (carinae) in their telson is one that provides an avenue for exploration. Namely, why have the more aggressive species of mantis shrimp evolved ridges? To that end, this study first builds a comparison between the telsons of two species of mantis shrimp, a more aggressive smashing type (*Odontodactylus scyllarus*) and a less aggressive spearing type (*Lysiosquillina maculata*) stomatopod to compare the differences in the telson and the effect of ridges in providing stiffness or compliance. Then we focus on the mechanics of ridge-like geometries on the telson in impact mitigation, shock absorption and energy dissipation under high-energy impact conditions.

5.2 Morphological Features

Bulk specimens and their polished cross-sections were examined by our collaborators[38] to provide a general overview of the structural features of the smasher and spearer telsons. Figure 5.1A shows a representative view of the smasher stomatopod (*O. scyllarus*) and figure 5.1C shows the spearer stomatopod (*L. maculata*) with dashed regions indicating the telson. Figures 5.1B and 5.1D show the dactyl club for the smasher and the dactyl spear for the spearer telson respectively. Figure 5.1E and 5.1G show dorsal views of the smasher and spearer telsons respectively. Here noticeable differences become apparent. The smasher telson features many ridges, called carinae on its dorsal surface while the spearer telson lacks any such distinct geometry. Figures 5.1F and 5.1H then highlight the transverse cross-sections of the telson showcasing the distinct ridges in the smashing type telson as well as the pronounced central ridge called the medial carina. Other

differences such as a concave macrocurvature in the smasher telson and a convex macrocurvature visible in the spearer telson.

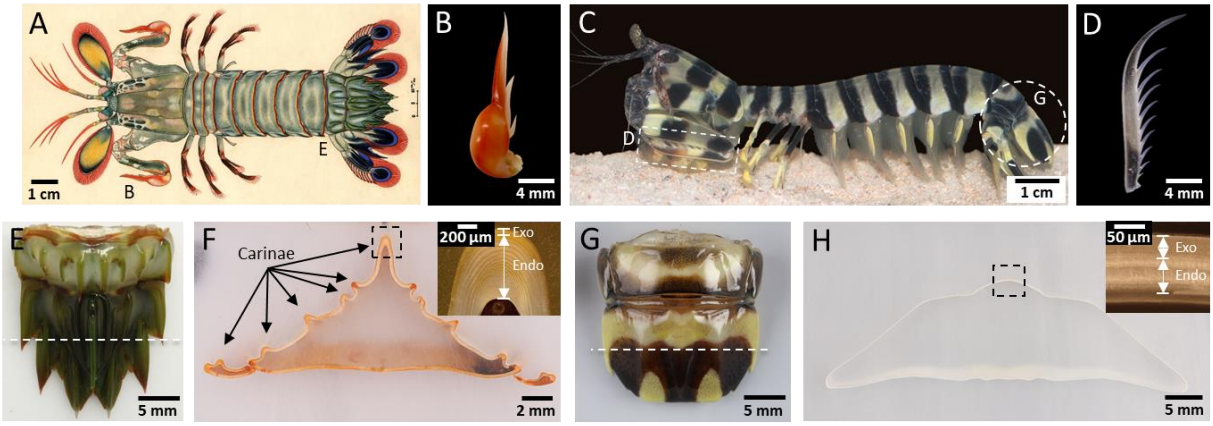

Figure 5.1: Telson overview and comparison of bulk morphologies, (A) Smashing type (*O. scyllarus)* mantis shrimp. (B) Hammer-like dactyl appendage of smasher stomatopod. (C) Spearing type (*L. maculata)* mantis shrimp. (D) Spear-like dactyl appendage of spearer stomatopod. (E) Telson of smasher stomatopod. (F) Polished transverse cross section of the smasher telson with plane of section denoted by dashed line in (E). (G) Telson of spearer stomatopod. (H) Polished transverse cross section of the spearer telson with plane of section denoted by dashed line in (G). Inset: Higher magnification optical micrograph of dorsal cuticle along center line. Micrography performed by N. Yaraghi, Kisailus group, UC Riverside. Adapted from [38]

5.3 Development of Computational Models

5.3.1 3D Models

Several types of computational models were constructed for this analysis. CAD geometries of the 3D smasher and spearer telsons were created from micro-CT scans of the telsons. In a process similar to what is described for the woodpecker in chapter 4, a combination of reverse engineering softwares were used to clean the stl files, fix internal holes and triangulation errors, and convert to NURBS surfaces from which the 3D CAD models were finally created. The original smasher geometry was then modified using sculpting tools in Geomagic (3D Systems, Morrisville, NC) such that structural features were systematically removed from the smasher telson in multiple models to create a set of intermediate geometries between the smasher and spearer telsons. CAD geometries were then exported for finite element analysis. Finite element meshes were created from the CAD files using commercially available FEA software (Abaqus). Simulations were

performed using Abaqus/Standard with meshes consisting of about 200,000 C3D4 elements. A linear elastic material definition was chosen with a Young's modulus of 1 GPa, since the analysis was aimed to be comparative between different geometries rather than absolute.

5.3.2 2D Plane Strain Models

To investigate mechanical response under impact, 2D cross-sectional geometries of the ridged smasher telson were extracted from the 3D models resembling figure 5.1F. A smoothened version of the 2D cross-sectional geometry was also created to act as a control geometry or a reference geometry. 2D geometries were chosen for the impact simulations to reduce the complexity of the problem while still investigating the effect of the ridges, and to reduce computational cost. Geometries were imported into Abaqus and converted into FE meshes with about 200,000 CPE4 plane strain elements. Impact was simulated against a circular impactor with radius of curvature similar to the dactyl club at impact velocities of 20 m/s to better match natural conditions. Impact simulations were performed in Abaqus/Explicit with free-free boundary conditions, meaning, both the telson and the impactor were allowed to move freely after impact. Results were compared between the ridged smasher model and the artificially created smooth smasher model. The impactor was modeled with a young's modulus of 30 GPa consistent with mechanical properties of the dactyl club as characterized in literature[14]. The 2D telson models consisted of an outer hard shell filled with inner soft tissue. The hard shell was modeled as linear elastic with young's modulus of 6 GPa taken from nanoindentation data[38]. The inner soft tissue was modeled both as linear elastic with a Young's modulus of 1 kPa in one set of simulations and as viscoelastic using a prony series for tissue obtained from literature[75]. The viscoelastic simulations are expected to show strain rate dependence of the shear modulus with a distinct instantaneous modulus, rate-dependent modulus and long term modulus as shown in figure 5.2.

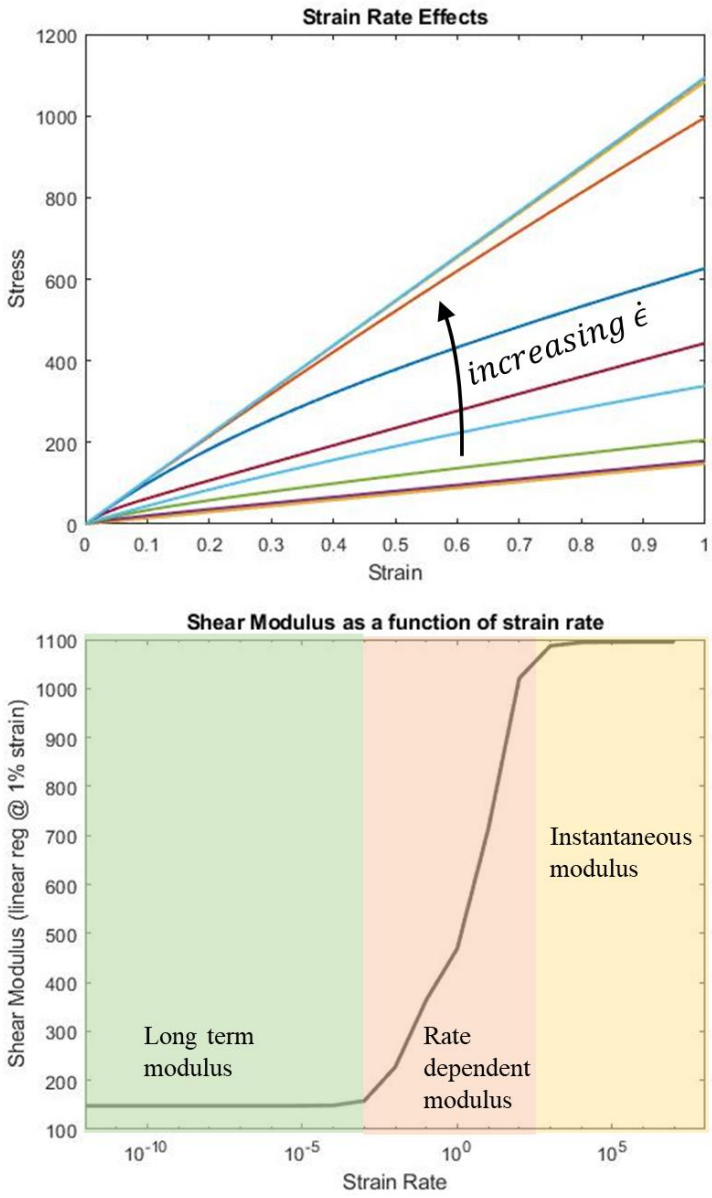

Figure 5.2: Strain rate dependent and distinct regions of shear moduli for the viscoelastic material used in simulations under impact.

5.4 Results and Discussion

5.4.1 Finite element Analysis on Effect of Ridge Geometry under quasi-static conditions

To assess the effect of the carinae geometry on the compressive stiffness of the telson, finite element simulations were performed on five different 3D models (Figure 5.3A). Computer Aided design (CAD) models for the smasher (denoted as SMSH) and spearer (denoted as SPER) telsons

were derived from micro-CT scans. To isolate the effect of the lateral ridges and medial carina, three additional models were created from the smasher telson through CAD manipulation. One geometry retained the medial carina but removed the lateral ridges (denoted as NRCC). In another modified model, the medial carina was removed, but the lateral ridges were preserved (denoted as NCCR). The third modified model consisted of a smoothened version of the smasher telson, containing no lateral ridges or medial carina, but maintaining the macrocurvature of the smasher telson (denoted as SMTH). Simulations were performed under two loading conditions; compression between two plates (henceforth referred to as top loading) and a lateral loading event against a sphere with a curvature similar to a dactyl club (henceforth referred to as lateral loading). To further probe the effects of ridge geometry, two more datasets were compiled. K1 SMTH refers to a variant of the smooth model (SMTH) in which the stiffness of the SMTH model was analytically scaled by a scaling factor K1 to match the stiffness of the smasher (SMSH) geometry under top loading. Then this same scaling factor K1 was used on the SMTH dataset to determine the stiffness response of K1 SMTH under lateral loading. Similarly, K2 SMTH is a scaled version of the SMTH model stiffness under lateral loading using a scaling factor K2. The same scaling factor is then used on the SMTH data set to obtain the stiffness response under top loading. Mean stiffness within error bounds was calculated for all models for up to 0.5 mm displacement under top loading (Figure 5.3B) and lateral loading (Figure 5.3C). The percentage change in stiffness as compared to the smasher (SMSH) model was calculated for top loading (Figure 5.3D) and lateral loading (Figure 5.3E) using the equation

$$\%\ change = \frac{K_{model} - K_{SMSH}}{K_{SMSH}} * 100$$

Here K_{model} refers to the stiffness for each respective model and K_{SMSH} refers to the stiffness of the smasher telson.

Comparison of the stiffness data shows that the loading direction plays a significant role on the effects of the carinae on stiffness response. Under top loading, the models containing the medial carina (SMSH and NRCC) show high stiffness as compared to the models that do not have the medial carinae (NCCR and SMTH). At the same time, the lateral ridges seem to add some compliance to the system (SMSH vs NRCC). The models without the medial carina show very low stiffness, as does the spearer model. Under lateral loading, the effect of the medial carina was noticeably reduced, though it still provided some stiffness to the system. Conversely, the effect of

the lateral ridges providing compliance seemed to be enhanced (SMSH vs NRCC or SMTH vs NCCR). The spearer model continued to show low stiffness in comparison, which can be attributed to the difference in macrocurvatures between the smasher and spearer geometries. K1 SMTH and K2 SMTH are useful tools in showing the effects of scaling achievable through modifications of thickness or Youngs modulus, on the stiffness. K1 SMTH which matches the stiffness of the SMTH model to that of the SMSH model under top loading, showed a disproportionately large response under lateral loading, with stiffness values of several orders of magnitude above that of the SMSH model. K2 SMTH which matches the stiffness of the SMSH model under lateral loading, showed an almost negligible change in stiffness as compared to SMSH under top loading. Together, these two data sets provide valuable insights in the importance of evolving ridged geometries as opposed to simple changes in thickness.

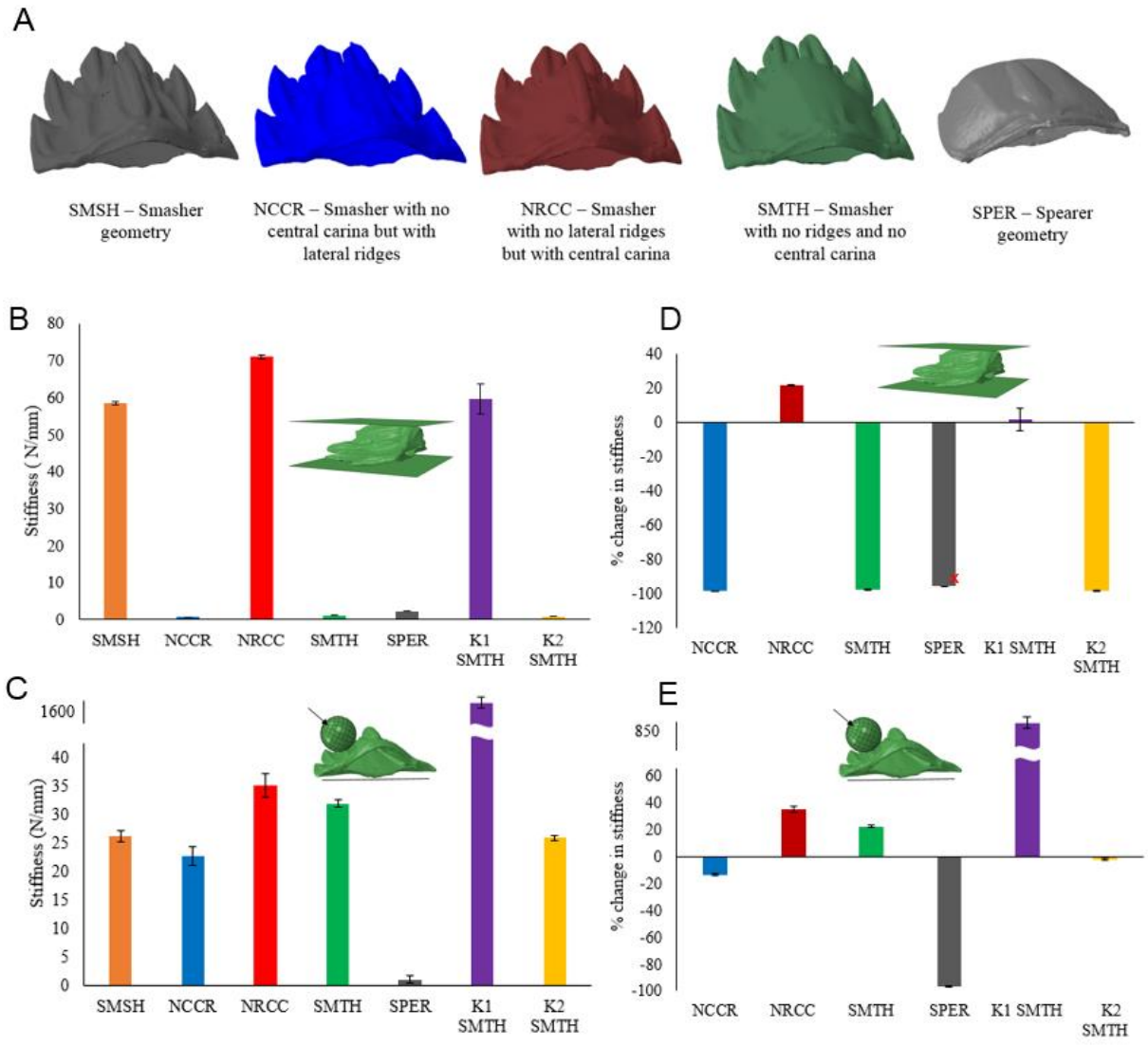

Figure 5.3: FE simulations on the effect of carinae geometries on stiffness. (A) Representations of CAD models used in the FE simulations with nomenclature. (B) Mean stiffness for top loading up to 0.5 mm displacement (inset: boundary conditions). (C) Mean stiffness for lateral loading up to 0.5 mm displacement (inset: boundary conditions) (D) Percentage change in stiffness as compared to the SMSH model under top loading. Corresponding change in stiffness for spearer geometry obtained from experimental data under top loading has been highlighted. (E) Percentage change in stiffness as compared to the SMSH model under lateral loading. Adapted from [38]

Follow-up experimental analysis using 3D printed mimics was also performed by collaborators and showed good qualitative agreement with the computational results as shown in figure 5.4.

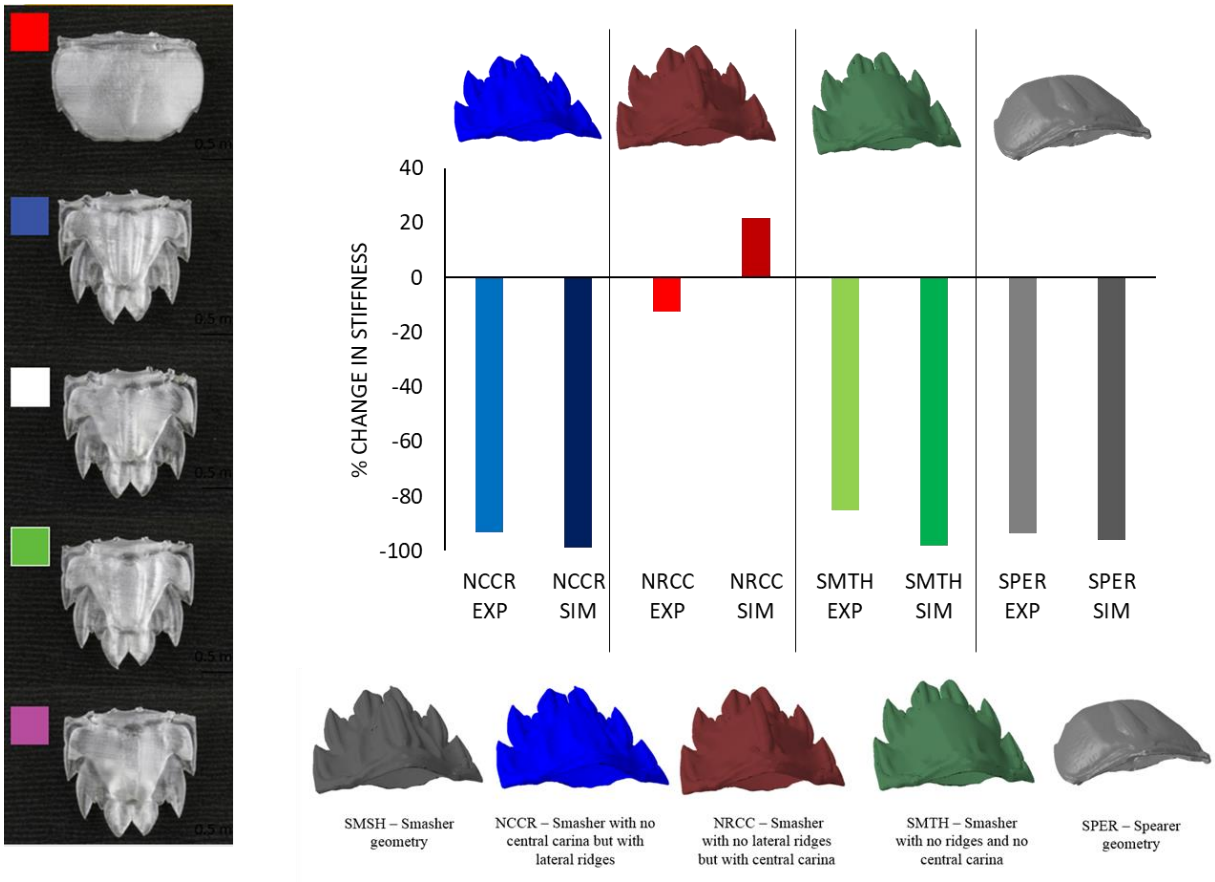

Figure 5.4: Comparison of experiments of 3D printed telson structures with simulation data indicating percentage change in stiffness as compared to the original ridged geometry shows good qualitative agreement with some variation for initial stiffness under quasi-static loading conditions. Color of curves indicate similar geometries in experimental and simulation with lighter color variants indicating experiment. Left bar shows 3D printed specimens while bottom bar shows 3D FE models. Experimental data acquired from J. Rivera, Kisailus group, UC Irvine.

5.4.2 Analysis of telson geometries under impact conditions

2D plane strain models of the ridged telson as well as a smoothened variant of the ridged telson were created from transverse cross sections of the smashing type telson. These structures were subjected to impacts from a circular impactor with radius of curvature similar to that of the dactyl club at impact velocities of 20 m/s consistent with those observed in natural conditions[14].

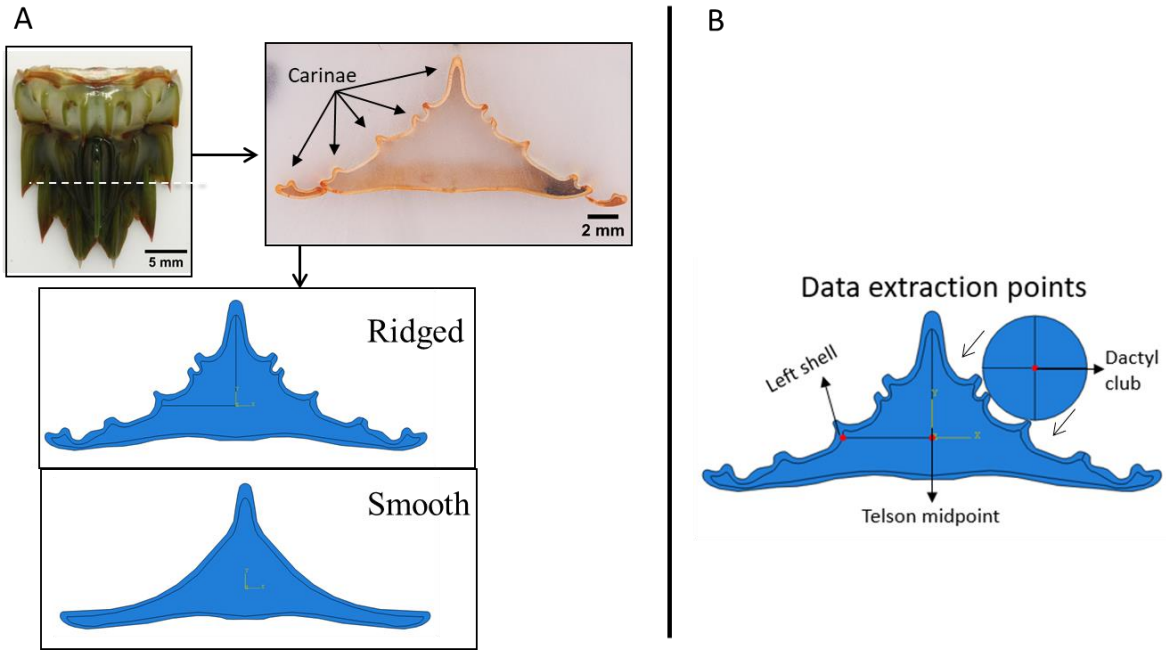

Figure 5.5: (A) Construction of two variations of 2D plane strain models from cross-sections of the smashing type telson. (B) Boundary conditions and data extraction points

Preliminary Simulations for effect of ridges in regions far from impact

Initial results showed that the ridged model experienced lower shear strains at the midpoint of the telson (Figure 5.6A) and on the telson shell in a region far away from the impact regions. Nodal accelerations extracted on the telson shell indicated larger vibration in the smooth model as compared to the ridged model (Figure 5.6B) indicating a possible effect of ridges in energy dissipation and impact mitigation. However, since quasistatic analysis of the telson geometry indicates that mechanical response is highly dependent on the direction and location of impact, a parametric analysis for loading at various points was then attempted.

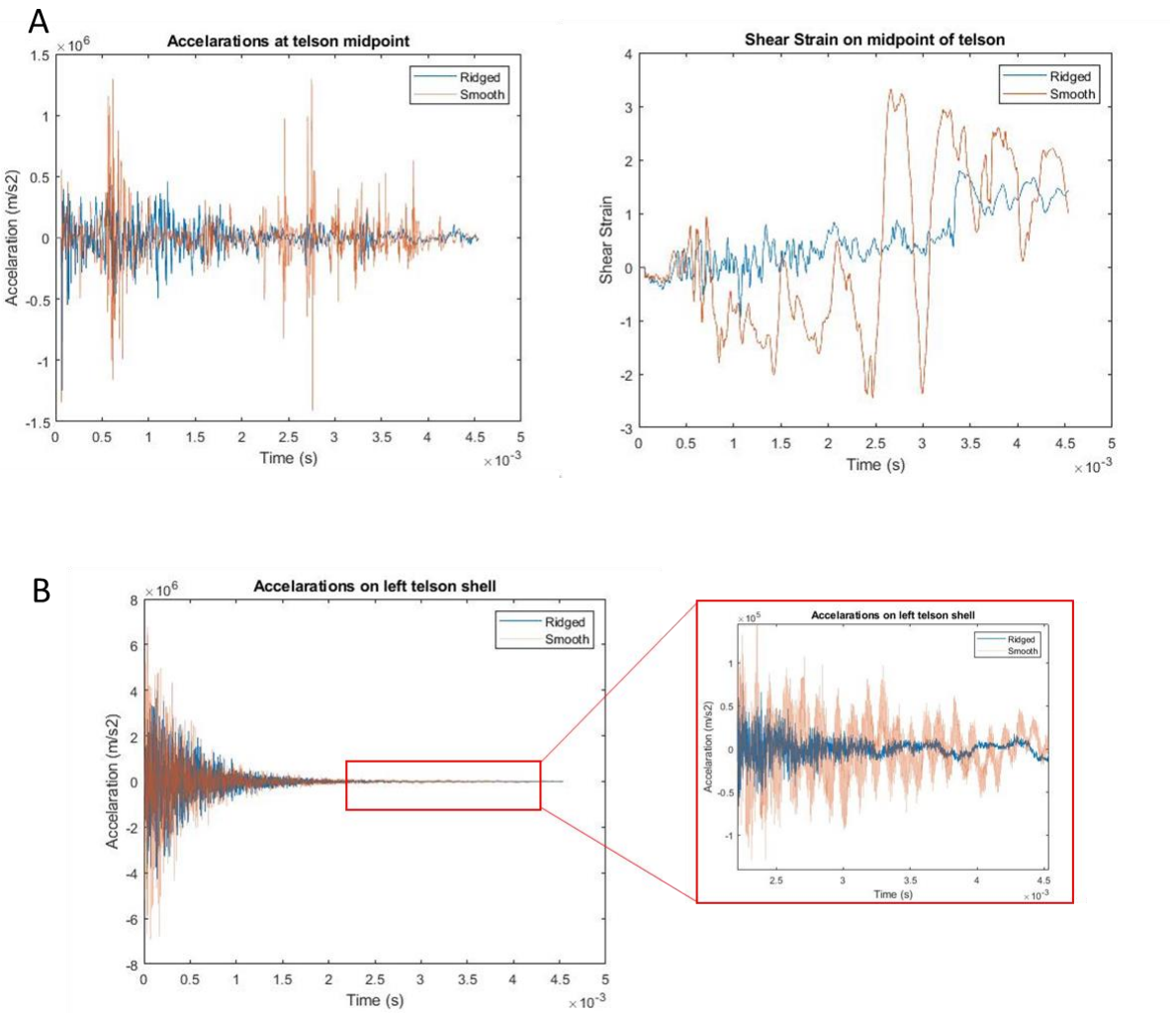

Figure 5.6: (A) Indicates accelerations and shear strain at the midpoint of the telson geometries for ridged (blue) and smooth (orange) models. (B) Indicates accelerations on the telson shell at a region far from impact with magnification of acceleration data inset.

Parametric Analysis for different loading directions

To show that the ridges play a role in energy dissipation, a parametric analysis was performed for different loading directions of the circular impactor. Ridged and smooth telsons were impacted 20 times at different angles of impact in different locations as shown in figure 5.7A. Shear strains were extracted at the telson midpoint and the telson shell at a region far from impact to assess the performance of the ridges. Shear strains extracted at the telson midpoint showed any effect of the ridges seems to be highly dependent on direction and location of impact with some impact locations showing lower shear strains in the ridged models while other impact locations displayed

higher shear strains in the ridged model. However, on the telson shell, a definite trend was observed with all simulations indicating lower shear strains on the left telson shell for the ridged model as compared to the smooth (figure 5.7B-F). While data was extracted from only one region, this does show that ridges have a definitive effect on reducing strains at regions far from the impact location on the telson shell, while their effect on the internal tissue is still unclear.

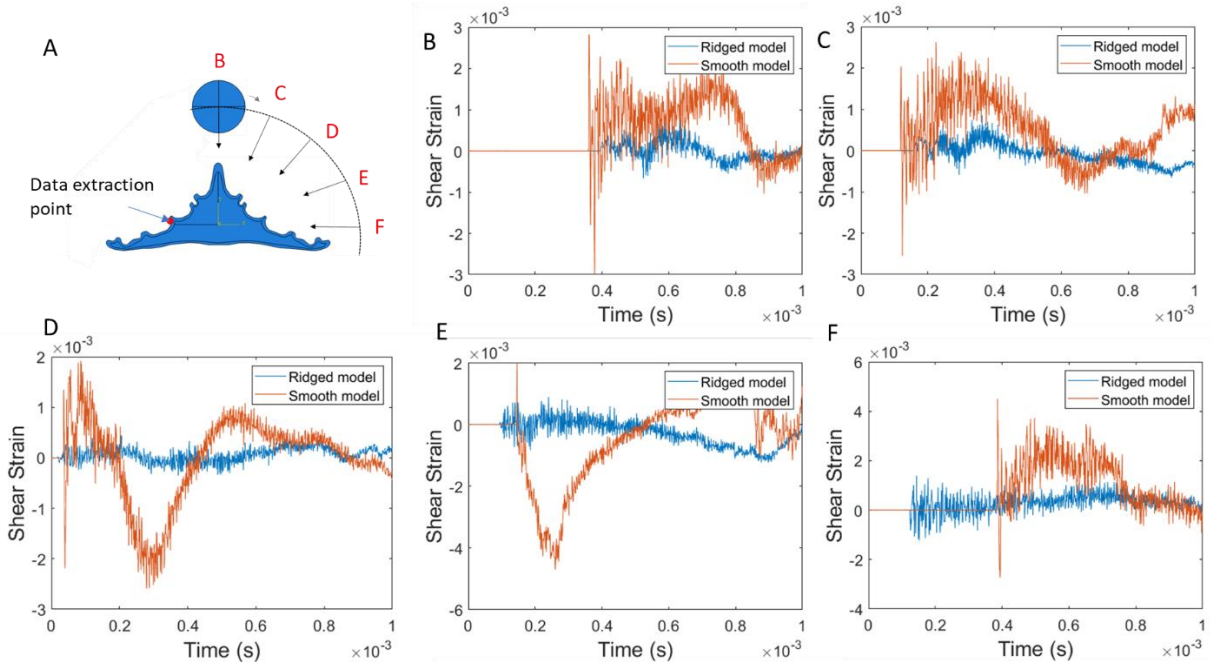

Figure 5.7: Parametric analysis for different loading directions. (A) Indicates different loading conditions considered. A total of 20 simulations were conducted with 5 of them being shown above indicated by red lettering. (B)-(F) Shear strain on the left telson shell at different loading directions for ridged vs smooth telsons.

FE Analysis of effect of ridges at impact location

Analysis of mechanical response at the location of impact can be difficult due to the large number of mixed frequencies in the stress pulse, and the complex geometries of ridges at the impact location and the associated interfaces between the hard shell and soft tissue in the telsons leading to multiple reflections of the stress wave. To evaluate the effect of ridges on a more qualitative scale, deformation of the side wall of the telson was observed during impact and compared between the ridged and smooth telsons (Figure 5.8). We found that while for the smooth telson, impact lead to a global bending of the side wall, the ridges on the telson side wall in the ridged model that

faced the direct impact deformed locally to prevent a global bending of the side wall. Deformation in the ridged telson models primarily consisted of deformation of the ridges under impact with further deformation arrested by the first ridge encountered that was not directly impacted. This was interesting in that it points to ridges acting almost as wave traps to retard the propagation of the stress wave by energy dissipation through local buckling.

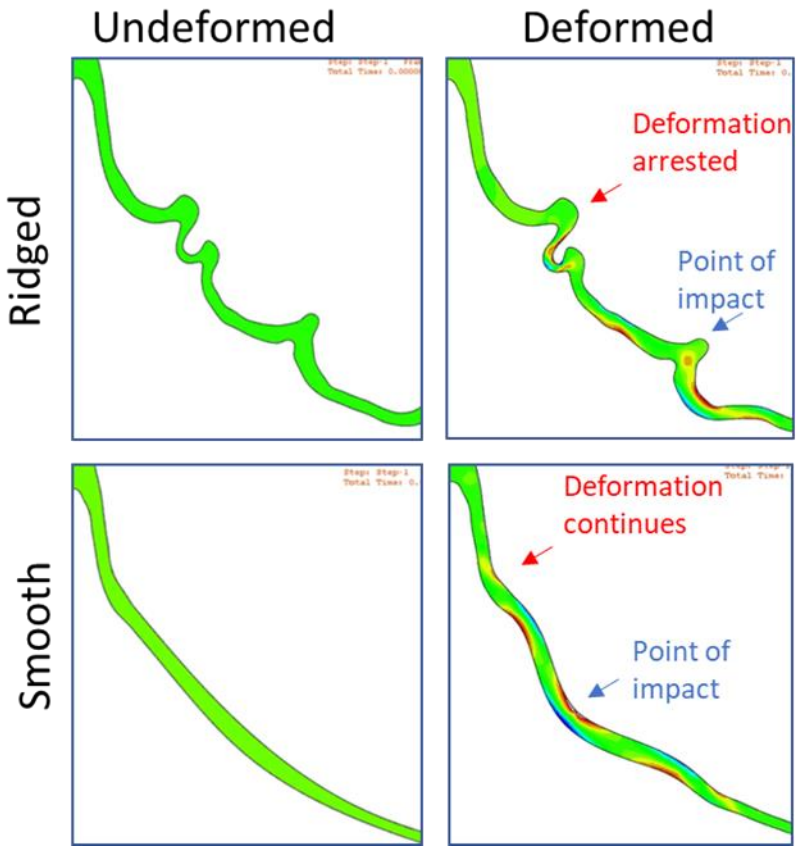

Figure 5.8: Deformation of telson side wall during impact at impact location for the ridged telson model (top) and smooth telson (bottom).

Analysis of Stress Wave Propagation during impact

Results from the previous section indicated that ridges may behave almost like wave traps retarding the propagation of the stress wave after impact. To further evaluate this behavior, we observed the propagation of the stress wave in the ridged and smooth telsons after impact. We noticed that there is a difference in time taken for the stress wave to reach the other end of the telson between the ridged and smooth telson (Figure 5.9). Since the ridged model has a longer travel path (due to the presence of ridges), we calculated the increase in path distance, but found

that it still did not account for the increased time lag in the stress waves between the ridged and smooth telsons. While the ridged model had ~15% longer path distance compared to the smooth model, the time lag in the stress waves was closer to 33%. We calculated the longitudinal (c_L) and shear wave speeds (c_s) for the material used for the telson simulations with

$$c_L = \sqrt{\frac{E}{\rho}} \quad , \quad c_s = \sqrt{\frac{G}{\rho}}$$

where E is the young's modulus, G is the shear modulus and ρ is the mass density of the telson material. Longitudinal wave speed was found to be 2450 m/s and shear wave speed was 1741 m/s. Analysis of the stress wave propagation found that while the stress wave front in the smooth model moved at the longitudinal wave speed, the speed of the wavefront in the ridged model was consistent with the shear wave speed. This observation is interesting since it seems to indicate that ridges may act to convert longitudinal waves to shear waves.

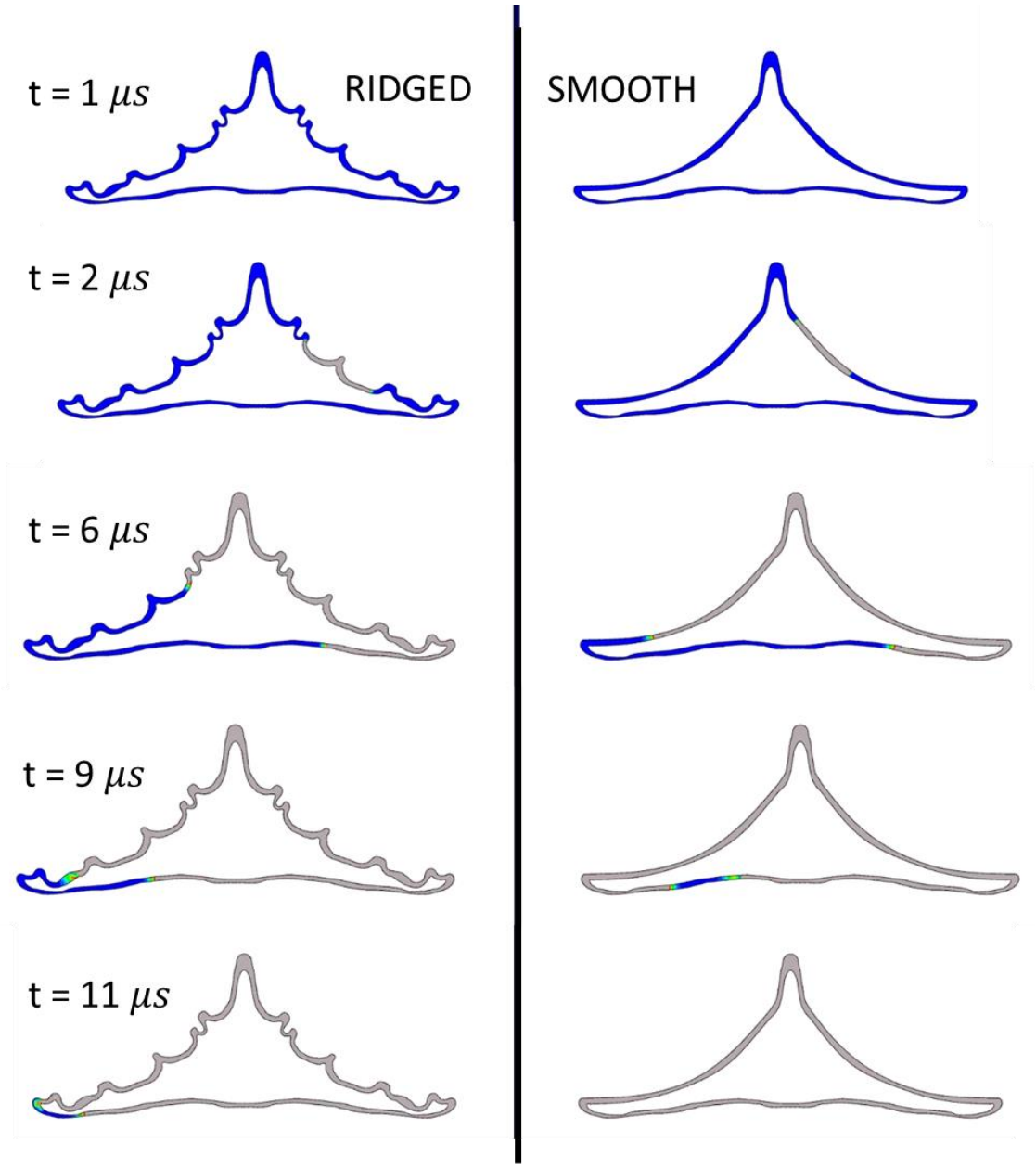

Figure 5.9: Differences in stress wave speed between ridged and smooth telsons. Grey indicates stress wave front.

Analysis of Simpler 2D Geometries for stress wave propagation

To further probe the idea that ridges may help convert longitudinal stress waves to shear waves in the thin telson shell, we constructed simple 2D geometries of smooth, sinusoidal and ridged beams to evaluate the differences in geometric composition on impact response (Figure 5.10).

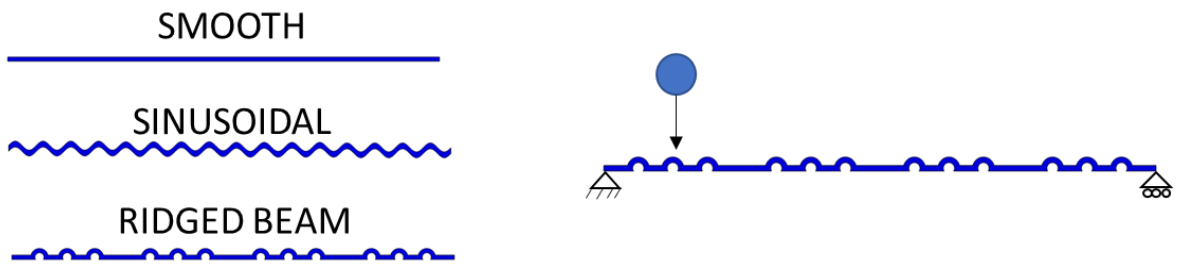

Figure 5.10: Three designed geometries tested under impact with boundary conditions shown on the right.

First, a modal analysis was performed to evaluate the effect of geometrical parameters on the free vibration response. We discovered that sinusoidal and ridged models presented a new mode (mode 5) that consisted of a movement associated with flattening of the ridges and sinusoids (Figure 5.11). While we cannot be sure if this mode is activated during impact, it does agree with previous observations in the telson of local bending or flattening of the ridges under impact.

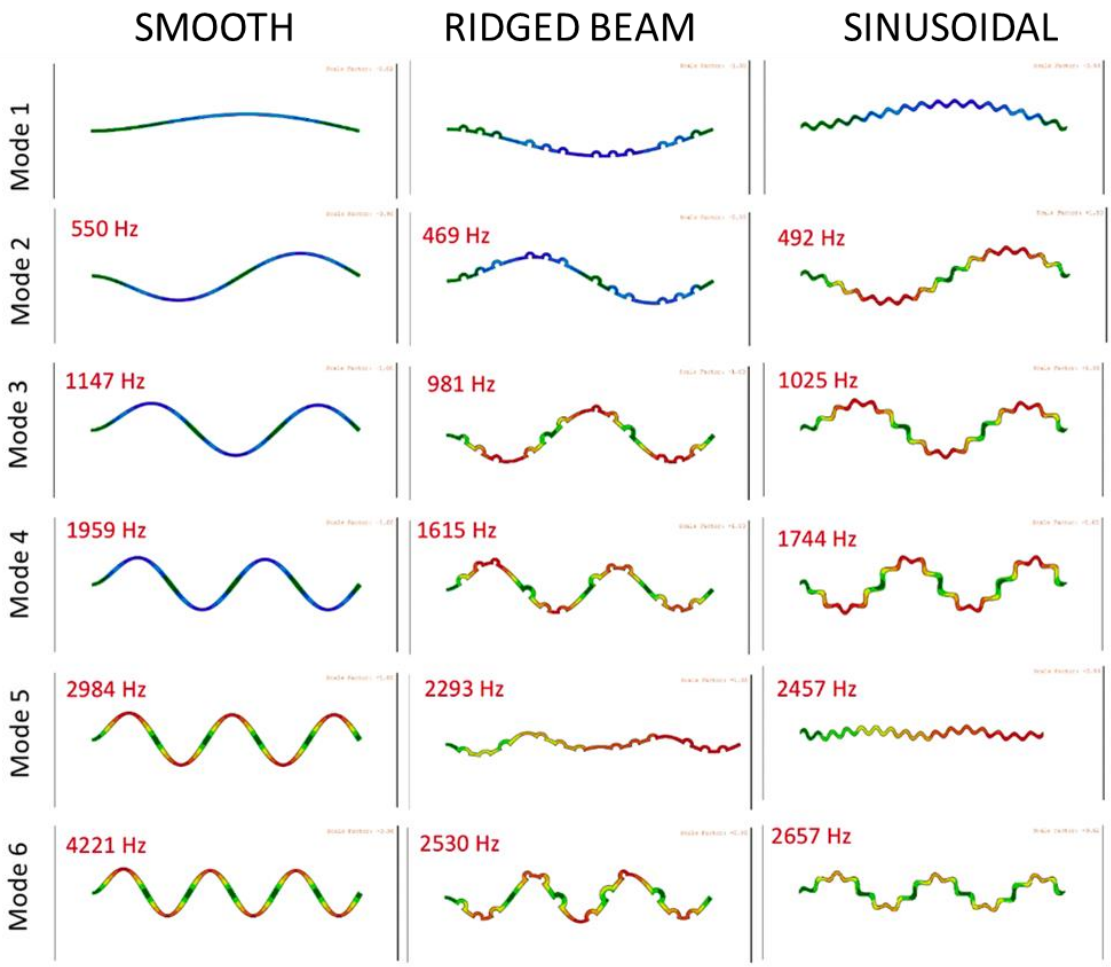

Figure 5.11: Frequency modal analysis for smooth, ridged and sinusoidal geometries shows the presence of a new mode (mode 5) in sinusoidal and ridged geometries that is consistent with flattening of the ridges.

Finally, an impact analysis was performed for the three models against a circular impactor. We quantified the principal stresses and their directions during stress wave propagation and found that both the ridged and the sinusoidal geometries showed principal stresses in transverse directions not in line with the direction of wave propagation indicating the presence of shear waves (Figure 5.12). For the smooth model, all principal stress directions were in line with the direction of wave propagation. The conversion of longitudinal waves to shear waves and subsequent filtration of shear waves by ridged geometries has been previously demonstrated in the horns of big horn sheep[76]. Ridges in the telson could also play a similar role in conversion of impact waves to shear waves. Furthermore, previous work has shown that the bouligand microstructure

of the dactyl club is able to filter shear waves[37], and while a similar microstructural analysis of the telson is lacking, maybe, the telson microstructure also plays a role in filtering shear waves.

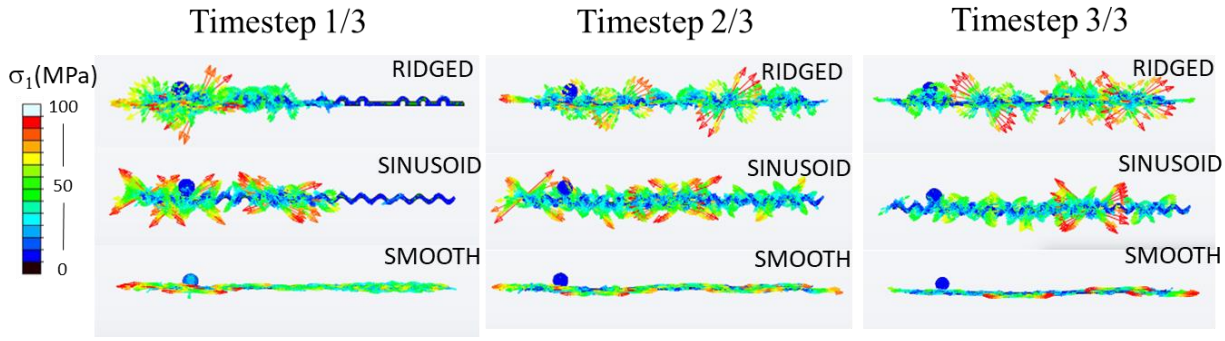

Figure 5.12: Principal stress magnitude and directions for ridged, smooth and sinusoidal models at three different time steps of the simulation.

5.4.3 Effect of Ridged shells with viscoelastic cores

Most of the previous work has focused on understanding the effect of ridges of the hard telson shell on impact mitigation and energy dissipation. In this section, we also consider the viscoelastic inner soft tissue in the models to identify if the presence of ridges affects wave propagation in the soft tissue. Since the soft tissue in the telson has not been characterized, we use tissue mechanical properties of brain which are expected to be similar from literature[75]. We performed simulations for ridged and smooth telsons with viscoelastic inner tissue but could find no statistically significant differences in the response. To isolate the effect of a single ridge from the geometric variations in the telson, we modeled 2D box geometries consisting of hard outer shells and soft viscoelastic inner cores. Two models were created, one which had a single ridge on the outer shell, while the other was smooth. Box dimensions were kept in the range of the telson, and nodal stress and strains were extracted for a set of nodes in the center. Figure 5.13 shows equivalent strain (a strain conjugate to vonMises stress) for ridged vs smooth box geometries. Again, no significant differences between the ridged and smooth models was discovered. One reason that could mask any differences is because of continuous reflections of the stress waves off the boundaries of the models after impact. We know that the stress wave speed is given by

$$c = \sqrt{\frac{E}{\rho}}$$

where E is the effective elastic modulus and ρ is the mass density. The hard outer shell has an effective elastic modulus in the GPa range while the soft inner tissue has a modulus in the kPa range. This results in a large orders of magnitude difference in wave speeds between the outer shell and the inner core. Therefore, the stress wave propagates through the outer shell multiple times before it propagates into the inner tissue causing multiple points of ingress into the tissue, affecting the response and masking any effect of the single ridge.

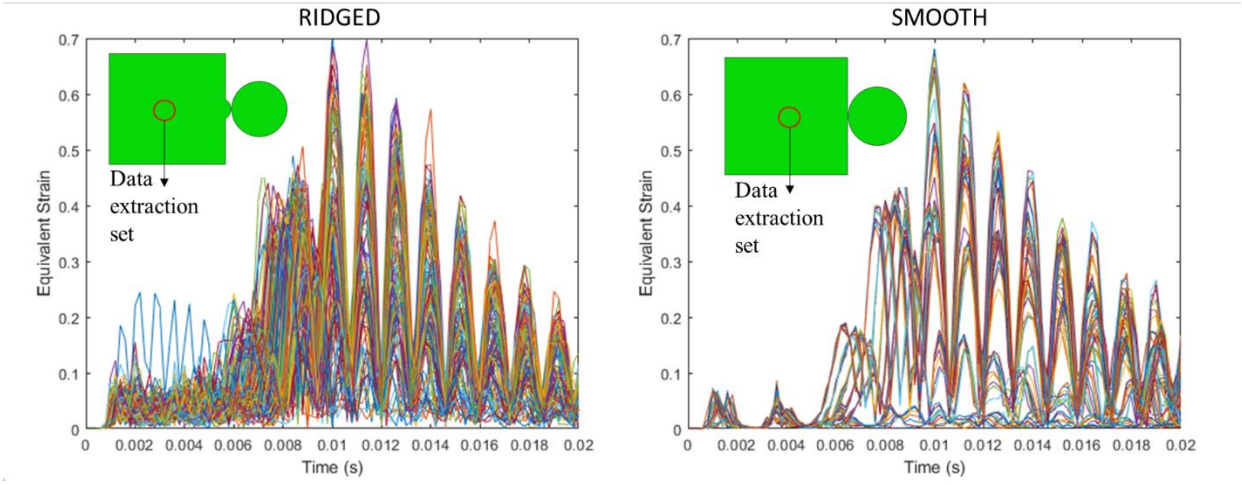

Figure 5.13: : Equivalent strain comparison between ridged and smooth box geometries. Inset: The box geometries with red circle indicating set of nodes from where data was extracted.

To eliminate the effect of reflections off the boundary and evaluate the transient response, a new set of 3D simulations were considered with different geometries. Geometries consisted of solid cylinders with viscoelastic cores. Two geometries were constructed, the first consisted of ridges running along its length, and the second was a smooth cylinder. Both the axial ends of the cylinders were assigned non-reflective boundary conditions for the hard shell. Non-reflective boundary conditions allow the stress wave to continue propagating out of the model, and therefore prevent reflections from the boundary. In theory, this would give time for the stress wave to propagate into the viscoelastic material without additional stress information from the boundaries affecting the result. Models were then subject to a very small duration impact pulse at the center in the transverse direction. A low magnitude impact pulse with very low impact duration was chosen such that all stress information would enter the models before the stress waves encountered boundaries. Observation of the stress contours during wave propagation seemed to indicate that

the ridged variant displayed a damping of the vibrations when compared to the smooth with vibration velocities decreasing at a larger rate than the smooth. We extracted the energy dissipated by viscous forces and found that the ridged model displayed higher energy dissipation (Figure 5.14). In the previous section, we showed that ridged geometries convert longitudinal waves to shear waves. Perhaps the presence of shear waves in the viscoelastic material for the ridged cylinder accounts for the increased viscous dissipation.

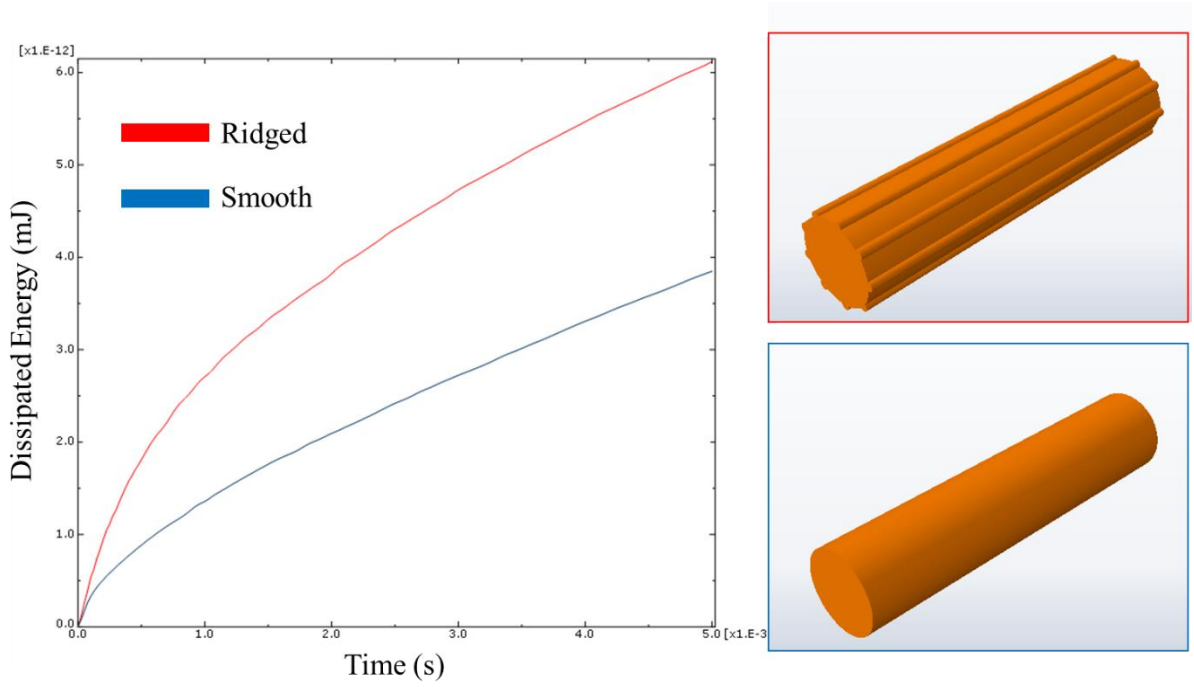

Figure 5.14: Viscous dissipation energy for the ridged vs smooth cylinder models.

5.5 Conclusions

The results reported here indicate some very interesting mechanical effects of ridges in the telson geometries. Quasi-static simulations of the 3D telsons between smasher and spearer telsons indicated that the presence of a medial ridge in the smasher telson provides out-of-plane stiffness whereas the presence of lateral ridges suggests a role in providing compliance for energy absorption. This highlights the subtle interplay between the stiffness provided by the medial carina and compliance provided by the lateral ridge to give the smasher telson its stiffness under multiple directions of loading. To understand mechanical response under dynamic loading conditions, we focused on the smasher telson and a smoothened variant of the smasher. A parametric analysis of 2D telson geometries under different loading directions indicated that the mechanical response

was dependent on the loading direction and angle of attack. Areas on the telson shell far from the impact location displayed lower strains in the ridged telson as compared to the smooth variant indicating an effect of the ridges in lowering strains. Investigation of mechanical response at the impact location suggested that local bending of ridges at impact location act to arrest the deformation and prevent global bending of the telson sidewall. Ridges act almost as wave traps retarding stress wave propagation. Calculation of stress wave speeds and quantification of principal stress and stress directions suggest an ability of ridged geometries to convert longitudinal waves into shear waves. Conversion of longitudinal waves to shear waves by ridged geometries has been shown before in big horn sheep[76] and shear wave filtering effects of microstructures in the mantis shrimp have been shown before as well[37]. Vibrational analysis of ridged beams indicated the presence of a new natural frequency mode consistent with bending of ridges and further corroborates mechanical response at impact location. An analysis of ridged geometries with an outer hard shell and inner viscoelastic core highlight the ability of ridged geometries to show larger viscous damping and energy dissipation, likely due to the presence of shear waves in the viscoelastic tissue. Overall, these results highlight advantages of ridges in energy dissipation, stiffness control and impact mitigation. They provide useful design cues in manipulating stiffness and energy dissipation in structures under multidirectional loading. Through the use of several different computational techniques, this chapter identified structural adaptations, the ridges, that play a role in impact resistance through local buckling, and stress wave retardation through the conversion of longitudinal waves to shear waves. To extend the notion to bioinspired structures, we use the findings from this chapter to describe novel geometries with tailorable stiffness and energy dissipation for applications in engineering structures in the next chapter.

6. MECHANICS OF RIDGED SHELL METASTRUCTURES FOR TAILORABLE STIFFNESS AND ENERGY DISSIPATION

Parts of chapter 6 will be included in the publication – A. A. Trikanad, P. Zavattieri, "Mechanics of ridged shell metastructures for tailorable stiffness and energy dissipation", Status: In preparation

6.1 Introduction

Chapter 5 described ridged geometries in mantis shrimp telson which display variable stiffness and energy dissipation through geometric variations in the ridges rather than material composition. Here, we attempt to extend the concept to engineering structures by designing bio-inspired geometries with enhanced stiffness and energy dissipation as well as building a mechanistic explanation for the deformation behavior such that mechanical response can be tailored to specific applications. For the initial design, we focused on the side wall of the smashing type mantis shrimp telson. One side wall of the telson cross section was extruded out of plane to create a 3D shell structure. The telson side wall has an associated curvature as well as a set of ridges curved in the opposite direction. To simplify the bio-inspired structure, we focused on a single ridge running through the center. The resulting model consisted of a thin shell geometry with transverse curvature, with a single ridge with the opposite curvature running through the center (Figure 6.1).

Previous research has shown that thin elastic shells can display intriguing mechanical instabilities. Due to their slender cross sections, small geometric variations can result in large macroscopic mechanical responses due to buckling[77]. Shell based structures have been previously used as unit cells in architectured materials to display unique and non-intuitive elastic responses such as negative poisson's ratio[78], [79], and negative stiffness[80]–[83] through clever geometrical manipulations to harness elastic instabilities under bending. Materials displaying such non-conventional properties are known as elastic metamaterials and are a hot topic of research and development with their ability to manipulate mechanical response through structural manipulation[22], [84]–[86]. In chapter 2, we discussed the difference between stretching and bending dominated structures in cellular lattices. Shell based structures are generally utilized as bending dominated structures to harness elastic instabilities caused by the thin cross sectional geometries and internal curvatures.

Shell based structures can produce snap-through elastic instabilities with the ability to snap from one energetically stable state to another. Snap-through instabilities are characterized by a reduction in the equilibrium force and a reversal of displacement through bending or buckling in the shell. Snap-through behavior generally shows hysteretic behavior between the loading and unloading paths and consequently, displays energy dissipation characteristics. Importantly, this elastic behavior is repeatable because the material stays in the elastic regime. In order to attain this behavior, researchers have resorted to inducing prestress during the manufacturing process in composite shell structures to create elastic instabilities that can trigger snap-through mechanisms. Riley et al[87] developed composite shells inspired by the leaves of the venus fly trap designed with magnetically reinforced composites which introduced pre-stress to induce snapping behavior. Other researchers have used thermal prestresses in the manufacturing process of composite shells to induce similar snapthroughs[88], [89].

In this regard, natural systems provide an advantage in such a design space because they evolve structural adaptations to make up for a lack of material composition. Lessons learned from nature can help to design such shells with snap through instabilities without the need of pre-stress. Indeed, Holmes and Crosby[90] designed venus fly-trap inspired hemispherical elastomeric shells capable of two stable configurations for applications towards optical lens. Similar domed structures have been used by other researchers to design metamaterial sheets with controllable shape morphing for actuation in soft robotics[84][91].

The shell design in this work is extruded from one side wall of the telson (Figure 6.1). It can be described as a straight tin-walled elastic strip with a curved cross-section, with a ridge of opposite curvature running through it in the longitudinal axis. Without the central ridge, these structures resemble a ligament from a carpenter's tape (or a tape spring). Tape spring ligaments have been studied before and display snap through behavior and associated energy dissipation characteristics when bent in the direction opposite to the direction of transverse curvature[92]. Recently, Hector et al[81] developed hexachiral cellular materials using tape spring ligaments as the unit cells and displayed reversible enhanced energy dissipation when the constituent tape springs were bent in the opposite sense (Bending in direction opposite to transverse curvature of the tape). Runkel et al[82], [83] connected two oppositely oriented tape springs to develop chiral lattice topologies for applications towards structural damping control, vibrational control and noise mitigation. In this work, we aim to extend the concept of the tape spring ligament, by introducing

a ridge of opposite curvature running through its center and analyze its mechanical behavior as compared to the conventional tape spring ligament.

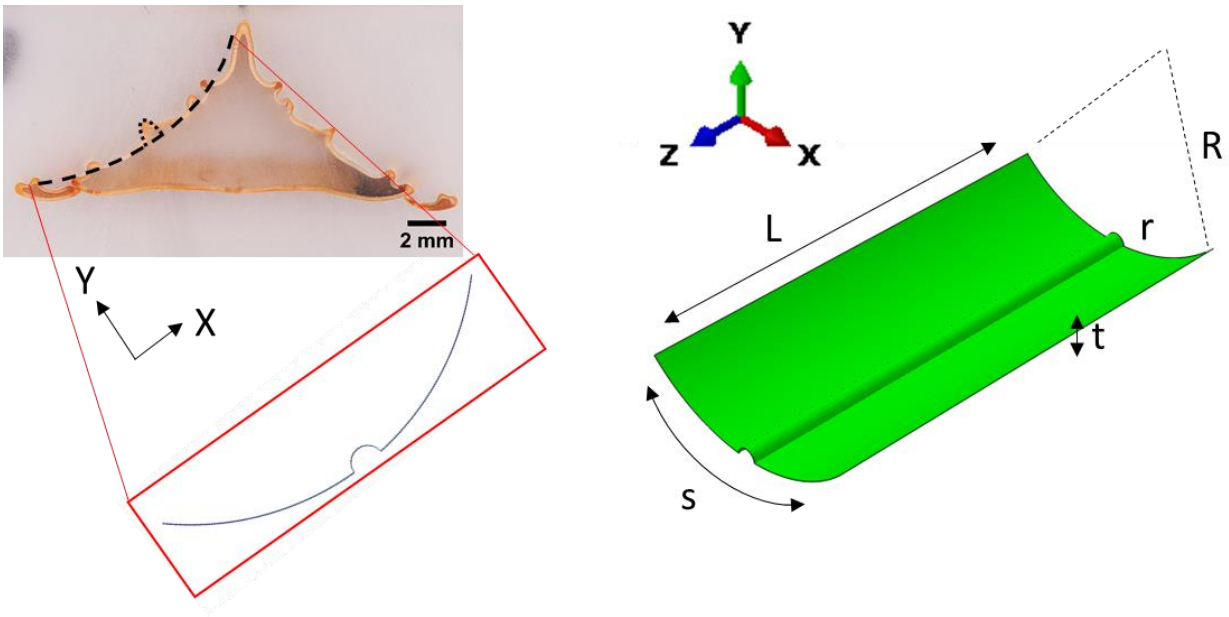

Figure 6.1: 3D ridged shell structure designed from telson side wall and extruded in the z-direction. Also shown are the different geometrical parameters that are used in this study.

6.2 Methods

6.2.1 Finite Element Modeling

CAD models of ridged 3D shell geometries were designed in the Abaqus pre-processor for analysis. 3D shell geometries without a ridge (similar to a tape spring ligament) were also constructed to act as control geometries. Linear elastic material definitions with Young's modulus of 1 GPa. Since this analysis focuses on structural effects and all results are normalized by a similar tape spring geometry, absolute material characterization was not required. Simulations were performed in Abaqus/Standard. Tape springs were coupled to reference points at each end, and a point in the middle was fixed to prevent rigid body motion. Rotational displacement was applied to the reference points at the boundaries and reaction moments were extracted from the boundaries. Rotations were applied to simulate same sense (rotation in the direction of transverse macrocurvature of ridged shell) as well as opposite sense (rotation in direction opposite to the transverse macrocurvature of the ridged shell). To perform parametric analysis with varying

geometrical parameters, custom python scripts were written capable of automated sequential simulations with systematic variation in individual geometric parameters.

6.2.2 Experimental

To validate finite element simulations for stiffness characterization, four point bending experiments were performed on three samples with differing ridge sizes. Experiments were performed on an MTS universal testing machine at a loading rate of 1 mm/min to minimize dynamic effects. Samples were additively manufactured using a Formlabs Form 2 SLA style 3D printer using custom Formlabs material (Grey Pro - Young's modulus of 2.6 GPa post-cured as per material datasheet).

6.3 Results and Discussion

6.3.1 Response under pure bending

To determine the effect of ridges in the mechanical response of these shells, a parametric analysis was performed where the radius of the ridge was changed from zero, indicating no ridge (same as reference structure) to the arc length of the shell, indicating a ridge that occupies the entire transverse cross-section of the shell. Rotational displacement was applied to the models so as to simulate pure bending and reaction moments were extracted from the ends (Figure 6.2). Ridged geometries showed snapping behavior (characterized by a straight vertical drop in the reaction moment) in both directions of bending as opposed to conventional tape spring ligaments which show snapping behavior in only the opposite sense of loading. Snapping behavior yields energy dissipation characterized by hysteresis in the loading-unloading cycle. One characteristic moment-rotation plot is shown in figure 6.2 (inset in blue).

Opposite Sense Bending

While both directions of loading yielded snapping behavior, there were differences in the responses. For opposite sense, when radius of ridge was zero, it displayed snapping behavior. This is expected since it behaves exactly like a tape spring ligament bending in the opposite sense. This was followed by a range of ridge radii for which opposite sense bending yielded no noticeable

energy dissipation or snapping behavior. A secondary range then emerged, where there was non-zero energy dissipation in the opposite sense. Finally, as the ridge radius got closer to the arc length of the parent structure, there was a range that again displayed conventional buckling with no snapping or hysteretic behavior.

Same Sense Bending

When bending in the same sense, as expected, no energy dissipation was seen at ridge radius of zero, similar to a conventional tape spring. An initial range of ridge radii displayed conventional buckling behavior, followed by a range of ridge radii that displayed snap-through instabilities and energy dissipation characteristics. Interestingly, as the ridge radius was further increased, reaction moments after snapping displayed negative values. This suggests the presence of a secondary deformation state where reaction moment is zero, indicating an ability of the structure to maintain a stable secondary configuration and display bistable behavior. This could have useful applications in shape morphing structures with the ability to showcase two stable states on command.

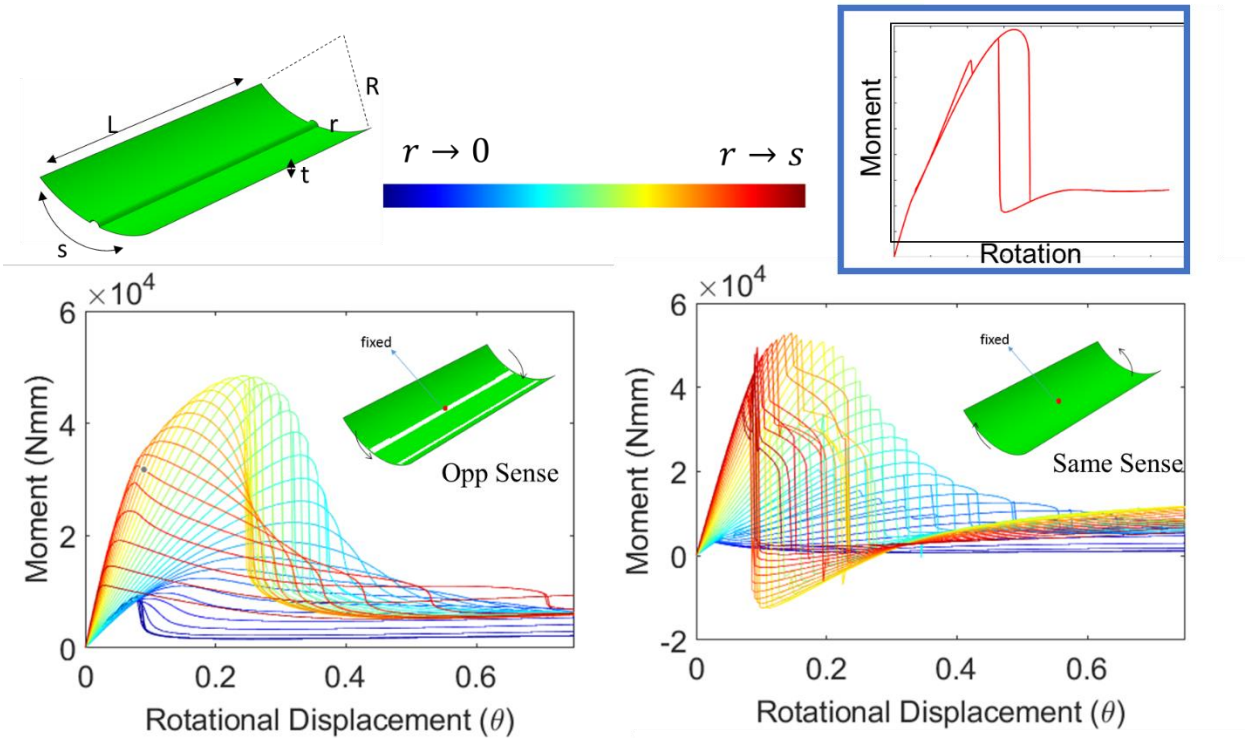

Figure 6.2: Moment vs Rotation plots in opposite sense and same sense bending for varying ridge radii from r = 0 to r = s. Inset in blue is a characteristic hysteresis loop for one of the ridged geometries

6.3.2 Dimensionless Analysis

To investigate the role of structural parameters on the mechanical response with a focus on the ridged geometry, we performed a dimensionless analysis with the Buckingham Pi theorem to determine the different pi groups that control the deformation behavior. Input parameters consisted of five independent geometric parameters; L is the length of the tape, r is the radius of the central ridge, t is the thickness of the tape, s is the transverse arc length of the parent structure and R is the macrocurvature of the transverse cross-section. Two material parameters were also considered with E as the elastic modulus and σ_y as the yield strength. Output parameters of interest included the bending stiffness, peak moment and the dissipated energy. With eight physical variables and two base units (force and length), six linearly independent dimensionless groups were determined. They are as follows:

$$\pi_1\,(output) = \frac{KL}{2EI} \quad , \quad \frac{P}{P_{control}} \quad , \quad \frac{E_d}{E_{d_{control}}}$$

where K is the bending stiffness, E is the elastic modulus, and I is the moment of inertia. P is the peak moment and E_d is the dissipated energy defined by the area occupied by the hysteresis loop in the loading-unloading curve of the moment rotation plots. Each parameter is normalized by its corresponding value for the control or reference sample which is the shell with no ridge (conventional tape spring ligament). Since the control sample does not dissipate energy under same sense bending, the energy dissipated as well as the peak moment under opposite sense bending was used as a normalization parameter for the dimensionless groups concerned with energy dissipation and peak moments. π_1 in essence, denotes the output dimensionless group.

Input dimensionless groups were then identified as

$$\pi_2 = \frac{L}{s}$$

π_2 is a consideration of the longitudinal aspect ratio. The importance of this parameter stems from the effect of proximity to the boundary where rotation is applied. It is important that this parameter remain large enough that deformation response is not influenced by boundary effects.

$$\pi_3 = \frac{2r}{s}$$

π_3 determines the proportion of the transverse cross-section that is occupied by the central ridge. π_3 is the input dimensionless parameter that is of most interest in this study.

$$\pi_4 = \frac{t}{s}$$

π_4 is a structural parameter that denotes effective thickness. Since the intriguing mechanical instabilities displayed by shells in general require thin and slender cross-sections, it is important that this parameter stay small so as not to affect the overall response.

$$\pi_5 = \frac{s}{R}$$

π_5 in essence denotes the effect of transverse macrocurvature of the parent shell. It essentially defines the angle of curvature used for these shells. Snap-through instabilities do not occur if these shells display no transverse curvature, and changing this parameter may have effects on the overall response.

$$\pi_6 = \frac{\sigma_y}{E}$$

π_6 is a dimensionless group that controls the effect of material properties on the mechanical response. This group determines if the effect of the structural properties can allow the shells to stay in the elastic regime without undergoing plastic strain.

Stiffness Response

Using the dimensionless parameters defined in the previous section, we quantified the effect on the normalized pre-buckling stiffness with variation in π_3 (proportion of arc occupied by ridge) as shown in figure 6.3A. Stiffness response was similar for same sense and opposite sense bending. Interestingly, ridged shells showed an initial compliant behavior with a decrease in stiffness as compared to a shell without a ridge for smaller ridge sizes, followed by an inflection point after which there was a constant increase in stiffness with increasing ridge size. This indicates that there is a ridge size for which the stiffness of a shell without a ridge is the same as the stiffness of the shell with a ridge (at $\pi_3 = 0.43$). This theoretically allows designers to consider applications where one is interested in maintaining stiffness while varying other mechanical properties. Further increases in ridge size allows for large gains in stiffness with up to 4 times higher stiffness than a shell without a ridge.

On closer investigation of the deformation behavior around the minima ($\pi_3 = 0.275$), we found that the inflection point is consistent with a change in the deformation mechanism (Figure 6.3B). For models where $\pi_3 < 0.275$, material points at the junctions where in the inner ridge meets the outer shell move towards the center after load application. In models where $\pi_3 > 0.275$, material points move away from the center towards the edges. To further probe this change in deformation behavior, we extracted principal stress directions after loading for two models, one on each side of $\pi_3 = 0.275$ (Figure 6.3C). Evaluation of the principal stress directions indicate the presence of competing mechanisms in the model. When load is applied, due to the transverse curvature of the macroshell, compressive stresses (red arrows) are generated at the outer edges of the macroshell. This induces tensile forces at the junction between the ridge and the outer shell because the structure is attempting to flatten the edges (blue arrows). When ridge sizes are small, the effect is dominated by the tensile forces on the outer shell and causes the material points in the junction to move inwards towards the center. However, when the central ridge is big (>0.275), the inner ridge acts in a similar fashion to the outer shell, but with an opposite curvature. Therefore, it induces tensile stresses at the junction which dominate the deformation characteristics and force

the material points at the junction to move outwards. This intriguing interplay between the competing mechanisms of the outer curved shell and the oppositely curved inner ridge help to produce elastic instabilities that provide non-intuitive mechanical behavior on the macroscale.

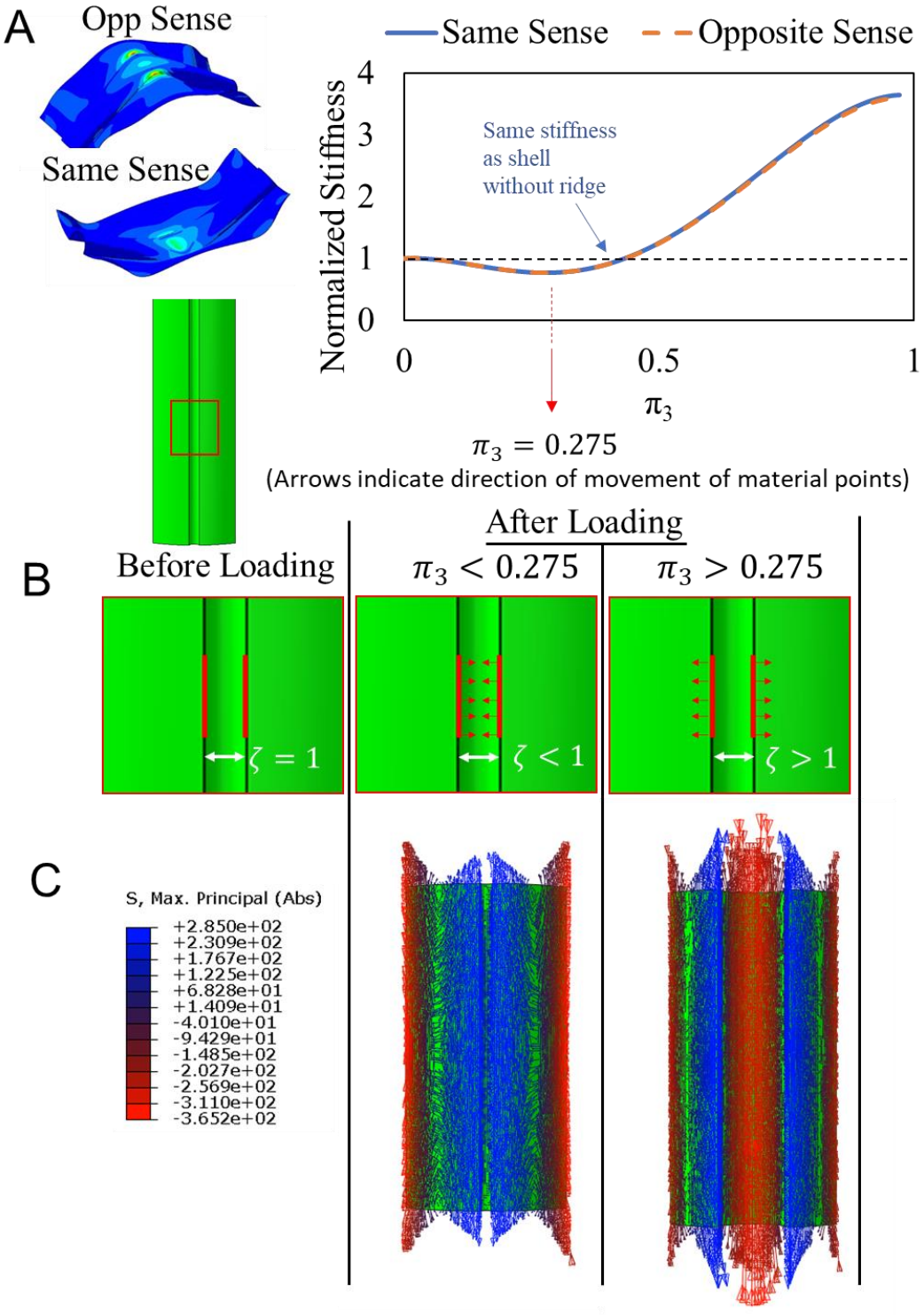

Figure 6.3: (A) Stiffness response for varying ridge size for same and opposite sense bending. (B) Schematic describing movement of material points for models with π_3 lower or higher than 0.275. (C) Principal stress directions for models at π_3 lower or higher than 0.275 where red indicates compressive stress and blue indicates tensile stress.

Experimental Verification of Stiffness Response

In the previous section, we showed with FE simulations that shells with smaller ridge sizes demonstrate lower stiffness than a shell with no ridge (tape spring ligament) while shells with larger ridge sizes demonstrate higher stiffness than a shell with no ridge. To corroborate these findings, we performed four-point bending tests on three specimens. A control specimen consisting of a shell with no ridge, a specimen with $\pi_3 < 0.43$ and a shell with $\pi_3 > 0.43$. Evaluation of load-displacement data showed an excellent match with simulations and confirmed the findings showing that the presence of a change in mechanism allowing ridged shells to show both compliance as well as increased stiffness depending on the size of the central ridge (Figure 6.4).

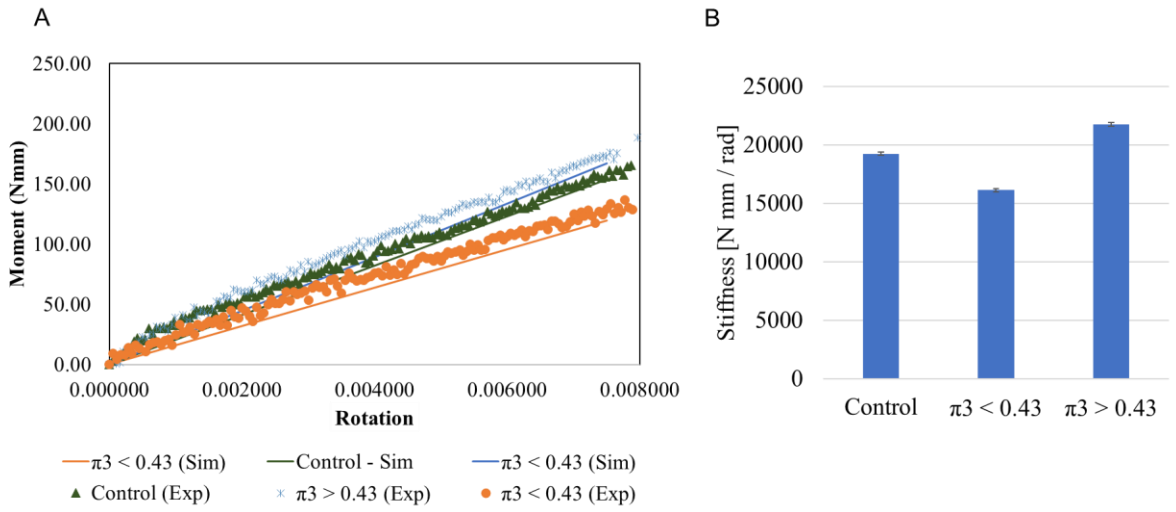

Figure 6.4: Experimental verification of stiffness response. (A) Load-displacement data from experiments converted into moment rotation data and shows good match with simulations. (B) Stiffness calculated from the experimental data shows expected trend.

Evaluation of Peak Moment and Energy Dissipation

The effect of varying ridge size (π_3) on the peak moment and energy dissipation were then quantified through a parametric analysis. Peak moment is the highest moment recorded in the moment-rotation curve while energy dissipation is calculated as the area enclosed by the loading-unloading curve. Since it is known that the reference geometry (shell with no ridge) does not show snapping behavior with same sense bending, the energy dissipation recorded for opposite sense bending of the reference geometry was used as a normalization parameter. Because it shows energy

dissipation in opposite sense bending, it consequently also shows a larger peak moment when bent in the opposite sense. Therefore, peak moment during opposite sense bending of the reference geometry was used as a normalization parameter for the ridged geometries. Normalized peak moment and normalized energy dissipation for both same sense and opposite sense bending for varying ridge sizes was then quantified and is shown in figure 6.5A and 6.5B respectively. With opposite sense bending, we see an increase in peak moment with increasing ridge size going up to almost 5 times larger than a shell with no ridge, after which there is a significant reduction in peak moment for large ridge sizes. When bending in the same sense, we see a constant, almost linear increase in peak moment followed by a stabilization at a high peak moment of almost 6 times that of a shell with no ridge. Conventional tape springs (shells with no ridge) show energy dissipation only when bent in the opposite sense (see figure 6.5B inset). However, ridged shells are able to display energy dissipation when bent in both same and opposite sense bending. With opposite sense bending, we see very large energy dissipation (up to 40 times that of a shell with no ridge) for π_3 values between 0.35 and 0.6. For same sense bending, remarkably, we see orders of magnitude increased energy dissipation in a large range from π_3 = 0.2 all the way to $\pi_3 = 0.9$. When π_3 lies between 0.6 and 0.8, we see energy dissipation values that are almost 200 times that of a shell with no ridge. However, given the concurrently high peak moments, it is highly unlikely that ridged tapes in these π_3 ranges will practically showcase this energy dissipation. It is almost certain that these tapes will undergo yielding and plastic strain rather than stay within the elastic limit. Nevertheless, it shows an intriguing design space for high yield materials that may be developed in the future, that can access these configurations. The more interesting range which is practically achievable with manageable stresses lies between 0.15 and 0.4. In this range, peak moments go at the highest point, to double that of the conventional tape spring ligament geometry, but these ridged geometries show very large energy dissipation in the same sense (~50 times higher) and about 4 times larger energy dissipation in the opposite sense. Moreover, this is also the range that showcases variable stiffness, with the ability to both increase or decrease stiffness or even, to maintain stiffness with that of the reference conventional geometry.

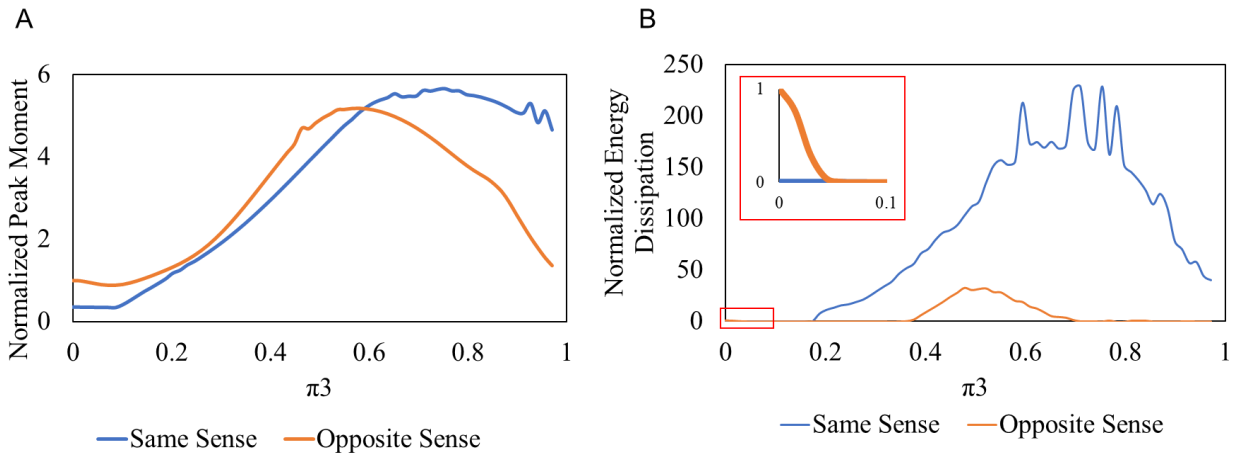

Figure 6.5: (A) Varying ridge size (π_3) vs normalized peak moment for same and opposite sense bending. (B) varying ridge size (π_3) vs normalized energy dissipation for same and opposite sense bending. Inset: Highlights normalized energy dissipation for reference geometries ($\pi_3 = 0$)

6.4 Conclusions

In the previous chapter, we investigated the effect of ridged geometries in the mantis shrimp telson on stiffness control, impact mitigation, and energy dissipation. In this chapter, we extend the concept of ridged geometries by exploring the mechanics of ridges in 3D shell structures. We used dimensionless analysis to determine the control groups governing the deformation behavior for such structures and ran parametric analysis for different geometric parameters with a focus on variation of ridge size and its effect on bending stiffness, peak moments and energy dissipation. Our main findings are:

- Evaluation of moment rotation data revealed that ridged shells show the presence of snap-through instabilities and hysteresis in their loading-unloading cycles leading to the ability to dissipate energy. For specific ridge sizes, same sense loading indicated negative reaction moments indicating the presence of a secondary stable configuration revealing bistability.
- Evaluation of normalized stiffness indicated a change in deformation behavior governed by an interplay between competing mechanisms in the inner ridge and the outer macroshell yielding intriguing elastic instabilities with the ridge size determining the dominant mechanism.

- Normalized stiffness curves also indicated a non-zero ridge size which has the same stiffness as a shell with no ridge indicating the potential for significant variation in other mechanical properties while controlling or maintaining stiffness.
- Normalized peak moment and energy dissipation curves showcased a design space, theoretically capable of extremely large orders of magnitude increased energy dissipation, which may be achievable in the future with high yield materials.
- For a design space situated between $\pi_3 = 0.15$ and $\pi_3 = 0.4$, ridged shell structures are capable of enhanced energy dissipation in both same sense and opposite sense bending, within achievable peak moments while maintaining stiffness.

Overall, these results point to a rich design space for these shells to harness elastic instabilities to produce snapping behavior for enhanced energy dissipation within controlled stiffness bounds. While there is a significant portion of the design space that must still be explored including variations in the other pi groups, as well as experimental realization of the energy dissipation characteristics, these results still provide a good first step for designers in applications such as architected metamaterials for energy dissipation, for morphing structures, in robotic actuation, and for dynamic control such as structural damping, vibrational control and shock absorption applications.

7. SUMMARY AND CONCLUSIONS

Biological organisms have optimized their structures over millions of years of evolution to withstand forces in their natural environment. To compensate for a lack of diversity in their building blocks, they have adapted their structures to withstand mechanical forces. Understanding the mechanisms at play can provide a rich design space for new engineering or synthetic structures that must face similar mechanical loads. The main goals of this study were to first use mechanics as a tool to investigate structural adaptations in biological organisms that allow them to withstand dynamic loads and display remarkable energy dissipation, fatigue resilience and vibrational control characteristics. Then, we endeavored to build a mechanical framework that can define and replicate these characteristics and attempted to extrapolate our findings to bio-inspired structures with the hope that this study provides a good first step towards better, smarter and more efficient solutions for researchers looking to design structures or materials for enhanced energy dissipation, stiffness control, fatigue resilience and acoustic sensitivity.

In our first study, we investigated cancellous bone, with its ability to withstand multiple cycles of loading through a person's lifetime. Using a combination of experimental testing and finite element simulations, we identified key structural parameters, the transverse rods, which acted as sacrificial elements during high cycle fatigue testing, accruing damage and plastic strain and consequently preventing damage of the load carrying members. On increasing the diameter of transverse rods, we found that it led to orders of magnitude increase in fatigue life. We extended the idea to synthetic lattice structures by designing bone-like architecture materials and found that increases in proportion of material oriented transverse to the loading direction led to significant increase in fatigue life. We determined through a stress triaxiality study that this effect is present in both stretching dominated as well as bending dominated structures. We found that the ratio of plastic dissipation study to work done during the cyclic loading process was directly related to the fatigue life of these structures. A statistical analysis of the data revealed empirical modifications to stress vs life curves that would yield better predictions of fatigue life for synthetic lattice structures and architectured materials.

From our fatigue study, we then moved to a study on vibrations. In chapter 3, we investigated the ability of mosquitos to use their antenna for audition in different contexts. We analyzed structural and morphological variations in two sexes of two species of mosquitos that use

audition for different purposes. *Aedes aegypti* mosquitos can follow conspecifics in swarms of thousands of individuals by following their wingbeats, despite a constant noise source; their own wingbeats in close proximity to their antennae. *Uranotaenia lowii* mosquitos can hear and track frog calls with a similar noise source; their wingbeats, in close proximity to their heads. We investigated the effect of structural features in the antennae including their hair and intersegmental variation on the steady state vibrational response to pure tone stimuli and quantified their effect on sensitivity and tuning. We evaluated their ability to track their acoustic targets despite their own noisy wingbeats and found that mosquitos can use a combination of natural frequency modes and their own wingbeats to amplify their acoustic targets. Then we used lumped parameter models and showed that neurophysiologically, mosquitos utilize a non-linear relationship between displacement at the base of the antenna and current generated in their Johnston's organs to harness distortion products produced by the proximity of the peaks in the antennal response of their wingbeats and the acoustic target to amplify the target tone at a lower frequency. Overall, we described mechanical and neurophysiological mechanisms in antennae that allow them to amplify acoustic targets by harnessing the competing signal or the noise source. These results can have significant value in the design of noise-resistant mechanical sensors or acoustic microphones.

In chapter 4, we moved from steady state vibrational analysis to a combination of steady state vibration and stress wave propagation. We investigated the ability of woodpeckers to withstand repeated blows to the head without sustaining brain damage through a mechanical and functional evaluation of their skull bones. We used a combination of micro-CT scanned data and engineering software to design structurally accurate CAD models of the woodpecker head and run finite element simulations. We used a novel technique – the ricker pulse, to better understand the vibrational response in the woodpecker head. We found that the area around the brain vibrates at a different dominant frequency compared to the rest of the woodpecker head, showcasing vibrational isolation. Analysis of stress wave propagation showed that the stress wave bypasses the area of the head near the brain, and instead goes into the neck and body of the woodpecker via the jugal bone. We also validated these results with experiments with 3D printed woodpecker heads.

In chapter 5, we focused on impact resistance and energy dissipation displayed by the telsons of smashing type mantis shrimp during ritualized fighting with conspecifics. We compared the telsons of the smashing type mantis shrimp against a less aggressive shrimp, the spearer. We

identified ridged geometries on the telson of the smasher mantis shrimp that provided a combination of stiffness and compliance; the response dependent on the direction of loading. Dynamic analysis showed us that ridges at the impact location undergo local buckling to prevent global bending of the side wall and arrest the deformation at the next unimpacted ridge. Ridges may act as wave traps retarding the propagation of the stress wave. We found that stress waves moved slower in the ridged geometry vs the smooth geometries and found evidence that ridges convert input longitudinal waves into shear waves. On analysis of ridged geometries with a viscoelastic core, we found that ridged geometries displayed greater viscous damping of the stress wave as well as larger energy dissipation. Overall, these results provided useful design cues for the manipulation of geometry to control stiffness and energy dissipation.

In chapter 6, we extrapolated ridged geometries on the mantis shrimp telson into 3D shell structures. We performed dimensionless analysis of these structures to determine the governing structural parameters. We found that these structures display snap-through instabilities under bending loads in both directions of loading; same sense and opposite sense. We evaluated the effect of ridge size on stiffness and found that ridged geometries show an initial compliance for smaller ridges followed by a stiffening effect for larger ridge sizes. We investigated the deformation behavior and found competing mechanisms between the inner ridge and the outer macroshell that caused elastic instabilities. Our investigation into normalized peak moment and normalized energy dissipation revealed a design space that showed multiple orders of magnitude increases in energy dissipation, but is practically unattainable due to the large peak moments. We also discovered a design space which showcased enhanced energy dissipation (up to 50 times more than a conventional tape spring ligament) with peak moments of 1.5 to 2 times that of the reference configuration, and at the same time the ability to show both more compliant or higher stiffness behavior. Further investigation into this design space can yield very useful structures for applications in architecture materials, shape morphing structures or robotic actuators.

In closing, this study investigated a number of different organisms that display intriguing mechanical properties through manipulation of their structure rather than material composition. Within a common thread of bioinspired structures and dynamic loading, it uncovered structural adaptations in these organisms and built mechanical frameworks in place through the use of computational techniques and novel methodologies. Overall, it provided several design strategies for varied mechanical behavior including enhanced energy dissipation, fatigue resilience, acoustic

sensitivity, impact resistance, and vibrational control. With recent innovations in 3D printing, structures elucidated in this study are not limited to manufacturing challenges and these design strategies can be implemented to produce smarter and more efficient solutions inspired by nature in the design of engineering structures and materials.

REFERENCES

[1] M. A. Meyers, P. Y. Chen, A. Y. M. Lin, and Y. Seki, "Biological materials: Structure and mechanical properties," *Prog. Mater. Sci.*, vol. 53, no. 1, pp. 1–206, 2008.

[2] A. V. Srinivasan, G. K. Haritos, F. L. Hedberg, and W. F. Jones, "Biomimetics: Advancing man-made materials through guidance from nature- an update," *Appl. Mech. Rev.*, vol. 49, no. 10, pp. S194–S200, 1996.

[3] P. Fratzl, "Biomimetic materials research: What can we really learn from nature's structural materials?," *J. R. Soc. Interface*, vol. 4, no. 15, pp. 637–642, 2007.

[4] Y. Sun and Z. Guo, "Recent advances of bioinspired functional materials with specific wettability: from nature and beyond nature," *Nanoscale Horizons*, vol. 4, no. 1, pp. 52–76, 2019.

[5] U. G. K. Wegst, H. Bai, E. Saiz, A. P. Tomsia, and R. O. Ritchie, "Bioinspired structural materials," *Nat. Mater.*, vol. 14, no. 1, pp. 23–36, 2015.

[6] M. Connections, "REVIEW Structural Biological Materials: Critical Mechanics-Materials Connections," no. February, pp. 773–780, 2013.

[7] U. G. K. Wegst and M. F. Ashby, "The mechanical efficiency of natural materials," *Philos. Mag.*, vol. 84, no. 21, pp. 2167–2186, 2004.

[8] P. D. Zavattieri, "Tango with the Piranhas," *Matter*, vol. 2, no. 1, pp. 23–25, 2020.

[9] W. Yang, H. Quan, M. A. Meyers, and R. O. Ritchie, "Arapaima Fish Scale: One of the Toughest Flexible Biological Materials," *Matter*, vol. 1, no. 6, pp. 1557–1566, 2019.

[10] B. Ji and H. Gao, "Mechanical principles of biological nanocomposites," *Annu. Rev. Mater. Res.*, vol. 40, pp. 77–100, 2010.

[11] M. E. Launey, M. J. Buehler, and R. O. Ritchie, *On the mechanistic origins of toughness in bone*, vol. 40. 2010.

[12] A. R. Studart, "Towards high-performance bioinspired composites," *Adv. Mater.*, vol. 24, no. 37, pp. 5024–5044, 2012.

[13] R. Wang and H. S. Gupta, "Deformation and fracture mechanisms of bone and nacre," *Annu. Rev. Mater. Res.*, vol. 41, pp. 41–73, 2011.

[14] J. C. Weaver *et al.*, "The stomatopod dactyl club: A formidable damage-tolerant biological hammer," *Science (80-.).*, vol. 336, no. 6086, pp. 1275–1280, 2012.

[15] B. Nadrowski, T. Effertz, P. R. Senthilan, and M. C. Göpfert, “Antennal hearing in insects - New findings, new questions,” *Hear. Res.*, vol. 273, no. 1–2, pp. 7–13, 2011.

[16] F. Barthelat, “Architectured materials in engineering and biology: Fabrication, structure, mechanics and performance,” *Int. Mater. Rev.*, vol. 60, no. 8, pp. 413–430, 2015.

[17] A. M. Torres, J. B. Matheny, T. M. Keaveny, D. Taylor, C. M. Rimnac, and C. J. Hernandez, “Material heterogeneity in cancellous bone promotes deformation recovery after mechanical failure,” *Proc. Natl. Acad. Sci. U. S. A.*, vol. 113, no. 11, pp. 2892–2897, 2016.

[18] L. Römer and T. Scheibel, “The elaborate structure of spider silk: structure and function of a natural high performance fiber.,” *Prion*, vol. 2, no. 4, pp. 154–161, 2008.

[19] L. J. G. Ib S O N, “T he m echanical properties o f natural m aterials. II. M icrostructures for m echanical efficiency,” vol. 450, pp. 141–162, 1995.

[20] X. Zheng *et al.*, “Ultralight, ultrastiff mechanical metamaterials,” *Science (80-.).*, vol. 344, no. 6190, pp. 1373–1377, 2014.

[21] M. Ashby, “Designing architectured materials,” *Scr. Mater.*, vol. 68, no. 1, pp. 4–7, 2013.

[22] J. B. Berger, H. N. G. Wadley, and R. M. McMeeking, “Mechanical metamaterials at the theoretical limit of isotropic elastic stiffness,” *Nature*, vol. 543, no. 7646, pp. 533–537, 2017.

[23] S. Amin Yavari *et al.*, “Relationship between unit cell type and porosity and the fatigue behavior of selective laser melted meta-biomaterials,” *J. Mech. Behav. Biomed. Mater.*, vol. 43, pp. 91–100, 2015.

[24] S. M. Ahmadi *et al.*, “Fatigue performance of additively manufactured meta-biomaterials: The effects of topology and material type,” *Acta Biomater.*, vol. 65, pp. 292–304, 2018.

[25] S. N. Musy, G. Maquer, J. Panyasantisuk, J. Wandel, and P. K. Zysset, “Not only stiffness, but also yield strength of the trabecular structure determined by non-linear μFE is best predicted by bone volume fraction and fabric tensor,” *J. Mech. Behav. Biomed. Mater.*, vol. 65, no. October 2016, pp. 808–813, 2017.

[26] M. C. Göpfert, H. Briegel, and D. Robert, “Antennal vibrations in mosquitoes,” vol. 2738, pp. 2727–2738, 1999.

[27] D. Avitabile, M. Homer, A. R. Champneys, J. C. Jackson, and D. Robert, “Mathematical modelling of the active hearing process in mosquitoes,” *J. R. Soc. Interface*, vol. 7, no. 42, pp. 105–122, 2009.

[28] B. D. Saltin, Y. Matsumura, A. Reid, J. F. Windmill, S. N. Gorb, and J. C. Jackson, "Material stiffness variation in mosquito antennae," *J. R. Soc. Interface*, vol. 16, no. 154, 2019.

[29] M. P. Su, M. Andrés, N. Boyd-Gibbins, J. Somers, and J. T. Albert, "Sex and species specific hearing mechanisms in mosquito flagellar ears," *Nat. Commun.*, vol. 9, no. 1, 2018.

[30] L. Wang, J. T. M. CheungJason, F. Pu, D. Li, M. Zhang, and Y. Fan, "Why do woodpeckers resist head impact injury: A biomechanical investigation," *PLoS One*, vol. 6, no. 10, pp. 1–8, 2011.

[31] J. ODA, J. SAKAMOTO, and K. SAKANO, "Mechanical Evaluation of the Skeletal Structure and Tissue of the Woodpecker and Its Shock Absorbing System," *JSME Int. J. Ser. A*, vol. 49, no. 3, pp. 390–396, 2006.

[32] Y. Liu, X. Qiu, X. Zhang, and T. X. Yu, "Response of woodpecker's head during pecking process simulated by material point method," *PLoS One*, vol. 10, no. 4, pp. 1–16, 2015.

[33] P. Zhou, X. Q. Kong, C. W. Wu, and Z. Chen, "The Novel Mechanical Property of Tongue of a Woodpecker," *J. Bionic Eng.*, vol. 6, no. 3, pp. 214–218, 2009.

[34] S.-H. Yoon and S. Park, "A mechanical analysis of woodpecker drumming and its application to shock-absorbing systems.," *Bioinspir. Biomim.*, vol. 6, no. 1, p. 016003, 2011.

[35] W. J. Bock, "Kinetics of the avian skull," *J. Morphol.*, vol. 114, no. 1, pp. 1–41, 1964.

[36] N. A. Yaraghi *et al.*, "Impact resistant designs from the cuticle of the mantis shrimp," *ICCM Int. Conf. Compos. Mater.*, vol. 2017-Augus, no. August, pp. 20–25, 2017.

[37] N. Guarín-Zapata, J. Gomez, N. Yaraghi, D. Kisailus, and P. D. Zavattieri, "Shear wave filtering in naturally-occurring Bouligand structures," *Acta Biomater.*, vol. 23, pp. 11–20, 2015.

[38] N. A. Yaraghi *et al.*, "The Stomatopod Telson: Convergent Evolution in the Development of a Biological Shield," *Adv. Funct. Mater.*, vol. 1902238, pp. 1–13, 2019.

[39] P. A. Green and S. N. Patek, "Contests with deadly weapons: Telson sparring in mantis shrimp (Stomatopoda)," *Biol. Lett.*, vol. 11, no. 9, 2015.

[40] J. R. A. Taylor, N. I. Scott, and G. W. Rouse, "Evolution of mantis shrimp telson armour and its role in ritualized fighting," *J. R. Soc. Interface*, vol. 16, no. 157, 2019.

[41] J. R. A. Taylor and S. N. Patek, “Ritualized fighting and biological armor: The impact mechanics of the mantis shrimp’s telson,” *J. Exp. Biol.*, vol. 213, no. 20, pp. 3496–3504, 2010.

[42] A. M. Torres *et al.*, “Bone-inspired microarchitectures achieve enhanced fatigue life,” *Proc. Natl. Acad. Sci.*, vol. 116, no. 49, p. 201905814, 2019.

[43] X. S. Liu, X. H. Zhang, and X. E. Guo, “Contributions of trabecular rods of various orientations in determining the elastic properties of human vertebral trabecular bone,” *Bone*, vol. 45, no. 2, pp. 158–163, 2009.

[44] A. M. Torres *et al.*, “Bone-inspired microarchitectures achieve enhanced fatigue life,” *Proc. Natl. Acad. Sci. U. S. A.*, vol. 116, no. 49, pp. 24457–24462, 2019.

[45] S. M. Haddock, O. C. Yeh, P. V. Mummaneni, W. S. Rosenberg, and T. M. Keaveny, “Similarity in the fatigue behavior of trabecular bone across site and species,” *J. Biomech.*, vol. 37, no. 2, pp. 181–187, 2004.

[46] R. R. Hoy and D. Robert, “Tympanal hearing in insects,” *Annu. Rev. Entomol.*, vol. 41, no. 1, pp. 433–450, 1996.

[47] J. T. Albert and A. S. Kozlov, “Comparative Aspects of Hearing in Vertebrates and Insects with Antennal Ears,” *Curr. Biol.*, vol. 26, no. 20, pp. R1050–R1061, 2016.

[48] R. R. Popper, Arthur N, Simmons, Andrea M, Fay, *S pringer H andbook of A uditory research*. 2003.

[49] C. M. B. Chris- and L. Iii, “Original Communications: Auditory Apparatus of the Culex Mosquito,” *J. Cell Sci.*, vol. s1-3, no. 10, pp. 97–102, 1855.

[50] A. Borkent and P. Belton, “Attraction of female Uranotaenia lowii (Diptera: Culicidae) to frog calls in Costa Rica,” *Can. Entomol.*, vol. 138, no. 1, pp. 91–94, 2006.

[51] G. Menda *et al.*, “The Long and Short of Hearing in the Mosquito Aedes aegypti,” *Curr. Biol.*, vol. 29, no. 4, pp. 709-714.e4, 2019.

[52] D. N. Lapshin and D. D. Vorontsov, “Frequency organization of the Johnston’s organ in male mosquitoes (Diptera, Culicidae),” *J. Exp. Biol.*, vol. 220, no. 21, pp. 3927–3938, 2017.

[53] D. N. Lapshin and D. D. Vorontsov, “Directional and frequency characteristics of auditory neurons in Culex male mosquitoes,” *J. Exp. Biol.*, vol. 222, no. 21, pp. 1–11, 2019.

[54] P. M. V. Simões, R. A. Ingham, G. Gibson, and I. J. Russell, “A role for acoustic distortion in novel rapid frequency modulation behaviour in free-flying male mosquitoes,” *J. Exp. Biol.*, vol. 219, no. 13, pp. 2039–2047, 2016.

[55] M. C. Göpfert and D. Robert, “Active auditory mechanics in mosquitoes,” *Proc. R. Soc. B Biol. Sci.*, vol. 268, no. 1465, pp. 333–339, 2001.

[56] M. C. Göpfert, A. D. L. Humphris, J. T. Albert, D. Robert, and O. Hendrich, “Power gain exhibited by motile mechanosensory neurons in Drosophila ears,” *Proc. Natl. Acad. Sci. U. S. A.*, vol. 102, no. 2, pp. 325–330, 2005.

[57] E. H. Slifer and S. S. Sekhon, “The fine structure of the sense organs on the antennal flagellum of the Yellow Fever Mosquito Aedes aegypti (Linnaeus),” *J. Morphol.*, vol. 111, no. 1, pp. 49–67, 1962.

[58] J. F. V. Vincent and U. G. K. Wegst, “Design and mechanical properties of insect cuticle,” *Arthropod Struct. Dev.*, vol. 33, no. 3, pp. 187–199, 2004.

[59] B. J. Arthur, R. A. Wyttenbach, L. C. Harrington, and R. R. Hoy, “Neural responses to one-And two-tone stimuli in the hearing organ of the dengue y vector mosquito,” *J. Exp. Biol.*, vol. 213, no. 8, pp. 1376–1385, 2010.

[60] E. H. Armstrong, “The super-heterodyne-its origin, develop- ment, and some recent improvements* by edwin h. armstrong,” *October*, pp. 539–552, 1924.

[61] A. Tripathy, M. J. Nine, D. Losic, and F. S. Silva, “Nature inspired emerging sensing technology: Recent progress and perspectives,” *Mater. Sci. Eng. R Reports*, vol. 146, no. July, p. 100647, 2021.

[62] J. Jung *et al.*, “A Natural Stress Deflector on the Head? Mechanical and Functional Evaluation of the Woodpecker Skull Bones,” *Adv. Theory Simulations*, vol. 2, no. 4, p. 1800152, 2019.

[63] D. C. Viano, I. R. Casson, and E. J. Pellman, “Concussion in professional football: Biomechanics of the struck player - Part 14,” *Neurosurgery*, vol. 61, no. 2, pp. 313–327, 2007.

[64] A. C. McKee *et al.*, “Chronic traumatic encephalopathy in athletes: Progressive tauopathy after repetitive head injury,” *J. Neuropathol. Exp. Neurol.*, vol. 68, no. 7, pp. 709–735, 2009.

[65] P. R. A. May, P. Newman, J. M. Fuster, and A. Hirschman, “Woodpeckers and Head Injury,” *Lancet*, vol. 307, no. 7957, pp. 454–455, 1976.

[66] L. J. Gibson, “Woodpecker pecking: How woodpeckers avoid brain injury,” *J. Zool.*, vol. 270, no. 3, pp. 462–465, 2006.

[67] Z. D. Zhu, G. J. Ma, C. W. Wu, and Z. Chen, “Numerical study of the impact response of woodpecker’s head,” *AIP Adv.*, vol. 2, no. 4, pp. 0–8, 2012.

[68] Z. Zhu, W. Zhang, and C. Wu, “Energy conversion in woodpecker on successive peckings and its role on anti-shock protection of brain,” *Sci. China Technol. Sci.*, vol. 57, no. 7, pp. 1269–1275, 2014.

[69] Z. Zhu, C. Wu, and W. Zhang, “Frequency analysis and anti-shock mechanism of woodpecker’s head structure,” *J. Bionic Eng.*, vol. 11, no. 2, pp. 282–287, 2014.

[70] H. Ryan, “Ricker, Ormsby; Klander, Butterworth -A Choice of wavelets,” *CSEG Rec.*, vol. September, pp. 24–25, 1994.

[71] Y. Wang, “The Ricker wavelet and the Lambert W function,” *Geophys. J. Int.*, vol. 200, no. 1, pp. 111–115, 2015.

[72] K. Laksari, M. Kurt, H. Babaee, S. Kleiven, and D. Camarillo, “Mechanistic Insights into Human Brain Impact Dynamics through Modal Analysis,” *Phys. Rev. Lett.*, vol. 120, no. 13, p. 138101, 2018.

[73] S. N. Patek and R. L. Caldwell, “Extreme impact and cavitation forces of a biological hammer: Strike forces of the peacock mantis shrimp Odontodactylus scyllarus,” *J. Exp. Biol.*, vol. 208, no. 19, pp. 3655–3664, 2005.

[74] R. L. Caldwell and H. Dingle, “Ecology and evolution of agonistic behavior in stomatopods,” *Naturwissenschaften*, vol. 62, no. 5, pp. 214–222, 1975.

[75] Y. Li, J. Deng, J. Zhou, and X. Li, “Elastic and viscoelastic mechanical properties of brain tissues on the implanting trajectory of sub-thalamic nucleus stimulation,” *J. Mater. Sci. Mater. Med.*, vol. 27, no. 11, 2016.

[76] N. Lee, Z. Liu, S. Mun, K. Johnson, and M. F. Horstemeyer, “The Function of Horn Ridges for Impact Damping,” *SSRN Electron. J.*, 2019.

[77] M. Pezzulla, N. Stoop, M. P. Steranka, A. J. Bade, and D. P. Holmes, “Curvature-Induced Instabilities of Shells,” *Phys. Rev. Lett.*, vol. 120, no. 4, p. 48002, 2018.

[78] R. Lakes, “Advances in negative poisson’s ratio materials,” *Adv. Mater.*, vol. 5, no. 4, pp. 293–296, 1993.

[79] K. Bertoldi, P. M. Reis, S. Willshaw, and T. Mullin, “Negative poisson’s ratio behavior induced by an elastic instability,” *Adv. Mater.*, vol. 22, no. 3, pp. 361–366, 2010.

[80] D. Restrepo, “Programmable Cellular Materials,” Purdue University, 2015.

[81] K. W. Hector, D. Restrepo, C. T. Bonilla, L. G. Hector, N. Mankame, and P. D. Zavattieri, “Mechanics of chiral honeycomb architectures with phase transformations,” *J. Appl. Mech. Trans. ASME*, vol. 86, no. 11, pp. 1–15, 2019.

[82] F. Runkel, G. Ramstein, G. Molinari, A. F. Arrieta, and P. Ermanni, “Mechanics of curved-ligament hexachiral metastructures under planar deformations,” *J. Mech. Phys. Solids*, vol. 125, pp. 145–163, 2019.

[83] F. Runkel, G. Molinari, A. F. Arrieta, and P. Ermanni, “Tailorable Stiffness Chiral Metastructure,” *Phys. Status Solidi - Rapid Res. Lett.*, vol. 11, no. 10, pp. 1–6, 2017.

[84] J. A. Faber, J. P. Udani, K. S. Riley, A. R. Studart, and A. F. Arrieta, “Dome-Patterned Metamaterial Sheets,” *Adv. Sci.*, vol. 7, no. 22, pp. 1–9, 2020.

[85] B. Assouar, B. Liang, Y. Wu, Y. Li, J. C. Cheng, and Y. Jing, “Acoustic metasurfaces,” *Nat. Rev. Mater.*, vol. 3, no. 12, pp. 460–472, 2018.

[86] D. Yang, L. Jin, R. V Martinez, and K. Bertoldi, “Phase-transforming and switchable metamaterials,” vol. 6, pp. 1–9, 2016.

[87] K. S. Riley, H. Le Ferrand, and A. F. Arrieta, “Modeling of snapping composite shells with magnetically aligned bio-inspired reinforcements,” *Smart Mater. Struct.*, vol. 27, no. 11, 2018.

[88] J. P. Udani and A. F. Arrieta, “Analytical Modeling of Multi-sectioned Bi-stable Composites: Stiffness Variability and Embeddability,” *Compos. Struct.*, vol. 216, no. November 2018, pp. 228–239, 2019.

[89] I. K. Kuder, A. F. Arrieta, and P. Ermanni, “Design space of embeddable variable stiffness bi-stable elements for morphing applications,” *Compos. Struct.*, vol. 122, pp. 445–455, 2015.

[90] D. P. Holmes and A. J. Crosby, “Snapping surfaces,” *Adv. Mater.*, vol. 19, no. 21, pp. 3589–3593, 2007.

[91] A. Pal, V. Restrepo, D. Goswami, and R. V. Martinez, “Exploiting Mechanical Instabilities in Soft Robotics: Control, Sensing, and Actuation,” *Adv. Mater.*, vol. 33, no. 19, 2021.

[92] K. A. Seffen and S. Pellegrino, “Deployment dynamics of tape springs,” *Proc. R. Soc. A Math. Phys. Eng. Sci.*, vol. 455, no. 1983, pp. 1003–1048, 1999.

PUBLICATIONS

Published:

1. A. M. Torres, A. A Trikanad, C. A. Aubin, F. M. Lambers, C. M. Rimnac, P. Zavattieri, C. J. Hernandez, “Bone inspired microarchitectures achieve enhanced fatigue life”. Proceedings of the National Academy of Sciences, 116(49), 201905814, (2019) [42]
2. N. A. Yaraghi, A. A. Trikanad, D. Restrepo, W. Huang, J. Rivera, S. Herrera, M. Zhernenkov, D. Y. Parkinson, R. L. Caldwell, P. D. Zavattieri, D. Kisailus, “ The Stomatopod Telson: Convergent Evolution in the Development of a Biological Shield”, Advanced Functional Materials, vol 1902238, p, 1902238, 2019 [38]
3. J. Y. Jung, A Pissarenko, A. A. Trikanad, D. Restrepo, F. Y. Su, A. Marquez, D. Gonzalez, S. E. Naleway, P. Zavattieri, J. McKittrick, “A Natural Stress Deflector on the Head? Mechanical and Functional Evaluation of the Woodpecker Skull Bones”, Advanced Theory and Simulations, vol 2, no 4, p.1800152 (2019)[62]
4. J. Rivera, S Murata, M. S. Hosseini, A. A. Trikanad, R. James, A. Pickle, N. Yaraghi, N. Matsumoto, W. Yang, D. Y. Parkinson, H. S. Barnard, P. Zavattieri, A. Arakaki, D. Kisailus, “ Structural Design Variations in Beetle Elytra”, Advanced Functional Materials, vol 2106468, p 1-14 (2021)

In preparation:

1. A. A. Trikanad, H. Pantoja, X. Bernal, P. Zavattieri, “Mechanical and neurophysiological mechanisms in mosquito antennae promote the detection of acoustic targets amidst noise”, Status: In preparation.
2. A. A. Trikanad, P. Zavattieri, “Mechanics of ridged shell metastructures for tailorable stiffness and energy dissipation”, Status: In preparation